DOCTOR OF PHILOSOPHY

Spatio-temporal modelling of gene regulatory networks containing negative feedback loops

Sturrock, Marc

Award date:
2013

Awarding institution:
University of Dundee

DOCTOR OF PHILOSOPHY

Spatio-temporal modelling of gene regulatory networks containing negative feedback loops

Marc Sturrock

2013

University of Dundee

Spatio-temporal modelling of gene regulatory networks containing negative feedback loops

by

Marc Sturrock

A Thesis submitted for the degree of Doctor of Philosophy

Division of Mathematics

University of Dundee

Dundee

March 2013

Contents

Acknowledgements **vii**

Declaration **x**

Certification **xi**

1 Introduction **1**

2 Biological background **7**

2.1 Intracellular signal transduction 7

2.1.1 Genes 8

2.1.2 Gene regulatory networks 10

2.1.3 Negative feedback loops 11

2.2 The spatial structure of the eukaryotic cell 12

2.3 Intracellular transport mechanisms 13

2.3.1 Diffusive transport 14

2.3.2 Active transport 15

2.3.3 Transport across the nuclear membrane 16

The Hes1 gene regulatory network **18**

3 The Hes1 gene regulatory network **19**

3.1 Introduction 19

3.2 Biological background 19

3.3 Mathematical modelling of the Hes1 gene regulatory network 21

3.3.1 Literature review 21

3.3.2 Ordinary differential equation model 22

3.3.3 Delay differential equation model 24

4 A reaction-diffusion model of the Hes1 gene regulatory network **26**

4.1 Introduction 26

4.2 Reaction-diffusion model formulation 26

4.3 Numerical simulation results 29

4.4 Parameter values 32

4.5 The influence of spatial dimension 35

4.6 Drug treatment 43

4.6.1 Inhibition of the proteasome 43

4.6.2 Translation inhibition 45

4.7 The influence of extrinsic noise: exploring model dependence on initial conditions 47

4.8 Discussion 48

5 The influence of the nuclear membrane, active transport and cell shape on the Hes1 gene regulatory network 51

5.1 Introduction 51

5.2 Extended model formulation 52

5.3 Numerical simulation results 55

5.4 Modelling spatial effects in the nucleus 61

5.5 Convection as the sole transport mechanism of cytoplasmic Hes1 protein 63

5.6 Microtubule disruption numerical experiment 66

5.7 The influence of cell shape 70

5.8 Drug treatment 75

5.8.1 Inhibition of the proteasome 75

5.8.2 Translation inhibition 77

5.9 The influence of extrinsic noise: exploring model dependence on initial conditions 78

5.10 Discussion 79

6 A spatial stochastic model of the Hes1 gene regulatory network 83

6.1 Introduction 83

6.2 Spatial stochastic model formulation 85

6.2.1 The reaction-diffusion master equation 86

6.2.2 Domain, initial and boundary conditions 88

6.3 Numerical simulation results 89

6.3.1 The model reproduces quantitative and qualitative behaviour of wild-type ES cells 89

6.3.2 Intrinsic noise can explain variability in ES cell differentiation 93

6.4 Parameter sweeps 93

6.4.1 Hes1 must bind to the promoter sufficiently fast for oscillations to be observed 96

6.4.2 Oscillatory dynamics are only found for sufficiently large diffusion coefficients 98

6.4.3 Oscillatory behaviour is robust to changes in the position of the promoter site if the diffusion coefficient is large enough . . 99

6.5 Controlling differentiation responses via drug treatment 101

6.6 The influence of extrinsic noise: exploring model dependence on initial conditions 104

6.7 Discussion 106

The p53-Mdm2 gene regulatory network **108**

7 The p53-Mdm2 gene regulatory network **109**

7.1 Introduction 109

7.2 Biological background 109

7.3 Mathematical modelling of the p53-Mdm2 gene regulatory network . 112

7.3.1 Literature review 112

7.3.2 Ordinary differential equation model 113

7.3.3 Delay differential equation model 116

8 A reaction-diffusion model of the p53-Mdm2 gene regulatory network **117**

8.1 Introduction 117

8.2 Reaction-diffusion model formulation 117

8.3 Numerical simulation results 122

8.4 Parameter values 123

8.5 Proteasome inhibition numerical experiment 126

8.6 Discussion 127

9 The influence of the nuclear membrane and active transport on the p53-Mdm2 gene regulatory network **131**

9.1 Introduction 131

9.2 Extended p53-Mdm2 model formulation 131

9.3 Numerical simulation results 133

9.4 Microtubule disruption numerical experiment 137

9.5 Proteasome inhibition numerical experiment 142

9.6 Discussion 146

10 Discussion and future directions **149**

10.1 Discussion 149

10.2 Future directions 154

10.2.1 Partial differential equation models 154

10.2.2 Spatial stochastic Hes1 gene regulatory network model 155

10.2.3 Spatial stochastic p53-Mdm2 gene regulatory network model . 156

11 Appendix **158**

11.1 Protein translation and synthesis in the cytoplasm: consideration of the location of the endoplasmic reticulum 158

11.2 The Hes1 gene regulatory network 160

11.2.1 Dulac's criterion 160

11.2.2 Non-dimensionalisation of reaction-diffusion models 161

11.2.3 Parameter sweeps of spatial stochastic model 163

11.3 The p53-Mdm2 gene regulatory network 169

11.3.1 Busenberg's criterion 169

11.3.2 Non-dimensionalisation of reaction-diffusion models 171

Acknowledgements

I would first and foremost like to thank Professor Mark Chaplain for giving me the opportunity to work with him. I am very grateful for all his supervision, input into my work and support. I am also grateful for his generosity and good humour. Due to his excellent supervision, my PhD was completed very smoothly and I thoroughly enjoyed the path to completion.

I am grateful to my family for the encouragement and support they have given me during my studies. I would also like to thank Ding for providing a pleasant distraction from all things related to my work and lending her design skills to me whenever I needed them.

I wish also to thank my collaborators Dr Andreas Hellander and Dr Anastasios Matzavinos for the numerous helpful discussions concerning various aspects of spatial stochastic modelling. These discussions were of great importance in the development of my understanding of these issues. I would also like to thank Dr Dimitris Xirodimas and Professor Alastair Thompson for aiding me in elucidating the biological aspects of my studies.

I would like to extend my gratitude and appreciation to all the members of staff of the Division of Mathematics, in particular Mr Nick Dawes for providing me with many software packages and Mrs Shirley Fox for helping me with lots of paper work along

the way. I would also like to thank Dr Fordyce Davidson and Professor Ping Lin for numerous helpful discussions with regards to dynamical systems theory and numerical methods.

I would also like to pay special thanks to my fellow PhD students and the postdoctoral researchers here in Dundee (past and present). In particular, I would like to mention the names of Niall Deakin, Daniela Schlüter, Ebraheem Alzahrani, Mohannad Al-Tameemi, Yangfan Wang and Faik Mayah. It was delightful to have your company during my studies.

Last, but not least, I would like gratefully acknowledge the support of the ERC Advanced Investigator Grant 227619, “M5CGS - From Mutations to Metastases: Multiscale Mathematical Modelling of Cancer Growth and Spread”, which made this work possible.

Declaration

I declare that the following thesis is my own composition and that it has not been submitted before in application for a higher degree.

Marc Sturrock

Certification

This is to certify that Marc Sturrock has complied with all the requirements for the submission of this Doctor of Philosophy thesis to the University of Dundee.

Professor Mark A. J. Chaplain

Chapter 1

Introduction

As the abundance of molecular data in the life sciences increases, the use of mathematical and computational tools to provide a deeper understanding of how gene regulatory networks (GRNs) function is becoming both necessary and possible. In the last 10 years or so, the field known as 'systems biology' has emerged which seeks to understand complex systems comprised of many connected elements with correlated behaviours and non-linear interactions. Systems biology is an inherently multidisciplinary field, combining expertise and techniques from subjects such as mathematical biology, bioinformatics, image processing, biophysics, wet-lab biology and computer science. A large component of systems biology is concerned with the formulation, study and analysis of theoretical models.

There are many good reasons to develop and use models. One of their main uses in research is to predict how the system of interest will behave under conditions not yet tested experimentally. There are many examples in the literature of computational modelling successfully guiding biological experiments, for example see Locke et al. (2005). Models may also be designed for communication of concepts, for sharing with collaborators, for re-use as components of larger models, and even for training

purposes (e.g. flight simulators, virtual surgery). We can also use models to try to unearth the causes of an event that has already happened, for example, the Northeast America blackouts in 2003 (Bolouri, 2008).

The sheer size and complexity of the data from global, high-throughput technologies is such that unbiased and comprehensive data analysis can only be performed via computational methods. Moreover, GRNs, and indeed most biochemical networks, are highly nonlinear systems, so that it is often very difficult to predict their behaviours without extensive modelling. Computational mathematical models permit the use of sophisticated analyses and visualisation methods that can reveal deeply hidden properties of complex systems. Another very attractive feature of mathematical and computational modelling is that the models can be unambiguously described and communicated. The language of mathematics is universally understood, so dissemination of mathematical models can be trivial. Furthermore, computational models that conform to certain standards can be automatically interpreted by a variety of software tools (e.g. SMBL models), allowing greater scrutiny and re-use while avoiding mishandling.

Perhaps the strongest argument for using computational techniques to model and analyse GRNs is that the low cost and high performance of computers allows us to perform large numbers of *in-silico* experiments. *In-silico* experiments (i.e., theoretical experiments facilitated by the power of computers) can explore scenarios too costly (in terms of time or money) or too complicated to explore in a laboratory. They can help us develop insights into the roles of different regulatory interactions within a system, and guide experimental planning. *In-silico* experiments can also highlight inconsistencies in our assumptions, such as when a GRN model is shown to be incapable of reproducing certain experimental observations (this is something that we will encounter in this thesis, see section 8.5).

In addition to the above attractions, computational models of GRNs provide a number

of serendipitous benefits. For example, in order to construct a computational model, one often has to make all assumptions explicit. If there are any provisos, gaps, or arbitrarily defined values or interactions, their formal definition within a computational model should bring them to light. Of course, such explicit declarations can still be buried in pages of code or equations, but good practice guidelines can help users identify such issues. Making assumptions explicit can also trigger new lines of investigation. The models also facilitate automated consistency checking. Another benefit of computational modelling is that such models can be stored in databases and programmatically interrogated, thus allowing researchers everywhere to quickly locate and download a model. Indeed, the concept of 'cloud biology' is gaining momentum and many authors recognise its importance for the future (Slaymaker et al., 2012). As these technologies mature, one can envisage organ-, organism- or disease-specific model repositories that allow users to share interim models and explore the behaviour of their model in the context of models of related processes developed by other researchers.

Computational models of GRNs can take a variety of forms. Until recently, modelling studies have predominately used deterministic, temporal approaches. This includes models comprised of directed and undirected graphs, boolean networks, generalised logical networks, nonlinear ordinary differential equations, delay differential equations, stochastic differential equations and stochastic master equations (Jong, 2002). Although these models have attempted to be quantitative, they have often only yielded qualitative insights into the underlying biological system. This situation can be explained by two major difficulties facing the field of systems biology. First of all, the biochemical reaction mechanisms underlying regulatory interactions are usually not known or are incompletely known. This means that detailed kinetic models cannot be built and more approximate models are required. In the second place, quantitative information regarding kinetic parameters and molecular concentrations is only seldom

available. Unsurprisingly, the best modelling efforts have used fine-grained, quantitative and stochastic models which have been restricted to regulatory networks of small size and modest complexity that have been already well-characterised through experimental means. There has also been a marked lack of *spatio-temporal models* of GRNs in the systems biology literature — such models form the focus of this thesis.

In comparison to temporal models there are few spatio-temporal models of intracellular signalling pathways in the literature, although the body of work is growing. Early attempts at spatio-temporal modelling of intracellular pathways containing negative feedback loops were carried out by Glass and co-workers, who recognised the inherent spatial heterogeneity of cells and observed oscillatory dynamics for activator-inhibitor kinetics (Glass and Kauffman, 1970; Shymko and Glass, 1974). Mahaffy et al. subsequently developed models to capture spatial features for such pathways, introducing delays for transcription and translation and oscillatory dynamics were again observed (Mahaffy and Pao, 1984; Busenberg and Mahaffy, 1985; Mahaffy, 1988). More recently, Gordon et al. developed a partial differential equation (PDE) model for the p53-Mdm2 pathway (Gordon et al., 2009) including delays and which produced sustained oscillations. The model was solved in two spatial dimensions, but did not consider separate compartments for the nucleus and cytoplasm. Other PDE models not containing delays have also appeared recently including those of Terry et al. who studied the Notch and NF-κB pathways, finding oscillatory behaviour that closely resembles experimental results (Terry et al., 2011; Terry and Chaplain, 2011). Spatio-temporal models of intracellular processes have been investigated not only in the context of negative feedback loops. For instance, Kholodenko and co-workers have considered general reaction-diffusion models of protein kinase and phosphatase activity within cells (Brown and Kholodenko, 1999; Kholodenko, 2006), Cangiani and Natalini have examined active transport of proteins along microtubules (Cangiani and Natalini, 2010), and Dinh et al. have studied intracellular trafficking of adenoviral

vectors (Dinh et al., 2005). For a review of modelling intracellular spatio-temporal interactions, see Rangamani and Iyengar (2007) and Kholodenko (2006). It is clear from these early studies that the development of models which reflect spatial and temporal aspects of intracellular pathways can be regarded as a first step towards an effective computational approach in investigating conditions under which pathways become deregulated and in the optimising of targeted drug treatment.

The strength of models depends on the appropriateness of the modelling assumptions. Hence, in the next chapter we present background biology for eukaryotic cells, specifically focusing on gene regulatory networks, the spatial structure of the eukaryotic cell and intracellular transport mechanisms. In this thesis, we will focus on two specific gene regulatory networks, the Hes1 GRN (which plays a role in developmental processes) and the p53-Mdm2 GRN (which is critical for regulating the cell-cycle). Both can become deregulated in human cancer (Sang et al., 2008; Lane, 1992), so their study is interesting both from a biological and a clinical perspective. We present background biology for the Hes1 GRN in chapter 3 as well as a literature review of previous mathematical modelling efforts. Importantly, we demonstrate that neglecting spatial information can have major consequences in terms of reproducing experimental data. In chapter 4 we formulate and explore numerically a reaction-diffusion model of the Hes1 GRN which builds on and extends previous modelling efforts. Using our PDE model we are able to reproduce the oscillatory dynamic observed in experimental data, as well as mimicking well-documented biological experiments. We explore further the importance of spatial considerations in chapter 5 by making model extensions which are only possible under a spatial regime. Specifically, we study the influence of the nuclear membrane, active transport and cell shape on the Hes1 GRN. We find our extended model is more robust to changes in parameters as well as being robust to geometrical changes in our computational domain. We suggest a possible biological experiment that could distinguish which model (the one presented in chapter 4 or the

one presented in chapter 5) is more accurate. We depart from the continuum PDE approach in chapter 6 and develop a spatial stochastic model which accounts for intrinsic noise in the Hes1 GRN. We focus our modelling efforts on embryonic stem cells (due to the abundance of expression data for this cell line) and make a prediction regarding the source of heterogeneity in embryonic stem cell differentiation. In chapter 7 we introduce the more complex p53-Mdm2 GRN. As we did for the Hes1 GRN in chapter 3, we begin by introducing the background biology of the p53-Mdm2 GRN and a literature review of previous mathematical modelling efforts. Again, we are able to demonstrate that the use of strictly temporal approaches can have certain limitations. In chapter 8, a reaction-diffusion model of the p53-Mdm2 GRN is formulated and a numerical simulation study is presented. Interestingly, a proteasome inhibition numerical experiment unearths an inconsistency between our simulations and a biological experiment, implying something is a askew with our modelling assumptions. This problem is rectified in chapter 9, where we consider the influence of active transport and the nuclear membrane on the p53-Mdm2 GRN. By accounting for active transport we are able to faithfully reproduce data produced by the proteasome inhibition biological experiment. Finally, concluding remarks and directions for future research are given in chapter 10. Some technical details are deferred to an Appendix.

Chapter 2

Biological background

In this chapter we review the biology of intracellular signal transduction. We focus on gene regulatory networks, negative feedback loops and the spatial structure of eukaryotic cells. We also discuss how molecules are transported within the cell.

2.1 Intracellular signal transduction

Intracellular signal transduction can be described as the transmission of molecular signals from a cell's exterior to its interior. Molecular signals are transmitted between cells by the secretion of hormones and other chemical factors. The ability of an organism to function normally is dependent on all the cells of its different organs communicating effectively with their surrounding environment and with each other — a phenomenon known as *intercellular* communication. Eukaryotic cells require stimulation for cell division and survival, for example, it is known that in the absence of certain growth factors, the cell will undergo apoptosis (Collins et al., 1994). These extracellular stimulation requirements are necessary for controlling cell behaviour in unicellular and multicellular organisms. In fact, signal transduction pathways are perceived to be

so central to biological processes that a large number of diseases are attributed to their disregulation.

Once a cell picks up a hormonal or sensory signal, it must transmit this information from the surface to the interior parts of the cell — for example, to the nucleus. This occurs via signal transduction pathways that are very specific, both in their activation and in their downstream actions. Thus, the various organs in the body respond in an appropriate manner (only) to relevant signals. In eukaryotic cells, most intracellular proteins are activated by a ligand/receptor interaction and possess an enzymatic activity — examples include tyrosine kinases and phosphatases. Some of them create second messengers such as cyclic AMP and IP3, the latter controlling the release of intracellular calcium stores into the cytoplasm. In general, second messengers are molecules that relay signals from receptors on the cell surface to target molecules inside the cell, in the cytoplasm or nucleus. These second messengers then bring into play complex GRNs which control the levels of mRNA and protein copy numbers through various feedback loops. The changes in protein and mRNA copy numbers can result in changes in cell behaviour, structure and the environment. For example, a yeast cell which is surrounded by sugar solution will switch on genes to make enzymes that process the sugar and convert it to alcohol. This process, which we associate with wine-making, is how the yeast cell survives, gaining energy to multiply, which under normal circumstances would enhance its survival prospects. An overview of signal transduction is given in the schematic diagram in Figure 2.1.

2.1.1 Genes

The traditional definition of a gene is a region of DNA that is transcribed as a single unit and carries information for a discrete hereditary characteristic, usually corresponding to a single protein or a single RNA (Alberts et al., 2008). This definition has been

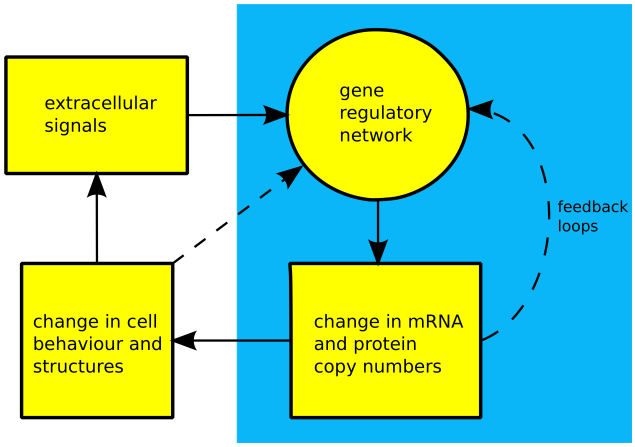

Figure 2.1: *A schematic diagram presenting an overview of the main components of intracellular signal transduction. Signals from outside the cell are processed by gene regulatory networks which cause changes in mRNA and protein levels. These changes can influence cell behaviour and internal structure or initiate certain feedback loops. The components of signal transduction which are studied in this thesis are highlighted by the blue rectangle.*

challenged in recent years, and it appears that what constitutes a gene often depends on its context, hence there no longer exists a universally accepted definition (Keller and Harel, 2007). It has been discovered that a gene may encode multiple transcription start sites, overlapping coding regions, alternative splicing sites, untranslated and regulatory RNAs, and enhancer binding sites hundreds of kilo-bases away from the basal promoter they act on. This new data has led to an updated definition of a gene as "*a union of genomic sequences encoding a coherent set of potentially overlapping functional products*" (Gerstein et al., 2007). This updated definition defines genes by functional products, whether they are proteins or RNA, rather than specific DNA loci.

In this thesis, we are concerned with the functional products of genes and how they regulate the expression of other genes. Our focus is on the theoretical and computational techniques that we can use to gain the deepest insights from the available expression data. We are aided in this undertaking by the fact that models of GRNs ultimately make predictions about features digitally encoded in DNA, which can be tested unambiguously using DNA-based technologies.

2.1.2 Gene regulatory networks

A gene regulatory network or genetic regulatory network lies at the core of intracellular signal transduction. In brief, a GRN is a collection of DNA segments in a cell which interact with each other indirectly through their RNA and protein products (and with other substances in the cell), thereby governing the rates at which genes in the network are transcribed into mRNA. In Figure 2.2, a schematic diagram of a generic gene regulatory network is presented.

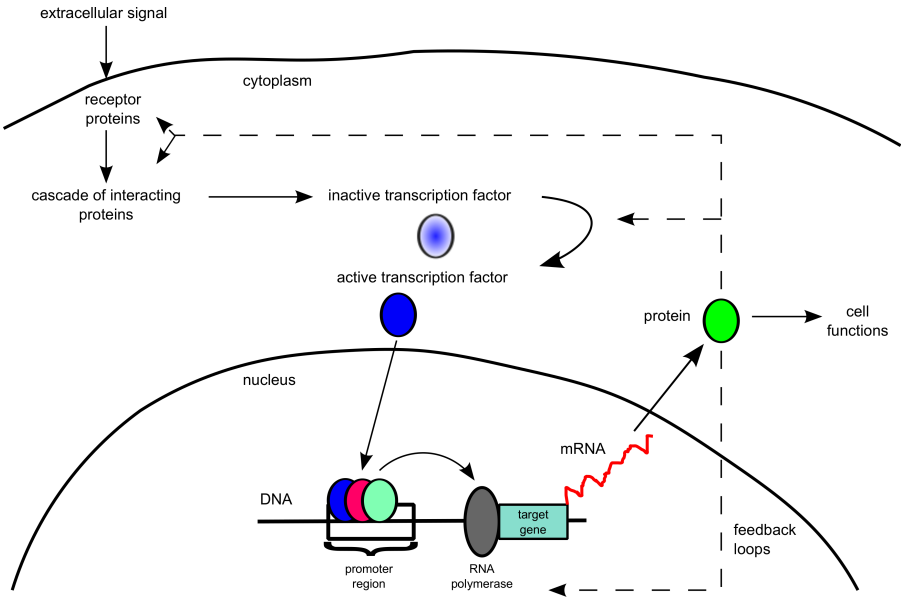

Figure 2.2: *A schematic diagram presenting a generic GRN. This diagram illustrates the chain of intracellular events that occur when a cell receives an extracellular signal.*

The sequence of events illustrated in Figure 2.2 can be summarised as follows. The cell receives an extracellular signal via specific receptor proteins at the cell membrane. This signal is carried through the cytoplasm by a cascade of interacting proteins which often results in the activation of transcription factors. Transcription factors are a class of molecules involved in regulating gene expression. They are usually proteins, although they can also consist of short, non-coding RNA. Transcription factors function by recognising certain nucleotide sequences before or after the gene in the nucleus.

Eukaryotes often have a promoter region upstream from the gene, with certain specific motifs that are recognised by the various types of transcription factor. By binding to this region at the start of other genes (or even their own gene), transcription factors can switch the gene 'on' or 'off', or in other words, initiate or inhibit the binding of RNA polymerase. Transcription factors are also usually found working in groups or complexes, forming multiple configurations that allow for varying degrees of control over rates of transcription. Once RNA polymerase is bound, the process of transcription can begin which yields mRNA. The newly formed mRNA is transported across the nuclear membrane and can then diffuse in the cytoplasm. In the cytoplasm, the process of translation can take place, where mRNA molecules interact with ribosomes (the protein production factories of the cell) to produce protein. It is worth noting that a single mRNA molecule can produce large quantities of protein. The protein molecules can be involved in numerous different events, such as feedback loops (positive or negative) or protein cascades which can result in changes in cellular function.

2.1.3 Negative feedback loops

Negative feedback loops controlling the concentrations of key intracellular proteins are prevalent in a diverse range of important cellular processes. Examples include inflammation, meiosis, apoptosis and the heat shock response (Alberts et al., 2008; Lahav et al., 2004; Fall et al., 2002). Experimental data reveal that pathways containing negative feedback loops can exhibit sustained oscillations (Hirata et al., 2002; Geva-Zatorsky et al., 2006; Nelson et al., 2004; Shankaran et al., 2009). This is not unexpected given the interactions involved in a negative feedback loop.

A generic example of a negative feedback loop with variables x and y is shown in Figure 2.3. The interactions involved in this negative feedback loop can be described as follows. An increase in x causes y to increase, which in turn results in the inhibition

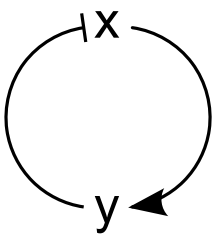

Figure 2.3: *A schematic diagram of a generic negative feedback loop.*

of x. After x begins to decrease, this will also cause y levels to diminish, eventually allowing x to increase again. This process repeats and thus produces oscillations in both x and y.

2.2 The spatial structure of the eukaryotic cell

Gene regulation is an inherently spatial process. In the eukaryotic cell, there are a variety of internal compartments (see Figure 2.4) called organelles, each of which has its own lipid membrane. Organelle function can be divided into three main categories: information processing, energy processing, and packaging of chemical products. The nucleus (the defining feature of the eukaryotic cell) is the organelle most associated with information processing. It is surrounded by two membranes which are referred to as the nuclear envelope. Nuclear pore complexes determine where species move in and out of the nucleus and how quickly they do so. The nucleus contains long, single strands of DNA called chromosomes, which become visible during cell division. The key process of transcription occurs at specific sites — genes — in the nucleus, and some genes are located closer to the nuclear membrane than others, increasing their sensitivity to transcription factors (Cole and Scarcelli, 2006). Up to 25% of the volume of the nucleus can be taken by structures called nucleoli. Nucleoli are a non-membrane bound structure where ribosomal RNA is transcribed and ribosomal subunits are assembled. Mitochondria (which break down sugars) are associated with

energy processing and have their own internal structures and DNA. The set of packaging organelles is collectively known as the endomembrane system. Its most prominent organelle is the endoplasmic reticulum. This system as a whole is a collection of biological containers that can move, separate, package, and transport chemicals, similar to a chemical manufacturing plant. Cell shape and size change over time and are known to influence intracellular signal transduction (Meyers et al., 2006; Neves et al., 2008). The cytoplasm is the gel-like substance that resides between the cell membrane and nuclear membrane, holding all the cell's internal organelles. The cytoplasm is given structure and shape by the cytoskeleton. The cytoskeleton is comprised of three major types of protein filaments: actin filaments, microtubules and intermediate filaments. The centrosome, located a small distance outside the nuclear envelope, is the primary microtubule-organising centre of eukaryotic cells (where microtubules originate). In many organisms, the centrosome consists of a pair of centrioles, each one a hollow tube formed by nine triplets of microtubules. Lysosomes and peroxisomes are small membrane-bound organelles that contain digestive enzymes used to break down waste materials and make use of molecular oxygen to oxidise organic molecules respectively. Also within the cytoplasm, another key process — translation — occurs in the ribosomes. All of these observations regarding the spatial structure of the eukaryotic cell serve to emphasise the fact the intracellular environment is extremely heterogeneous and mathematical models of GRNs will be more faithful the more they seek to account for spatial features inherent to the eukaryotic cell.

2.3 Intracellular transport mechanisms

To help establish and maintain uneven distributions of specific proteins, RNAs and organelles, eukaryotic cells employ several distinct mechanisms for molecular transport. The appropriate subcellular localisation of molecular species is critical for a cell to

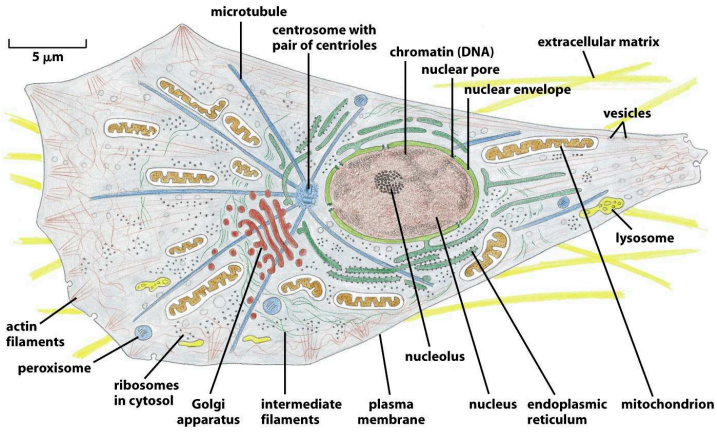

Figure 1-30 *Molecular Biology of the Cell*, Fifth Edition (© Garland Science 2008)

Figure 2.4: *The spatial structure of the eukaryotic cell. Copyright 2008 from Molecular Biology of the Cell, Fifth Edition by Alberts et al. Reproduced by permission of Garland Science/Taylor & Francis LLC.*

remain healthy (Kim et al., 2000; Johansson et al., 2008; Norvell et al., 2005).

2.3.1 Diffusive transport

Diffusion is the main mechanism of transport for many important materials in the cell (e.g. amino acids). It is sometimes described as 'passive transport' as it does not require any energy. Simply put, it is the movement of molecules from a region of high concentration to a region of low concentration. Diffusive transport has a number of important implications for cellular processes because of its undirected nature. Molecules which undergo diffusion can create a stable gradient between the site of synthesis and utilisation. Such gradients can have important implications for certain biological processes, for example, the localisation of bcd mRNA to the anterior of the oocyte is essential for setting up an antero-posterior axis when it is translated in the embryo.

This mRNA encodes a transcription factor that regulates the expression of a hierarchy of segmentation genes that define the details of antero-posterior patterning (Wang and Hazelrigg, 1994). Bcd proteins diffuse away from their anterior source, thus giving rise to a gradient of nuclear protein with a high concentration near the anterior and low concentration at the posterior (Tekotte and Davis, 2002).

2.3.2 Active transport

Unlike molecular diffusion, active transport is directed and requires energy. Active transport is a broad term and can refer to two different transport processes: molecular transport across a membrane or molecular transport facilitated by motor proteins along microtubules.

Active transport across a membrane is directional and requires an input of energy to move substances against their concentration gradients. This allows a cell to maintain small molecules and ions at concentrations very different from those in the surrounding environment. There are two basic types of active transport across a membrane: primary active transport and secondary active transport. Primary active transport involves the direct hydrolysis of ATP, which provides the energy required for transport. Secondary active transport does not use ATP directly. Instead, its energy is supplied by an ion concentration and electrical gradient established by primary active transport. This transport system uses the energy of ATP indirectly to set up the gradient. Calcium pumps are one mechanism cells use to shuttle calcium across cell membranes. Calcium ATPases in the plasma membrane mediate active transport of calcium out of cells, serving to maintain the normal, low levels of free cytoplasmic calcium. Another well studied example of a calcium ATPase is found in the sarcoplasmic reticulum of muscle cells, where it serves to pump calcium from the cytoplasm into those specialised forms of endoplasmic reticulum after a period of muscle contraction.

In section 2.2, we noted that microtubules could provide structure for the eukaryotic cytoplasm. This is not their only function, as they are also involved in the trafficking of intracellular molecules towards the nuclear membrane and cell membrane. Two families of motor proteins associate with the microtubules: dynein and kinesin. Dynein motors attach to proteins and transport them along microtubules towards the cell nucleus whereas kinesin motors attach to proteins and transport them along microtubules towards the cell membrane. Active transport along microtubules is involved in the regulation of gene expression as it facilitates the (fast) translocation of transcription factors into the nucleus, where they modulate gene activity (Lomakin and Nadezhdina, 2010). Also, active transport along microtubules aids in mRNA export within the cell and helps localise mRNAs in particular zones of the cytoplasm — a good example being bcd mRNA which we mentioned in section 2.3.1 (Schnee et al., 2005). We will discuss active transport along microtubules in more detail in section 5.2.

2.3.3 Transport across the nuclear membrane

Transport across the nuclear membrane makes use of both passive and active transport. The nuclear envelope consists of an inner and an outer nuclear membrane. The outer membrane is continuous with the endoplasmic reticulum membrane, and the space between it and the inner membrane is continuous with the endoplasmic reticulum lumen. RNA molecules, which are made in the nucleus, and ribosomal subunits, which are assembled in the nucleolus, are exported to the cytoplasm. In contrast, all the proteins that function in the nucleus are synthesised in the cytoplasm and are then imported. The extensive traffic of materials between the nucleus and cytoplasm occurs through nuclear pore complexes (NPCs), which provide a direct passageway across the nuclear envelope. The NPC is freely permeable to small molecules, metabolites and ions, but acts as a highly efficient molecular sieve for macromolecules — this being its main

function. Proteins containing nuclear localisation signals are actively transported inward through NPCs, while RNA molecules and newly made ribosomal subunits contain nuclear export signals, which direct their outward active transport through NPCs. Some proteins, including the nuclear import and export receptors, continually shuttle between the cytoplasm and nucleus. Ran-GTPase provides both the free energy and the directionality for nuclear transport. Cells regulate the transport of nuclear proteins and RNA molecules through the NPCs by controlling the access of these molecules to the transport machinery. Nuclear localisation signals are not removed, hence, nuclear proteins can be imported repeatedly, as is required each time that the nucleus reassembles after mitosis. We will return to the subject of transport across the nuclear membrane in more detail in section 5.2.

The Hes1 gene regulatory network

Chapter 3

The Hes1 gene regulatory network

3.1 Introduction

In this chapter, we review the biology and previous efforts to mathematically model the Hes1 gene regulatory network. We pay special attention to experiments performed recently and mathematical modelling efforts that the work presented in this thesis builds on.

3.2 Biological background

Hes1 is a member of the family of basic helix-loop-helix (bHLH) transcription factors. Hes1 is known to play a role in somitogenesis, the developmental process responsible for segmentation of the vertebrate embryo. During somitogenesis, a "segmentation clock" controls the timing of the assignment of mesodermal cells to discrete blocks. The segmentation clock depends on the oscillatory expression of a complex network of signalling pathways, including the Hes1 pathway which contains a simple negative

feedback loop (see Figure. 3.1 for a schematic view of this). This feedback loop is formed through interactions of the Hes1 protein with its own gene, where the Hes1 protein binds to N-box sequences on the hes1 promoter and represses the transcription of hes1 mRNA. Specifically, Hes1 (in dimer form) binds to four binding sites upstream of its transcriptional initiation site. Three of these binding sites are N-box sequences and there is also a weak binding region around position –10 (Zeiser et al., 2007).

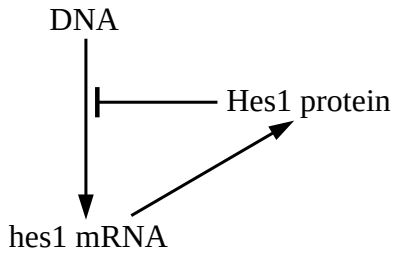

Figure 3.1: *A schematic diagram of the negative feedback loop in the Hes1 GRN. From hes1 mRNA, Hes1 protein is produced via the process of translation. Hes1 protein then inhibits transcription of hes1 mRNA.*

Experiments have measured the levels of hes1 mRNA and Hes1 protein in many different cultured mouse cell lines (Hirata et al., 2002; Masamizu et al., 2006). In response to a single serum treatment, it was found that levels of hes1 mRNA and Hes1 protein exhibited oscillations with a regular period of approximately 2 to 3 hours. This coincides with the period observed for the mouse segmentation clock. Shimojo et al. (2008) showed that Hes1 oscillations are also observed in neural progenitor cells, again with a period of about 2 to 3 hours. It was found that these oscillations were responsible for the maintenance of neural progenitors and that sustained overexpression of Hes1 inhibits proliferation and differentiation of these cells. More recently, Kobayashi et al. (2009) monitored Hes1 expression in embryonic stem (ES) cells. It was found that Hes1 levels still oscillated in space and time, but with a period of 3 to 5 hours, longer than that of other cell lines. This lengthened period is thought to be a result of the increased stability of hes1 mRNA in ES cells (Kobayashi et al., 2009). Kobayashi and

Kageyama continued to dissect the dynamics of the Hes1 GRN, finding that Hes1 oscillations contributed to heterogeneous differentiation responses of the ES cells, with cells expressing low and high levels of Hes1 differentiating into neural and mesodermal cells respectively (Kobayashi and Kageyama, 2010, 2011).

3.3 Mathematical modelling of the Hes1 gene regulatory network

3.3.1 Literature review

Mathematical models of oscillatory dynamics in the Hes1 GRN have taken a variety of forms. The first attempt to model this pathway was presented in the experimental paper Hirata et al. (2002), where an ordinary differential equation (ODE) model was used. However, in order to reproduce the observed oscillations, a third unknown species was introduced. At about the same time, it was discovered that introducing delays to ODE models of gene regulatory networks could produce sustained oscillatory dynamics (Tiana et al., 2002). Jensen et al. found the invocation of an unknown species could be avoided via the introduction of delay terms to a model of the Hes1 GRN (representing the processes of transcription and translation) (Jensen et al., 2003). A delay differential equation (DDE) model of the Hes1 GRN was also studied in Monk (2003). The effect of low particle numbers in Monk's DDE model of the Hes1 GRN was explored in Barrio et al. (2006). Here, the stochastic simulation algorithm (SSA) was extended to allow for delays. Zeiser et al. found that there is not much evidence for synergistic binding in the regulatory region of Hes1, and gave an estimate for the Hill coefficient (Zeiser et al., 2007). The details of the Hes1 pathway were scrutinised

in greater depth in Momiji and Monk (2008), again using a delay differential equation system. In particular, an investigation into the effects of dimerisation and compartmentalisation was presented. The role of Gro/TLE1 was considered in Bernard et al. (2006). Other models have examined the role of the Hes1 GRN in somitogenesis (Agrawal et al., 2009). A spatio-temporal model of the Hes1 GRN (using a PDE approach) was presented in Sturrock et al. (2011), the content of which forms the next chapter. Extensions of this model were considered in Sturrock et al. (2012) and we present these in chapter 5. A spatial stochastic model of the Hes1 GRN in embryonic stem cells was studied in Sturrock et al. (2013) and the material of this paper is presented in chapter 6.

3.3.2 Ordinary differential equation model

Denoting by $[m]$ and $[p]$ the concentrations of hes1 mRNA and Hes1 protein respectively, the basic reaction kinetics for this system can be modelled using ordinary differential equations (ODEs) as follows:

$$\frac{d[m]}{dt} = \frac{\alpha_m^h}{1+([p]/\hat{p})^h} - \mu_m[m], \tag{3.1}$$

$$\frac{d[p]}{dt} = \alpha_p[m] - \mu_p[p]. \tag{3.2}$$

The first term on the right hand side of equation (3.1) is a Hill function, which decreases as the protein concentration increases, modelling repression of hes1 mRNA transcription by Hes1 protein. The parameter α_m is the basal rate of transcription in the absence of Hes1 protein. $\hat{p}$ is the concentration of Hes1 that reduces the rate of initiation of hes1 transcription to half of its basal value (the repression threshold). The

second term represents the natural degradation of hes1 mRNA, at a rate μ_m. The first term on the right hand side of equation (3.2) is the Hes1 protein production term from translation of hes1 mRNA at a rate α_p and the second term represents Hes1 protein degradation at a rate μ_p.

Given that α_m, p_0, h, μ_m, α_p, and μ_p are (strictly) positive constants, Dulac's criterion (stated in Appendix 11.2.1) can be used to prove that periodic solutions for this system do not exist.

Proof. Let $\mathbf{x} = \begin{pmatrix} [\mathrm{m}] \\ [\mathrm{p}] \end{pmatrix}$ and $\mathbf{f}(\mathbf{x}) = \begin{pmatrix} \frac{\alpha_m}{1+([p]/\hat{p})^h} - \mu_m[m] \\ \alpha_p[m] - \mu_p[p] \end{pmatrix} = \begin{pmatrix} \mathrm{M} \\ \mathrm{P} \end{pmatrix}$. Hence we can write equations (3.1), (3.2) more concisely as

$$\frac{d\mathbf{x}}{dt} = \mathbf{f}(\mathbf{x}).$$

Let us suppose a nontrivial closed orbit, ∂A, exists with outward normal, $\mathbf{n}$, and let ∂A bound some nontrivial planar region A. It follows from the divergence theorem in the plane that

$$\oint_{\partial A} \mathbf{f}(\mathbf{x}) \cdot \mathbf{n}\, dr = \iint_A \nabla \cdot \mathbf{f}(\mathbf{x})\, dA. \tag{3.3}$$

From the left hand side we have:

$$\begin{aligned} \oint_{\partial A} \mathbf{f}(\mathbf{x}) \cdot \mathbf{n}\, dr &= \oint_{\partial A} (M d[p] - P d[m]) \\ &= \int_0^T (M\frac{d[p]}{dt} - P\frac{d[m]}{dt})\, dt \\ &= \int_0^T (MP - PM)\, dt = 0. \end{aligned} \tag{3.4}$$

However, from the right hand side we have

$$\begin{aligned}\iint_A \nabla \cdot \mathbf{f}(\mathbf{x})\, dA &= \iint_A \frac{\partial}{\partial [m]} \left(\frac{\alpha_m}{1+([p]/\hat{p})^h} - \mu_m [m] \right) + \frac{\partial}{\partial [p]} \left(\alpha_p [m] - \mu_p [p] \right) dA \\ &= -(\mu_m + \mu_p) \iint_A dA < 0,\end{aligned}$$

which produces a contradiction by the divergence theorem. □

Hence, although the model seems to account for the important features of the negative feedback loop (mRNA production decreases as protein increases), it is unable to reproduce the observed oscillatory dynamics. This implies that the model should be reformulated and the modelling assumptions reconsidered.

3.3.3 Delay differential equation model

In an attempt to model the intracellular processes more accurately, Monk (2003) introduced delays to equations (3.1), (3.2) to account for the processes of transcription, translation and transport. This lead to a system of delay differential equations, which can be written as:

$$\frac{d[m]}{dt} = \frac{\alpha_m^h}{1+([p(t-\tau_m)]/\hat{p})^h} - \mu_m [m], \tag{3.5}$$

$$\frac{d[p]}{dt} = \alpha_p [m(t-\tau_p)] - \mu_p [p], \tag{3.6}$$

where τ_m and τ_p represent delays. With the addition of these delay terms, Monk (2003) showed that it was possible to obtain sustained oscillations without introducing extra species. These results accurately reflect experimental data well but allow for few questions to be asked of the model. It was discovered recently (in a similar GRN) that there is no substantial delay introduced by the process of transcription itself, but it

was suggested that splicing or nuclear export may cause a delay in the negative feedback (Hanisch et al., 2013).

Chapter 4

A reaction-diffusion model of the Hes1 gene regulatory network

4.1 Introduction

A spatio-temporal model of the Hes1 GRN is developed and studied in this chapter. By simply accounting for the spatial structure of the cell and the diffusion of intracellular molecules we are able to reproduce observed oscillatory behaviour without the introduction of delays to the system.

4.2 Reaction-diffusion model formulation

We begin by introducing the PDE model developed in Sturrock et al. (2011) describing the intracellular interactions between hes1 mRNA and Hes1 protein. We adopt the same notation as the previous chapter, i.e., $[m]$ and $[p]$ denote hes1 mRNA and Hes1 protein concentrations respectively. Indeed, as will become apparent, the model

builds directly on the ODE system presented by equations (3.1) and (3.2). The model is considered on a two-dimensional spatial domain representing a cell, with a separate nucleus and cytoplasm. In the equations below, a subscript n denotes a nuclear concentration and a subscript c denotes a cytoplasmic concentration.

We assume both protein and mRNA are subject to diffusion (introduced in section 2.3.1). Diffusion coefficients are denoted depending on the type of species (either a subscript m for mRNA or p for protein) and location (a subsubscript n for nuclear or c for cytoplasmic). For example, the diffusion coefficient for hes1 mRNA in the nucleus is D_{m_n}. Both protein and mRNA are assumed to undergo linear decay, with parameter μ_m denoting mRNA decay and μ_p denoting protein decay. Production of mRNA takes place by the process of transcription in the nucleus. Our production term for nuclear hes1 mRNA is a Hill-like function which decreases as protein levels in the nucleus increase. In this function, the parameters $\hat{p}$, and h represent, respectively, the concentration of Hes1 protein that reduces the transcription rate to half its basal value, and a Hill coefficient. α_m defines the basal rate of mRNA production in the absence of nuclear protein. It should be noted that this transcription rate implicitly accounts for post-transcriptional modifications such as splicing, polyadenylation and editing, i.e., α_m is the rate by which fully formed messenger RNA is formed in the nucleus. Proteins are translated from mRNA by ribosomes in the cytoplasm, a process that is likely to occur at least some minimal distance from the nuclear membrane. Hence we assume protein production occurs a small distance outside the nucleus with production rate proportional to the amount of cytoplasmic hes1 mRNA, the constant of proportionality being denoted α_p. The full system of equations is therefore given by:

$$\frac{\partial [m_n]}{\partial t} = D_{m_n}\nabla^2[m_n] + \underbrace{\frac{\alpha_m}{1+([p_n]/\hat{p})^h}}_{\text{transcription}} - \mu_m[m_n], \tag{4.1}$$

$$\frac{\partial [m_c]}{\partial t} = D_{m_c}\nabla^2[m_c] - \mu_m[m_c], \tag{4.2}$$

$$\frac{\partial [p_c]}{\partial t} = D_{p_c}\nabla^2[p_c] + H(x,y)\underbrace{\alpha_p[m_c]}_{\text{translation}} - \mu_p[p_c], \tag{4.3}$$

$$\frac{\partial [p_n]}{\partial t} = D_{p_n}\nabla^2[p_n] - \mu_p[p_n], \tag{4.4}$$

where $H(x,y)$ is a function accounting for the localisation of protein production in the ribosomes a distance l from the centre of the nucleus (see Appendix 11.1 for details) and is defined as follows:

$$H(x,y) = \begin{cases} 0, & \text{if } x^2+y^2 \leq l^2, \\ \\ 1, & \text{if } x^2+y^2 > l^2. \end{cases} \tag{4.5}$$

We apply continuity of flux boundary conditions across the (internal) nuclear membrane and zero-flux boundary conditions at the outer cell membrane:

$$D_{m_n}\frac{\partial [m_n]}{\partial \mathbf{n}} = D_{m_c}\frac{\partial [m_c]}{\partial \mathbf{n}} \quad \text{and} \quad [m_n] = [m_c] \quad \text{at the nuclear membrane,} \tag{4.6}$$

$$D_{p_n}\frac{\partial [p_n]}{\partial \mathbf{n}} = D_{p_c}\frac{\partial [p_c]}{\partial \mathbf{n}} \quad \text{and} \quad [p_n] = [p_c] \quad \text{at the nuclear membrane,} \tag{4.7}$$

$$\frac{\partial [m_c]}{\partial \mathbf{n}} = 0 \quad \text{at the cell membrane,} \tag{4.8}$$

$$\frac{\partial [p_c]}{\partial \mathbf{n}} = 0 \quad \text{at the cell membrane,} \tag{4.9}$$

where $\mathbf{n}$ is a unit normal. We also apply zero-initial conditions, i.e.,

$$[m_n] = [m_c] = [p_n] = [p_c] = 0 \quad \text{at} \quad t = 0. \tag{4.10}$$

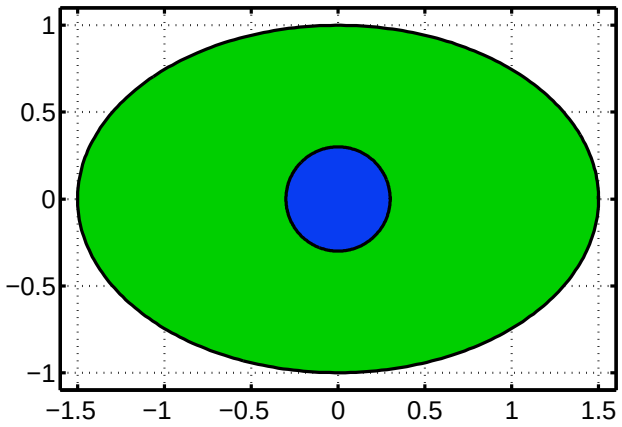

Figure 4.1: *The domain used in numerical simulations of the Hes1 reaction-diffusion model. Spatial units here are non-dimensional, with one non-dimensional spatial unit corresponding to* $10\mu m$*. The cell is an ellipse, centre (0,0), with major and minor axes of* 3 *and* 2*, respectively. The nucleus is shown here as a blue circle, centre (0,0), radius* 0.3*. The cytoplasm (shown in green) is the part of the cell that is outside the nucleus.*

4.3 Numerical simulation results

To numerically solve equations (4.1) – (4.4) subject to conditions (4.6) – (4.10), we used the following procedure. First we non-dimensionalised the model, details of which are provided in Appendix 11.2.2. Then we chose non-dimensional parameter values which yielded oscillatory dynamics and were guided by non-dimensional values used by Monk (2003). We solved the model numerically using the finite element method as implemented in the software package COMSOL 3.5a, using triangular basis elements and Lagrange quadratic basis functions along with a backward Euler time-stepping method of integration. This numerical method of approximating the solution of PDEs is used in all 2-dimensional and 3-dimensional simulations in this thesis. We choose the finite element method due to its ability to handle complicated geometries and boundaries with relative ease. The model equations were solved on the domain shown in Figure 4.1, representing a cell with cytoplasmic and nuclear subdomains. A typical simulation took approximately 55 seconds to run on an iMac with a 2.6 Ghz

Intel core duo processor and 4gb of ram. Finally we calculated dimensional parameter values — these are shown in the third column in Table 4.1. The calculations are described in Appendix 11.2.2. For simplicity, all nuclear and cytoplasmic diffusion coefficients were set equal to the same constant; we denote the dimensional diffusion coefficient by D_{i_j}, which indicates diffusion of species i (mRNA or protein) in location j (nucleus or cytoplasm).

We ran our simulations for a time corresponding to 720 minutes, which is consistent with the longest time for which oscillatory dynamics were observed in the Hes1 GRN following serum treatment (Hirata et al., 2002). We have found ranges of values for all of the parameters such that the system exhibits sustained oscillatory dynamics, where we define such dynamics as being able to observe at least five distinct peaks in the total concentration of the transcription factor in the nucleus. This criteria is motivated by the fact that 3 to 6 cycles of Hes1 protein were observed in response to serum treatment (Hirata et al., 2002). These ranges are given in the fourth column in Table 4.1. In order to find the range for any particular parameter, we varied this parameter whilst holding all the other parameters fixed at their 'default' values, the dimensional versions of which are stated in the third column of Table 4.1. For simplicity we investigated only integer Hill coefficients. The meaning and use of non-integer Hill coefficients is discussed in Zeiser et al. (2007) and Prinz (2010).

Figure 4.2a shows the dynamic evolution of the total concentrations of hes1 mRNA and Hes1 protein over time in the nuclear compartment, while Figure 4.2b shows the total concentrations in the cytoplasmic compartment. Both the nuclear and cytoplasmic compartments show that solutions of the Hes1 reaction-diffusion model exhibit sustained oscillatory dynamics. Although the oscillations appear damped, the numerical solution still displays at least 6 cycles of Hes1 protein which is in keeping with our biologically motivated criteria for 'sustained oscillatory dynamics'. The model yields results in qualitative agreement with biological experiments (Hirata et al., 2002).

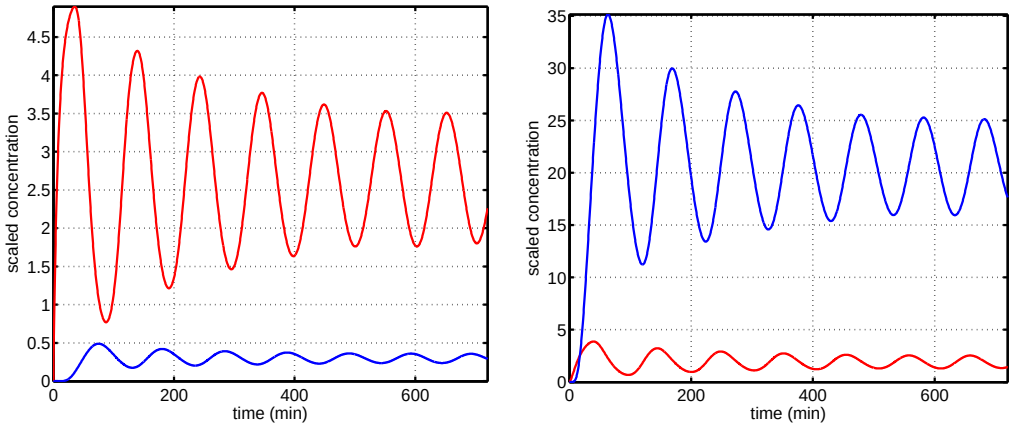

(a) *nuclear compartment* **(b)** *cytoplasmic compartment*

Figure 4.2: *Plots of the total concentrations (in non-dimensional units) of hes1 mRNA (red) and Hes1 protein (blue) in (a) the nucleus and (b) the cytoplasm for the Hes1 reaction-diffusion model. The period of oscillation is approximately* 100 *minutes. Parameter values as per column 3, Table 4.1.*

The plots presented in Figures 4.3a and 4.3b show how the hes1 mRNA and Hes1 protein distributions evolve spatially in the cell from $t = 150$ to 300 minutes. mRNA is produced inside the nucleus and diffuses across the nuclear membrane to enter the cytoplasm (Figure 4.3a). In the cytoplasm, mRNA is translated into protein, which is then able to diffuse back into the nucleus, where it represses the production of its own mRNA. The mRNA concentration has clearly depleted by $t = 180$ and 300 minutes, reflecting the period of the temporal oscillation seen in Figures 4.2a, and 4.2b. As can be seen from Figure 4.3b, there is a delay in the rise of protein concentration after mRNA peaks, for example see $t = 240$ for both mRNA and protein. There appears to be a low to moderate concentration of protein at $t = 240$ minutes, whereas one can observe large quantities of mRNA present in the nucleus and the region of the cytoplasm close to the nucleus. It is not until $t = 270$ minutes that protein reaches high concentration levels (as it did at $t = 150$ to 180 minutes). This is because it takes time for mRNA to be exported and accumulate in the cytoplasm. At $t = 300$ minutes the protein concentration has decreased significantly once again, due to inhibition of mRNA transcription by the protein. This process repeats, producing sustained oscillatory dynamics in space and

Parameter	Description	Value in simulations	Range over which oscillations are observed
D_{i_j}	Diffusion coefficient of species i in compartment j	$3.13 \times 10^{-11}\text{cm}^2\text{s}^{-1}$	$2.67 \times 10^{-11}\text{cm}^2\text{s}^{-1}$ to $1.25 \times 10^{-9}\text{cm}^2\text{s}^{-1}$
α_m	Basal transcription rate of hes1 mRNA	$6.25 \times 10^{-11}\text{Ms}^{-1}$	$\geq 3.87 \times 10^{-12}\text{Ms}^{-1}$
$\hat{p}$	Critical concentration of Hes1 protein	$1.00 \times 10^{-9}\text{M}$	$6.89 \times 10^{-10}\text{M}$ to $1.00 \times 10^{-6}\text{M}$
h	Hill coefficient	5	≥ 4
μ_m	Degradation rate of hes1 mRNA	$1.25 \times 10^{-3}\text{s}^{-1}$	$1.25 \times 10^{-4}\text{s}^{-1}$ to $1.50 \times 10^{-3}\text{s}^{-1}$
α_p	Translation rate of Hes1 protein	0.0555s^{-1}	$\geq 0.0350\text{s}^{-1}$
μ_p	Degradation rate of Hes1 protein	$1.25 \times 10^{-3}\text{s}^{-1}$	$1.25 \times 10^{-4}\text{s}^{-1}$ to $1.50 \times 10^{-3}\text{s}^{-1}$
l	Minimum radial distance of translation from centre of nucleus	$6.32\mu\text{m}$	nuclear membrane ($3\mu\text{m}$) to $6.63\mu\text{m}$

Table 4.1: *Description of parameters in the Hes1 reaction-diffusion model (defined in section 4.2), values used in simulations, and ranges over which sustained oscillatory dynamics are observed.*

time.

4.4 Parameter values

Our range for the diffusion coefficient in Table 4.1 is consistent with two recent spatio-temporal modelling studies of intracellular signalling pathways similar in scope to the present study (Terry et al., 2011; Terry and Chaplain, 2011). Experimentalists have found the diffusion coefficient of soluble proteins in the cytoplasm to be in the range $10^{-9}\text{cm}^2\text{s}^{-1}$ to $10^{-8}\text{cm}^2\text{s}^{-1}$ (Matsuda et al., 2008; Seksek et al., 1997), which is in agreement with the upper bound of our range. There is also a growing body of evidence suggesting that proteins and mRNA molecules are subject to macromolecular crowding, which generates an environment where diffusion is hindered by obstacles and traps (Mendez et al., 2010). Taking this into account would likely increase our lower bound to be consistent with experimental measurements.

The degradation rate μ_m for hes1 mRNA and the degradation rate μ_p for Hes1 protein have both been estimated from experiments. Hirata et al. estimated μ_m to be $4.83 \times 10^{-4}\text{s}^{-1}$ and μ_p to be $5.16 \times 10^{-4}\text{s}^{-1}$ (Hirata et al., 2002). Our parameter ranges for

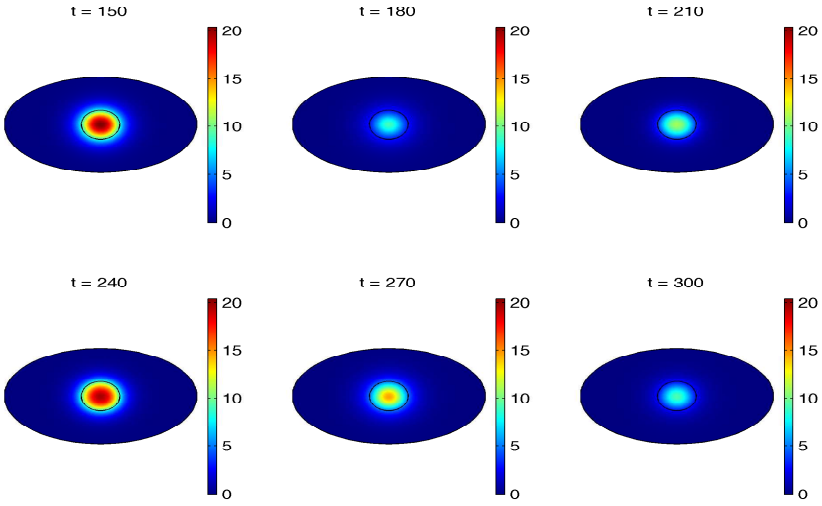

(a) *hes1 mRNA*

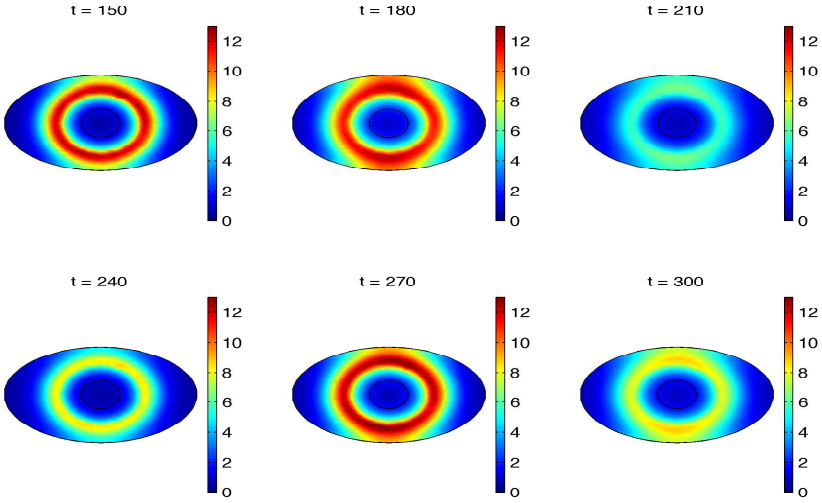

(b) *Hes1 protein*

Figure 4.3: *Plots showing the spatio-temporal evolution of (a) hes1 mRNA and (b) Hes1 protein from times* $t = 150$ *to* 300 *minutes at* 30 *minute intervals for the Hes1 reaction-diffusion model. The concentrations exhibit oscillatory dynamics in both time and space. Parameter values as per column 3, Table 4.1.*

μ_m and μ_p in Table 4.1 contain these experimental estimates.

We mentioned previously in section 3.3.3 that a DDE model of the Hes1 GRN had been explored in Monk (2003). Our range for the Hill coefficient, namely $h \geq 4$, is very similar to the range ($h > 4$) producing sustained oscillatory dynamics in the DDE model in Monk (2003). Note that a larger Hill coefficient corresponds to greater nonlinearity, or co-operativity, in the regulation of hes1 transcription by Hes1 protein. As we mentioned in section 3.2, Hes1 acts as a dimer, which, according to Monk (2003), is enough to suggest that $h = 2$. Hence, the requirement that $h > 2$ implies that there may be interactions between the four binding sites for Hes1 at the hes1 promoter.

Our value for the critical concentration of Hes1, namely $\hat{p} = 10^{-9}$M, is the same as the critical concentration for the zebrafish Her1 protein mentioned in Lewis (2003). Her1 is similar to Hes1 in that both are believed to belong to simple negative feedback loops. The DDE model of the Hes1 GRN in Monk (2003) contains a parameter (namely, p_0) analogous to $\hat{p}$ but representing a number of molecules rather than a concentration. A sensible range is suggested as 10 to 100. By an elementary calculation converting concentration into number of molecules, we find that our value for $\hat{p}$ corresponds to approximately 68 molecules, which clearly lies within the postulated range in Monk (2003).

Our estimate for the translation rate α_p of 0.0555s^{-1} is similar to the rate mentioned in Bernard et al. (2006) of 1min^{-1} or 0.0167s^{-1}. The mRNA production rate α_m has not been measured experimentally, so we leave our estimate of $6.25 \times 10^{-11}\text{Ms}^{-1}$ as a prediction. The distance l of translation from the centre of the nucleus has been studied in Figures 9 - 11 in Sturrock et al. (2011) but a range of values such that sustained oscillatory dynamics occur was not stated. The range for l presented in Table 4.1 reveals that oscillatory dynamics can be obtained when the minimum distance of protein translation coincides with where the cytoplasm meets the nucleus. However, increasing l

too much results in a loss of oscillatory dynamics, implying that the precise spatial location of the ribosome in the cytoplasm is important in our reaction-diffusion model of the Hes1 GRN.

4.5 The influence of spatial dimension

In order to investigate whether the spatial dimension of our model influences its behaviour we must ensure that we vary only the spatial dimension. For this purpose, we now consider a radially symmetric domain for our cell in 1, 2 and 3 spatial dimensions. In 1 spatial dimension, this is simply a line for both nuclear and cytoplasmic compartments. In 2 spatial dimensions, the nucleus is represented by a circle and the cytoplasm is represented by an annulus. In 3 spatial dimensions, the nucleus is represented by a sphere and the cytoplasm is represented by a spherical shell. Furthermore, we scale the production parameters so that the size of the domain plays no role. Hence, the transcription rate, α_m is scaled by the length of the nucleus in 1D, the area of the nucleus in 2D and the volume of the nucleus in 3D. Similarly, the translation rate, α_p is scaled by the length of the cytoplasm in 1D, the area of the cytoplasm in 2D and the volume of the cytoplasm in 3D. In addition, the spatial function localising translation of protein (see equation 4.5) is adjusted appropriately depending on the spatial dimension. We use the same initial and boundary conditions as defined in equations (4.6) – (4.10).

For 1-dimensional simulations we approximate the solution numerically using a backward time centred space finite difference method. This numerical code was adapted from work of Garvie (2007). Figures 4.4 and 4.5 reveal that our model still yields oscillatory behaviour when solved in 1 spatial dimension. Figure 4.4 contains plots of the total concentration of hes1 mRNA and Hes1 protein in both the nucleus and cytoplasm. This Figure reveals the period of oscillation to be approximately 90 minutes. In

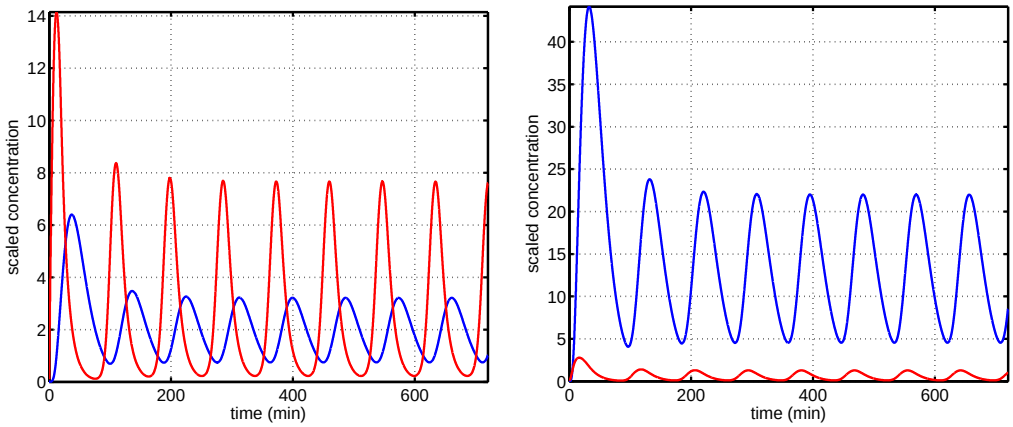

(a) *nuclear compartment* **(b)** *cytoplasmic compartment*

Figure 4.4: *Plots of the total concentrations (in non-dimensional units) of hes1 mRNA (red) and Hes1 protein (blue) in (a) the nucleus and (b) the cytoplasm for the Hes1 reaction-diffusion model solved in 1 spatial dimension. The period of oscillation is approximately 90 minutes. Parameter values as per column 3, Table 4.1 with α_m and α_p scaled appropriately.*

Figure 4.5 we present a plot of the entire spatio-temporal evolution the model in 1D. This spatial plot shows clearly shows sustained oscillatory behaviour for the duration of the simulation. We now compare the 1-dimensional case with higher dimensional simulations.

In Figures 4.6 and 4.7 we reveal that our model still yields oscillatory behaviour when solved in 2 spatial dimensions on a radially symmetric domain. Figure 4.6 contains plots of the total concentration of hes1 mRNA and Hes1 protein in both the nucleus and cytoplasm. Unlike, Figure 4.2 we observe oscillations with consistent amplitude, i.e., the solution tends to a limit cycle and does not reach a steady state. Hence changes in geometry can lead to qualitative changes in the behaviour of our model (we will return to this concept in section 5.7). In Figure 4.7 we present spatial snapshots of the spatio-temporal evolution of the 2D radially symmetric model. The approximate 90 minute period can be seen by comparing $t = 150$ and $t = 240$ minutes for Hes1 protein (Figure 4.7b). Qualitatively, there are no differences between the 1-dimensional and 2-dimensional cases. However, there are some minor quantitative differences. For example, by comparing Figure 4.4a with Figure 4.6a, we discover that more protein

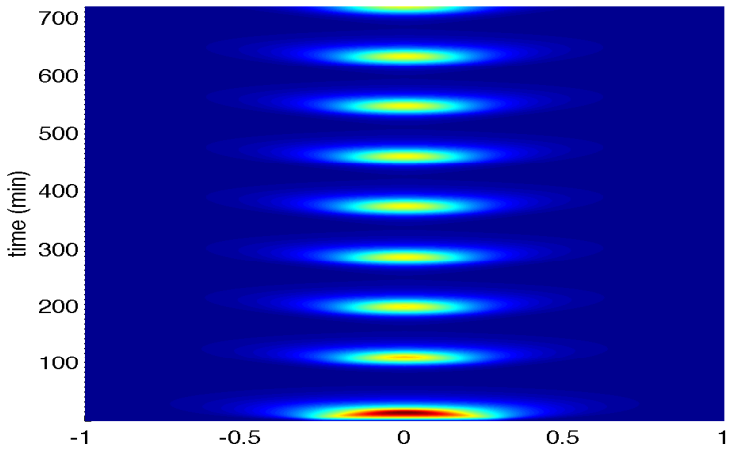

(a) *hes1 mRNA*

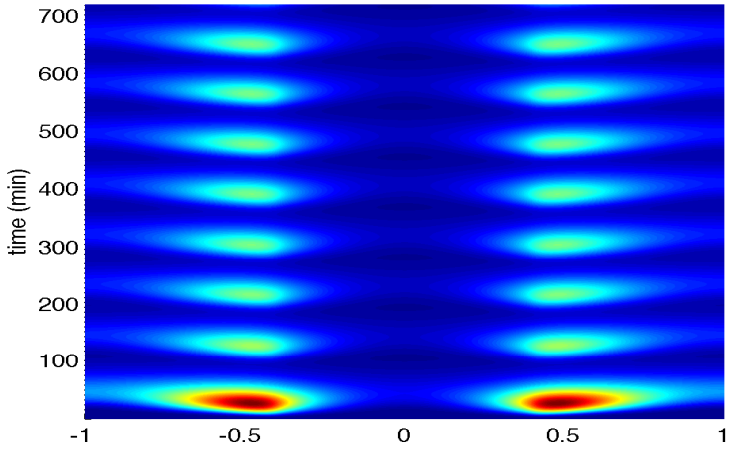

(b) *Hes1 protein*

Figure 4.5: *Plots showing the spatio-temporal evolution of (a) hes1 mRNA and (b) Hes1 protein for the Hes1 reaction-diffusion model solved in 1 spatial dimension. The x-axis represents space (non-dimensional units) and y-axis represents time (in mins). The concentrations exhibit oscillatory dynamics in both time and space. Parameter values as per column 3, Table 4.1 with α_m and α_p scaled appropriately.*

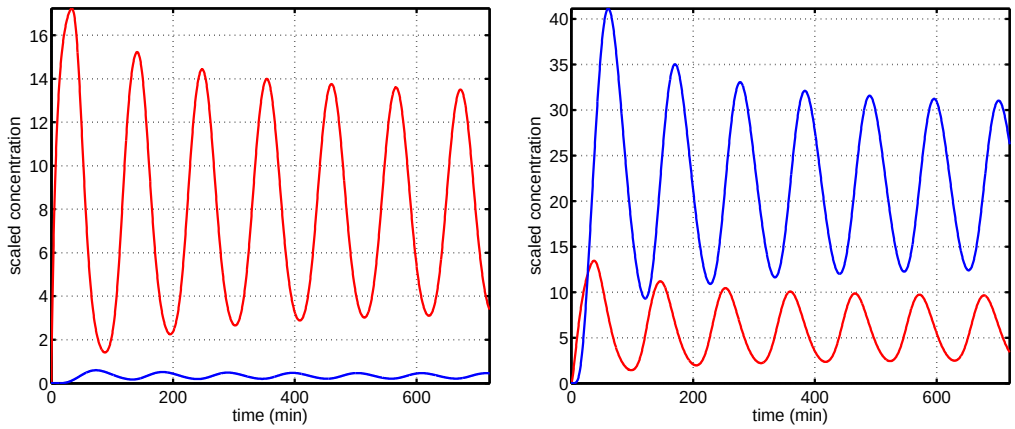

(a) *nuclear compartment* **(b)** *cytoplasmic compartment*

Figure 4.6: *Plots of the total concentrations (in non-dimensional units) of hes1 mRNA (red) and Hes1 protein (blue) in (a) the nucleus and (b) the cytoplasm for the Hes1 reaction-diffusion model solved in 2 spatial dimensions. The period of oscillation is approximately* 90 *minutes. Parameter values as per column 3, Table 4.1 with* α_m *and* α_p *scaled appropriately.*

accumulates in the nucleus in the 1-dimensional case. This is due to the fact that there exist less directions for protein to move into in 1 dimension, and hence it is more likely that protein will reach the nucleus.

Our model retains oscillatory dynamics when solved in 3 spatial dimensions, see Figures 4.8 and 4.9. Figure 4.8 contains plots of the total concentration of hes1 mRNA and Hes1 protein in both the nucleus and cytoplasm. In Figure 4.9 we present spatial snapshots of the spatio-temporal evolution of the 3D radially symmetric model. The approximate 90 minute period can be seen by comparing $t = 210$ and $t = 300$ minutes for hes1 mRNA (Figure 4.9a). Hence, the period of oscillation seems robust to changes in spatial dimension. There are no qualitative differences between the 1-, 2- and 3-dimensional cases. However, as we noted when comparing the 1- and 2-dimensional cases, there exist some quantitative differences between the 1- and 3-dimensional cases and the 2- and 3-dimensional cases. In general, we find that by increasing the spatial dimension, the amount of protein that accumulates in the nucleus lessens and the amount that is retained in the cytoplasm increases. We offer the explanation that as the cytoplasm increases in dimension, there are more directions for protein to move into, and

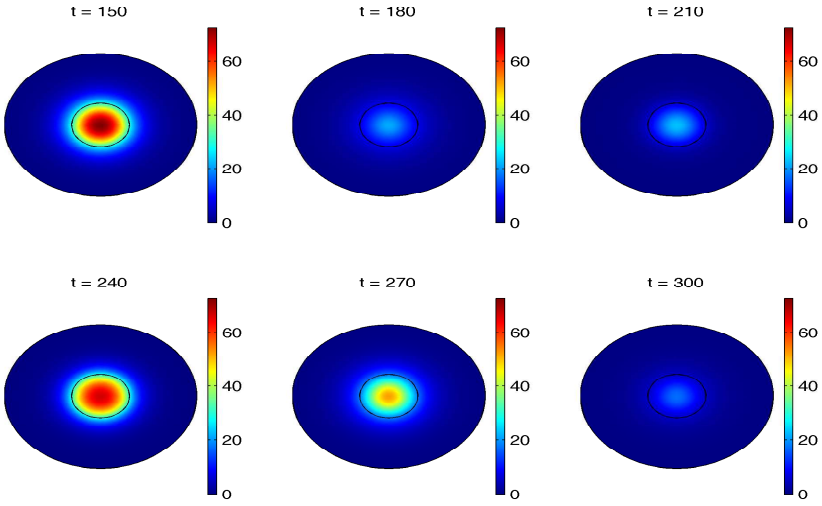

(a) *hes1 mRNA*

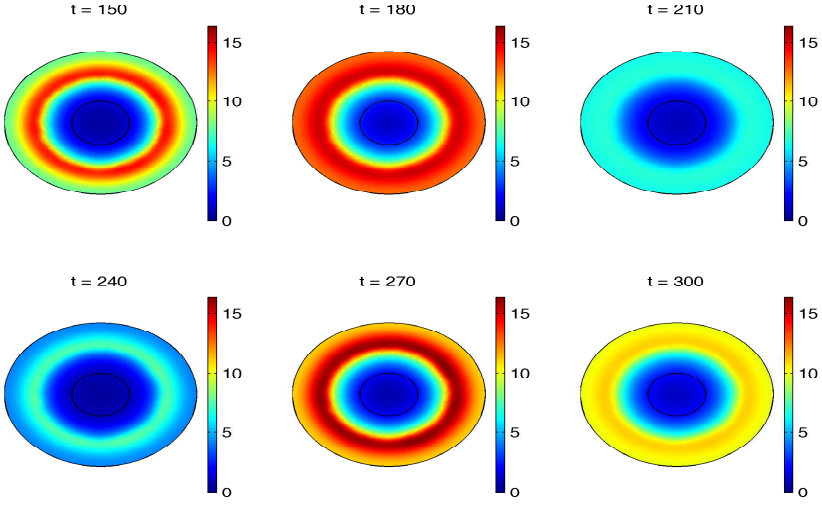

(b) *Hes1 protein*

Figure 4.7: *Plots showing the spatio-temporal evolution of (a) hes1 mRNA and (b) Hes1 protein from times* $t = 150$ *to* 300 *minutes at* 30 *minute intervals for the Hes1 reaction-diffusion model solved in 2 spatial dimensions. The concentrations exhibit oscillatory dynamics in both time and space. Parameter values as per column 3, Table 4.1 with* α_m *and* α_p *scaled appropriately.*

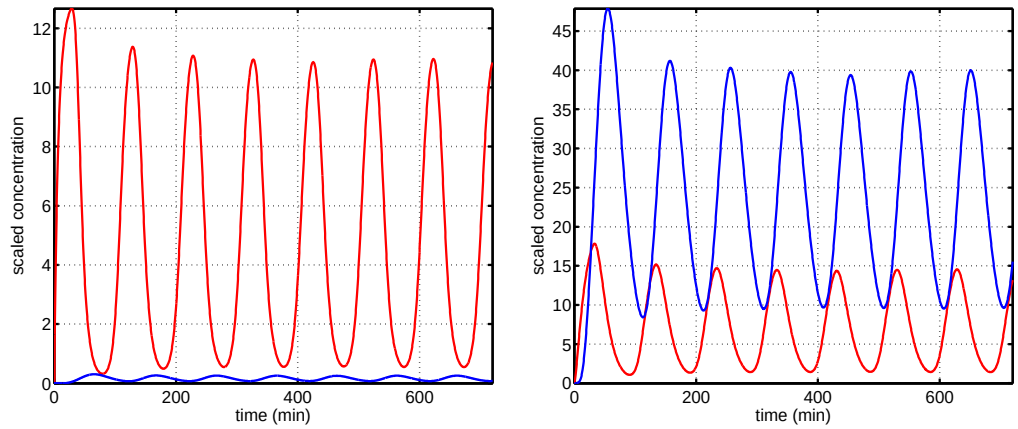

(a) *nuclear compartment* **(b)** *cytoplasmic compartment*

Figure 4.8: *Plots of the total concentrations (in non-dimensional units) of hes1 mRNA (red) and Hes1 protein (blue) in (a) the nucleus and (b) the cytoplasm for the Hes1 reaction-diffusion model solved in 3 spatial dimensions. The period of oscillation is approximately* 90 *minutes. Parameter values as per column 3, Table 4.1 with* α_m *and* α_p *scaled appropriately.*

hence it is less likely that protein will accumulate in the nucleus.

In order to further investigate how the spatial dimension influences the Hes1 reaction-diffusion model, we now present a study of the parameter ranges which are produced by solving the model in different dimensions. In particular, we will study the range of diffusion coefficients, D_{i_j} (see Table 4.1), which yield oscillatory dynamics (5 or more peaks of Hes1 protein in the nucleus). These ranges are presented in Table 4.2. We find that as the number of spatial dimensions is increased, the range of diffusion coefficients yielding oscillatory dynamics becomes broader. Although, we note that the range for 2- and 3-dimensional simulations is almost identical. Hence, for the rest of the thesis we will use 2- or 3-dimensional simulations.

Given the small computational cost of solving a 1-dimensional parabolic PDE system, we are able to produce a numerical 'bifurcation diagram' to illustrate how changing the diffusion coefficient, D_{i_j} influences the behaviour of the system. We computed this by plotting the maximum and minimum value of Hes1 protein recorded in the nuclear compartment from $t = 360$ to 720 mins for 1000 different diffusion coefficients. The

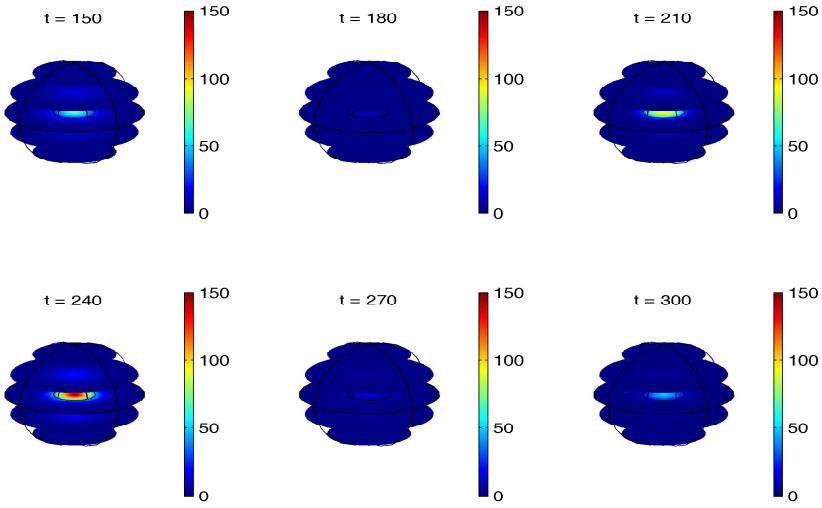

(a) *hes1 mRNA*

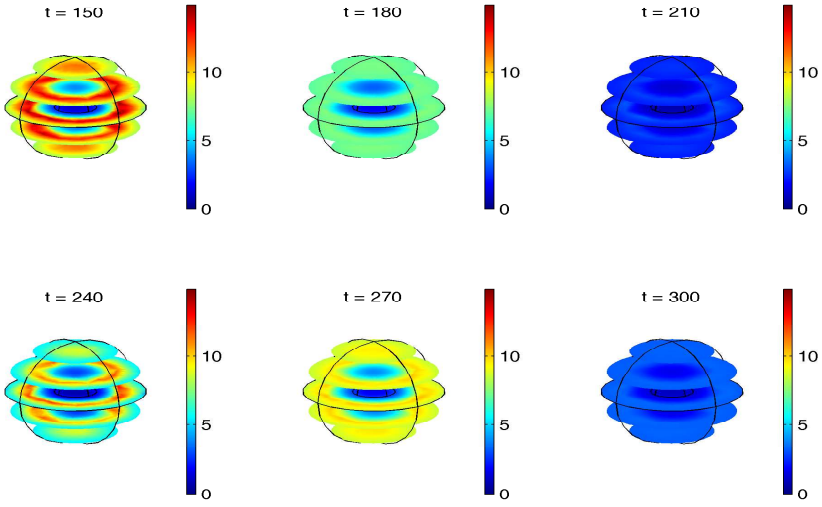

(b) *Hes1 protein*

Figure 4.9: *Plots showing the spatio-temporal evolution of (a) hes1 mRNA and (b) Hes1 protein from times* $t = 150$ *to* 300 *minutes at* 30 *minute intervals for the Hes1 reaction-diffusion model solved in 3 spatial dimensions. The concentrations exhibit oscillatory dynamics in both time and space. Parameter values as per column 3, Table 4.1 with* α_m *and* α_p *scaled appropriately.*

Spatial dimension	Range of diffusion coefficient, D_{i_j}
1	$1.25 \times 10^{-11}\text{cm}^2\text{s}^{-1}$ to $8.33 \times 10^{-10}\text{cm}^2\text{s}^{-1}$
2	$2.08 \times 10^{-11}\text{cm}^2\text{s}^{-1}$ to $1.96 \times 10^{-9}\text{cm}^2\text{s}^{-1}$
3	$2.08 \times 10^{-11}\text{cm}^2\text{s}^{-1}$ to $2.00 \times 10^{-9}\text{cm}^2\text{s}^{-1}$

Table 4.2: *List of spatial dimensions for which the Hes1 reaction-diffusion GRN model is solved, and ranges of diffusion coefficients which yield oscillatory dynamics.*

time period was chosen to avoid any transient behaviour induced by the zero initial conditions — this time period also reflects the timespan over which oscillations were observed (i.e., 3 to 6 120 minute cycles). Note that the range of values may appear inconsistent with those presented in row 1, Table 4.2 because the same criteria for oscillatory dynamics is not applied. As can be seen in Figure 4.10, if the diffusion coefficient is too small the maximum scaled concentration value is the same as the minimum scaled concentration value, i.e., a steady state solution is obtained. By increasing the diffusion coefficient a 'Hopf' bifurcation is produced and the system produces oscillatory dynamics (maximum and minimum concentration values are no longer equal). If we increase the diffusion coefficient further, the oscillations cease, and once again we find steady state values of Hes1 protein in the nucleus. Hence, if the diffusion coefficient is too small or too large we no longer observe oscillatory behaviour. We can understand this by considering the behaviour of the system in two extreme cases. When D_{i_j} is very small (i.e., less than the lower bound presented in Table 4.2), protein remains in the cytoplasm and mRNA remains in the nucleus, i.e., the species remain in the compartment where they were originally synthesised. When D_{i_j} is very large (i.e., larger than the upper bound presented in Table 4.2), the system becomes 'well-mixed' and we know from section 3.3.2 that it is impossible for oscillatory dynamics to be observed for a similar system.

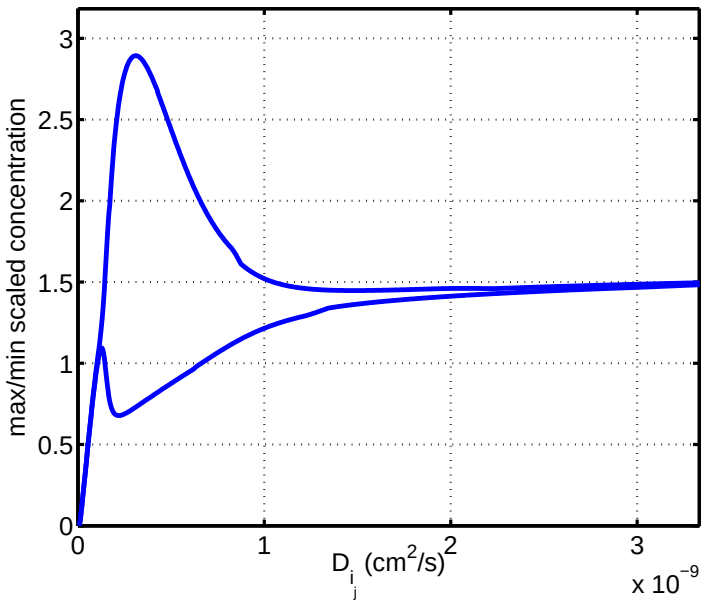

Figure 4.10: *Plot showing how the maximum and minimum scaled concentration of Hes1 protein in the nuclear compartment change as the diffusion coefficient, D_{i_j} is varied.*

4.6 Drug treatment

4.6.1 Inhibition of the proteasome

The proteasome is a large proteolytic protein complex found in all eukaryotic cells that is the primary site for degradation of most intracellular proteins (Alberts et al., 2008). The proteolytic activities of the proteasome can be inhibited by the class of drugs known as proteasome inhibitors (Orlowski and Kuhn, 2008). Our previous simulation results have shown that oscillatory dynamics in the Hes1 system occur only for a suitable protein degradation rate μ_p. Experiments have demonstrated that in the presence of the proteasome inhibitor MG132, hes1 mRNA is transiently induced by a serum treatment, but is then suppressed persistently thereafter (Hirata et al., 2002). We now show the result of inhibiting the proteasome in the Hes1 reaction-diffusion model by reducing the decay rate for Hes1 protein μ_p by a factor of 100. In order to make

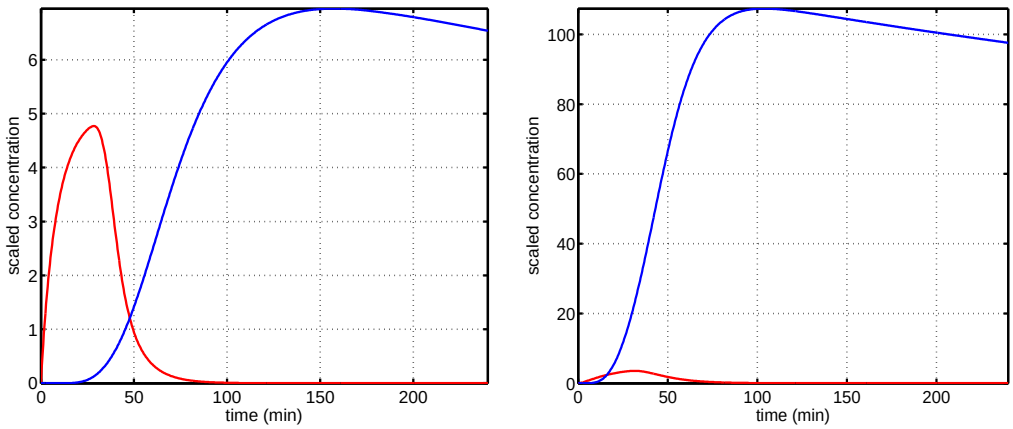

(a) *nuclear compartment* **(b)** *cytoplasmic compartment*

Figure 4.11: *Plots of the total concentrations (in non-dimensional units) of hes1 mRNA (red) and Hes1 protein (blue) in (a) the nucleus and (b) the cytoplasm for the Hes1 reaction-diffusion model when the proteasome is inhibited. No oscillations are observed. Parameter values as per column 3, Table 4.1 with* μ_p *reduced by a factor* 100*.*

our simulation results more readily comparable with the experimental data, we run our simulation for 240 minutes.

Our simulation results of the proteasome inhibition numerical experiment are presented in Figures 4.11 and 4.12. Figure 4.11a shows a plot of the total concentrations of hes1 mRNA and Hes1 protein in the nucleus over time, while Figure 4.11b shows the corresponding total concentrations in the cytoplasm. In Figure 4.12 we reveal the spatio-temporal evolution of the mRNA and protein concentrations (in response to proteasome inhibition) respectively over the same time period. We make the local concentration colour bars identical for mRNA and protein species so a more direct comparison can be made. We can see large quantities of protein almost everywhere in the cell and in contrast we can see almost no mRNA anywhere. Furthermore, as can be seen from all these plots, no oscillations in the concentration levels are observed, in line with the experimental results of Hirata et al. (2002).

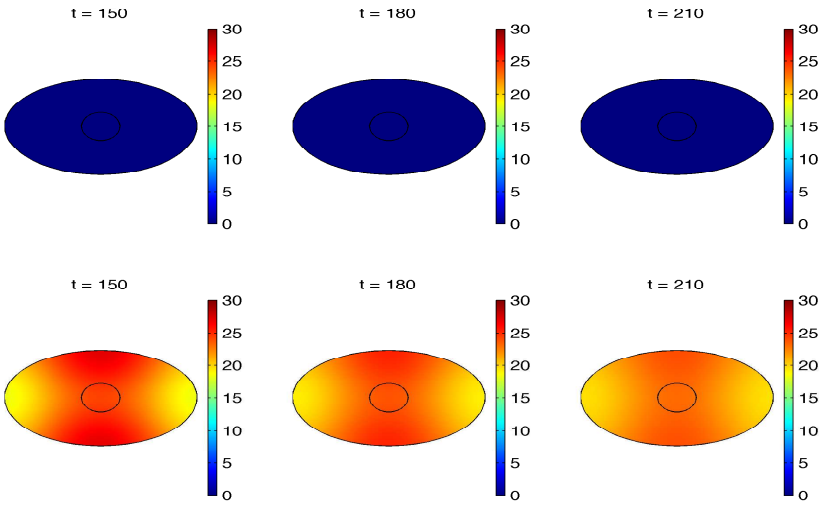

Figure 4.12: *Plots showing the spatio-temporal evolution of hes1 mRNA (first row) and Hes1 protein (second row) from times* $t = 150$ *to* 210 *minutes at* 30 *minute intervals for the Hes1 reaction-diffusion model when the proteasome is inhibited. Hes1 protein is distributed almost evenly throughout the cell (with slightly lower concentrations at the tips) for each time point. hes1 mRNA concentration is so low it is not visible. Parameter values as per column 3, Table 4.1 with* μ_p *reduced by a factor* 100*.*

4.6.2 Translation inhibition

Treating cells with the drug cycloheximide inhibits the key process of translation in cells. Cycloheximide functions by interfering with the translocation step in protein synthesis (movement of two tRNA molecules and mRNA in relation to the ribosome) thus blocking translational elongation. Cycloheximide is widely used in biomedical research to inhibit protein synthesis in eukaryotic cells studied *in vitro*. It is inexpensive and works quickly. Experiments have been performed in fibroblast cells to monitor levels of hes1 mRNA in response to this treatment. In the experiments a sustained increase of hes1 mRNA levels is reported (Hirata et al., 2002). We mimic this experiment with our model by decreasing α_p by a factor of 100 and running our simulation for 300 minutes.

Our simulation results of the translation inhibition numerical experiment are presented in Figures 4.13 and 4.14. Figure 4.13a shows a plot of the total concentrations of

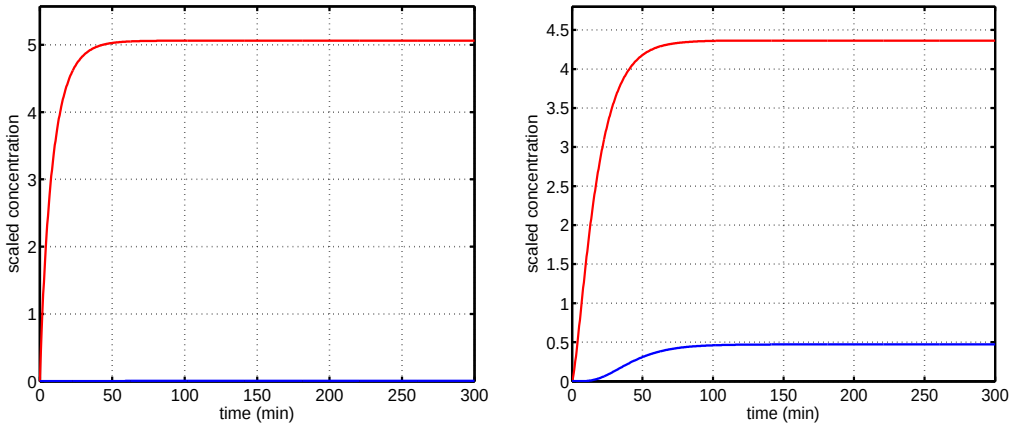

(a) *nuclear compartment* **(b)** *cytoplasmic compartment*

Figure 4.13: *Plots of the total concentrations (in non-dimensional units) of hes1 mRNA (red) and Hes1 protein (blue) in (a) the nucleus and (b) the cytoplasm for the Hes1 reaction-diffusion model when translation is inhibited. No oscillations are observed. Parameter values as per column 3, Table 4.1 with* α_p *reduced by a factor* 100*.*

hes1 mRNA and Hes1 protein in the nucleus over time, while Figure 4.11b shows the corresponding total concentrations in the cytoplasm. Finally, Figure 4.14 shows the spatio-temporal evolution of the mRNA and protein concentrations respectively over the same time period. Again, we use the same local concentration colour bars for easier comparison between the two species. In contrast to the proteasome inhibition numerical experiment, we find large quantities of mRNA within the cell (particularly in the nucleus and the part of the cytoplasm close to the nucleus). As can be observed from all these plots, no oscillations in the concentration levels are observed, in line with the experimental results of Hirata et al. (2002).

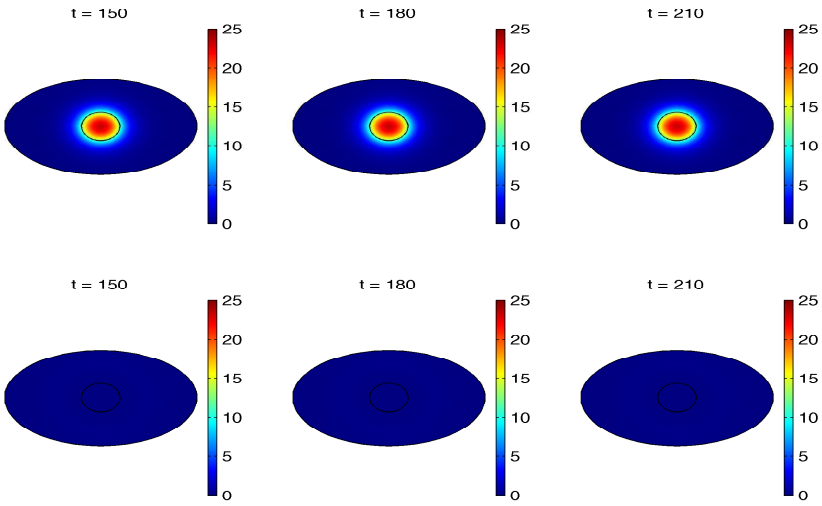

Figure 4.14: *Plots showing the spatio-temporal evolution of hes1 mRNA (first row) and Hes1 protein (second row) from times* $t = 150$ *to* 210 *minutes at* 30 *minute intervals for the Hes1 reaction-diffusion model when translation is inhibited. hes1 mRNA is found in high concentration in the nucleus. Hes1 protein concentration is so low it is not visible. Parameter values as per column 3, Table 4.1 with* α_p *reduced by a factor* 100*.*

4.7 The influence of extrinsic noise: exploring model dependence on initial conditions

Until now we have used zero initial conditions (ICs) for our numerical simulations of the Hes1 reaction-diffusion model. This may be inappropriate given the highly heterogeneous nature of cells. To find two cells with the exact same amount and spatial distribution of proteins and mRNAs at the same point in time is very unlikely. Hence, in this section a study of the influence of random initial conditions is presented. Initial conditions are selected by the following procedure. First, from our simulations with zero initial conditions (see Figure 4.2), the mean values for the total concentrations of hes1 mRNA and Hes1 protein in the nucleus ($mean_{m_n}$, $mean_{p_n}$) and cytoplasm ($mean_{m_c}$, $mean_{p_c}$) are obtained. Using these mean values, we define random initial

condition vectors ($\mathbf{m_{n_{init}}}$, $\mathbf{m_{c_{init}}}$, $\mathbf{p_{n_{init}}}$, $\mathbf{p_{c_{init}}}$) as:

$$\mathbf{m_{n_{init}}} \sim \mathcal{N}(mean_{m_n}, mean_{m_n}/10), \tag{4.11}$$

$$\mathbf{m_{c_{init}}} \sim \mathcal{N}(mean_{m_c}, mean_{m_c}/10), \tag{4.12}$$

$$\mathbf{p_{n_{init}}} \sim \mathcal{N}(mean_{p_n}, mean_{p_n}/10), \tag{4.13}$$

$$\mathbf{p_{c_{init}}} \sim \mathcal{N}(mean_{p_c}, mean_{p_c}/10). \tag{4.14}$$

We then randomly generated initial conditions (using the *randn* function in MATLAB) for each species, which are uniformly distributed throughout the appropriate compartment. We performed 10 simulations of the Hes1 reaction-diffusion model with random initial conditions sampled from equations (4.12) – (4.14). The result of integrating the total protein concentration over the entire cell is presented in Figure 4.15a and the corresponding mRNA vs protein phase plane in Figure 4.15a. After an initial transient period (which appears dependent on initial conditions), the total concentration level settles into an oscillatory behaviour (or limit cycle). The amplitude, period and even phase are largely unaffected by the change in initial condition. Although this study of random initial conditions is far from exhaustive, we can say the model behaviour appears to be robust to changes in initial conditions.

4.8 Discussion

Dissecting the mechanisms by which transcription factors are regulated within cells is critical to understanding cellular function in health and disease and the opportunities for therapeutic intervention. Results from previous mathematical models have reflected simplified experimental findings but have not distinguished explicitly between spatial compartments within the cell and have not considered (explicitly) spatial movement of molecules. We showed in the previous chapter that an ODE model could not replicate

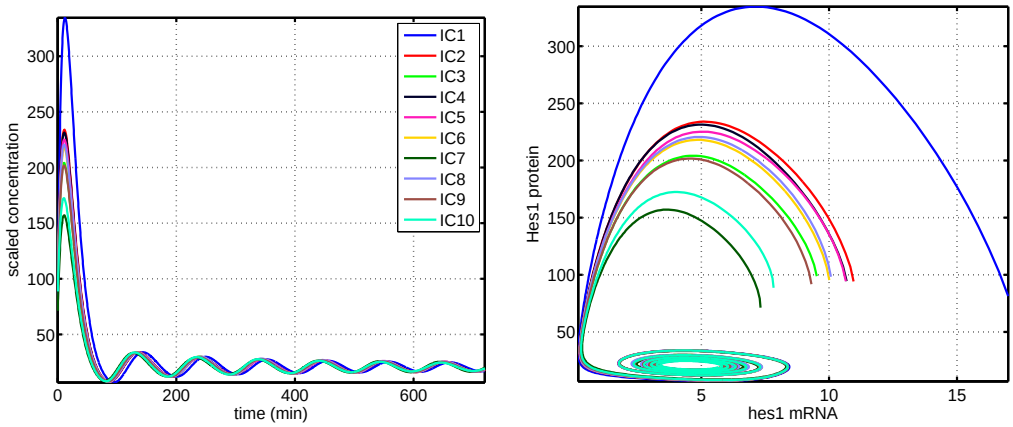

(a) 10 *simulations with different ICs* **(b)** *corresponding phase plane*

Figure 4.15: *Plots of the total concentrations Hes1 protein integrated over the entire cell for the Hes1 reaction-diffusion model with different initial conditions. After an initial transient period induced by the initial conditions, the model appears robust to changes in initial conditions. Parameter values as per column 3, Table 4.1.*

the experimentally observed oscillatory dynamics. We mentioned that previous modellers had worked around this problem by either introducing an unknown additional species or adding delays into the system. Given that spatial localisation is particularly important when modelling transcription factors, which, although produced in the cytoplasm, must be translocated to the nucleus to function. Using PDEs, we can model these aspects of GRNs explicitly.

The simulation results of this chapter have demonstrated the existence of oscillatory dynamics in the canonical negative feedback system (the Hes1 GRN) and have been able to focus on reactions occurring both in the cell nucleus and in the cytoplasm. Undoubtedly, the main advantage of using systems of PDEs to model intracellular reactions is that the PDEs enable spatial effects to be examined explicitly (we will exploit this fact more in the next chapter).

We varied the diffusion coefficients of the mRNAs and proteins and found a range of values for these diffusion coefficients where the system exhibits oscillatory dynamics, i.e., the results of the model have predicted a range of diffusion coefficients for the

molecules involved so that oscillations can be observed. By varying the diffusion coefficients of the molecules, we can vary the flux rates across the nuclear membrane (equivalent to varying nuclear import and export rates), thus granting greater control and allowing a much more in depth analysis of the systems. We were also able to manipulate mathematically the location of the ribosomes (by varying the parameter l, thus controlling where the proteins were synthesised within the cytoplasm. The simulation results revealed an 'optimum' distance outside the nucleus for protein production for which sustained (undamped) oscillations of large amplitude were observed. In other words, if protein translation occurred too far from the centre of the nucleus then sustained oscillatory dynamics were lost. Similar results were obtained by varying the other model parameters, further demonstrating that the oscillations are robust to parameter changes.

We demonstrated that our model is robust to changes in spatial dimension and initial conditions. Such features are desirable for any model — solving in lower dimensions can reduce computational cost and it is unlikely that two cells will have the same mRNA or protein distributions at any point in time. We also remarked that changes in geometry can have important consequences (we will return to this notion in more detail in the next chapter).

The spatial models presented here reflect (qualitatively) experimental findings both *in vitro* (Hirata et al., 2002) and *in vivo* (Hamstra et al., 2006) and mark a conceptual advance in the modelling of intracellular processes. With the emergence of new imaging technologies, validation of spatial models will be possible, with dynamic molecular imaging of subcellular processes on the near horizon.

Chapter 5

The influence of the nuclear membrane, active transport and cell shape on the Hes1 gene regulatory network

5.1 Introduction

In this chapter we consider extensions to the Hes1 reaction-diffusion model presented in chapter 4. Taking advatange of the inherently spatial nature of our modelling approach, we consider extensions that can only be explicitly modelled in a spatial setting.

5.2 Extended model formulation

We begin to extend the Hes1 reaction-diffusion model by first accounting for the structure of the nuclear membrane. Encapsulating the nucleus, the nuclear membrane divides the cell into two compartments, between which there is a constant exchange of molecular material. This physical separation of the nucleus and cytoplasm provides a level of spatial regulation in signal transduction. As mentioned in section 2.3.3, nucleocytoplasmic transport occurs through the nuclear pore complex. The NPCs perforate the two lipid bilayers which form the nuclear membrane and allow for bidirectional transport of a large number of RNA and protein cargoes which vary in size from 1 kDa to nearly 50 MDa (almost 40nm in diameter) (Weis, 2003). The number of functional NPCs varies depending on the growth state of the cell, which in turn affects the overall permeability of the nuclear membrane (Feldherr and Akin, 1991).

In order to model the nuclear membrane explicitly, we need to account for its thickness d (which is also the depth of the NPC) and the diffusion of molecules across it. This effectively allows us to model its permeability. The nuclear membrane thickness has been estimated to be approximately 100nm (Beck et al., 2004). Regarding diffusion across the nuclear membrane, note that since the NPCs are not located everywhere within it, there exist some areas of it that cannot be traversed, and this slows down the average rate at which particles diffuse across it. Molecular crowding may also slow down this average rate. In the restricted space of an NPC, larger molecules, such as proteins, will diffuse more slowly than smaller molecules, such as mRNA (Marfori et al., 2010; Rodriguez et al., 2004). A second explicit step in modelling the nuclear membrane is therefore to assume that diffusion across it is slower than in the cytoplasm or nucleus, with protein diffusion slower than mRNA diffusion across the membrane. Although diffusion coefficients for cytoplasmic, nuclear, and nuclear-embedded proteins have been estimated experimentally (Klonis et al., 2002), we are not aware of

experimental estimates for diffusion rates across the NPCs for hes1 mRNA and Hes1 protein. Therefore, still assuming (as we did at the end of section 6.2) that the nuclear and cytoplasmic diffusion coefficients are the same constant D_{i_j}, we shall simply choose $D_m = D_{i_j}/5$ and $D_p = D_{i_j}/15$ for the nuclear membrane diffusion coefficients for hes1 mRNA and Hes1 protein, respectively. In summary, we can take into account nuclear membrane thickness and slower diffusion across it by replacing the boundary conditions in (4.6) and (4.7) by those for a thin boundary layer of width d, defined by:

$$D_{m_n}\frac{\partial[m_n]}{\partial\mathbf{n}} = \frac{D_m([m_n]-[m_c])}{d}, \tag{5.1}$$

$$D_{m_c}\frac{\partial[m_c]}{\partial\mathbf{n}} = \frac{D_m([m_c]-[m_n])}{d}, \tag{5.2}$$

$$D_{p_c}\frac{\partial[p_c]}{\partial\mathbf{n}} = \frac{D_p([p_c]-[p_n])}{d}, \tag{5.3}$$

$$D_{p_n}\frac{\partial[p_n]}{\partial\mathbf{n}} = \frac{D_p([p_n]-[p_c])}{d}. \tag{5.4}$$

The boundary conditions, (5.1) – (5.4), describe the flux across the nuclear membrane. This flux can be thought of as a permeability coefficient (defined as the diffusion coefficient of the species in the nuclear membrane divided by the membrane thickness) multiplied by the concentration difference of the species across the nucleocytoplasmic boundary.

Our second extension to the original reaction-diffusion model is to consider active transport. As we mentioned in section 2.3.2, it is important for transcription factors to be able to move quickly from the cytoplasm to the nucleus, which can be achieved by active transport along microtubules. The microtubules are fibrous, hollow rods that function primarily to help support and shape the cell. For the majority of the cell cycle (i.e., the interphase period), the microtubules are arranged in the cytoplasm as an aster originating from the microtubule-organising centre (MTOC) located close to the nucleus (see Figure 2.4). The microtubules also play a major role in the intracellular

trafficking of macromolecules and organelles (Cole and Lippincott-Schwartz, 1995; Cangiani and Natalini, 2010). This trafficking of cargo molecules occurs as follows: motor proteins bind to the cargoes and then actively transport them along microtubules. Motor proteins can be split into two families – dyneins (which move molecules from the cytoplasm towards the nuclear membrane) and kinesins (which move molecules towards the cell membrane). Motor proteins interact with microtubules via their ATPase domain, while their opposite terminus interacts with the cargo being transported. The movement of proteins along microtubules towards the nucleus can be viewed as a biased random walk. For example, although cargoes bound to dynein mainly move in the direction of the nucleus, there is evidence for detachment and reattachment of cargoes to motor proteins, pauses, and simultaneous attachment to both dynein and kinesin which can change the direction of movement through a "tug-of-war" (Muller et al., 2008; Smith and Simmons, 2001). For simplicity, we shall model active transport of the transcription factor Hes1 as always being directed towards the nucleus. We do this by adding a convection term to the cytoplasmic Hes1 equation, namely equation (4.3), which becomes:

$$\frac{\partial [p_c]}{\partial t} = D_{p_c} \nabla^2 [p_c] - \underbrace{\nabla \cdot (\mathbf{a}\,[p_c])}_{\text{active transport}} + H(x,y)\alpha_p [m_c] - \mu_p [p_c], \tag{5.5}$$

where $\mathbf{a}$ is the convective velocity given by

$$\mathbf{a} = \left[\frac{-ax}{\sqrt{x^2+y^2}}, \frac{-ay}{\sqrt{x^2+y^2}} \right], \tag{5.6}$$

and the parameter a is the convection speed. The vector field $\mathbf{a}$ is depicted in Figure 5.1.

Finally, in order to take into account the location of the MTOC, we modify the domain on which our equations are solved. To be specific, we solve on the domain shown in Figure 5.2. In this domain, the MTOC is located around the circumference of a circle

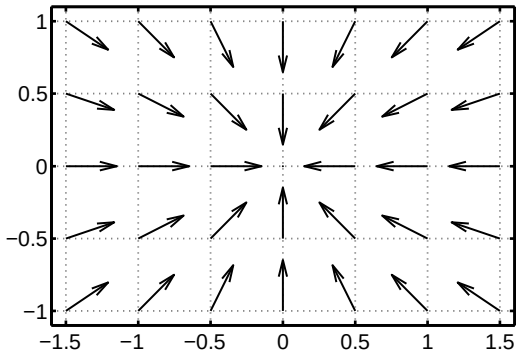

Figure 5.1: *Plot showing the vector field* $\boldsymbol{a}$ *(defined in equation* (5.6)*) modelling the convective effect of the microtubules on protein transport.*

a small distance away from the nucleus. Since microtubules originate from the MTOC and not from the nucleus, we assume that active transport may occur only in the green region outside the MTOC. Hence, in the outer green region, we assume cytoplasmic Hes1 protein satisfies equation (5.5) but in the orange region between the MTOC and the nuclear membrane we assume it satisfies equation (4.3).

5.3 Numerical simulation results

We explore here numerically the extended Hes1 model given by equations (4.1) – (4.4) and (5.5), subject to conditions (4.8) – (4.9) and (5.1) – (5.4) and solved on the domain shown in Figure 5.2. We retained the parameter values used to simulate the original Hes1 model in section 4.3. The diffusion coefficients across the nuclear membrane have already been defined in terms of the diffusion coefficient in the nucleus and cytoplasm, so did not need to be estimated. The nuclear membrane thickness was chosen to be the same as the experimentally measured value of 100nm (Beck et al., 2004). The rate of active transport was chosen to produce numerically stable sustained oscillations. We summarise the dimensional parameter values used for the extended Hes1 model in the second column of Table 5.1. As in the previous chapter, the parameter values we used in numerical simulations are in non-dimensional form. The

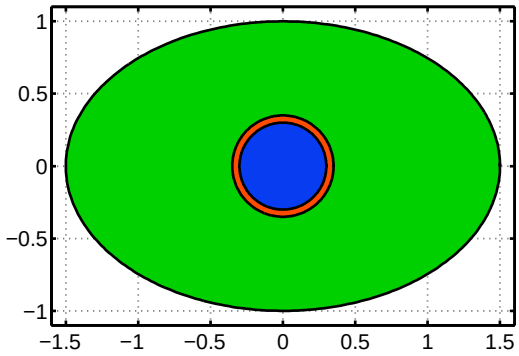

Figure 5.2: *The domain used in numerical simulations of the extended Hes1 model. Spatial units here are non-dimensional, with one non-dimensional spatial unit corresponding to* $10\mu m$*. The cell is an ellipse, centre (0,0), with major and minor axes of 3 and 2, respectively. The nucleus is shown as a blue circle, centre (0,0), radius 0.3. The microtubule-organising centre (MTOC) is located around the circumference of the circle, centre (0,0), radius 0.35, which surrounds the nucleus and is close to it. The cytoplasm is the part of the cell that is outside the nucleus (the green and orange regions) and active transport occurs only in the green region. It does not occur in the orange region because microtubules originate from the MTOC and not from the nucleus.*

non-dimensionalistion calculations are described in Appendix 11.2.2. Ranges of values such that the model exhibits sustained oscillatory dynamics were also found and are stated in the third column of Table 5.1. We use precisely the same biologically motivated criteria for oscillatory dynamics that we used in the previous chapter (5 distinct peaks of Hes1 protein in the nucleus). We run our simulations for 720 minutes which corresponds to the maximum amount of time oscillatory dynamics were observed for.

By comparing Tables 4.1 and 5.1, we see that the parameter ranges yielding sustained oscillatory dynamics are widened by the addition of an explicit nuclear membrane and active transport. Our extended model is therefore both more faithful to the underlying biology and a more robust oscillator. Note in particular that sustained oscillations may occur in the extended model even when the Hill coefficient h is as low as two. As we mentioned above in section 4.4, Hes1 acts as a dimer, which suggests that oscillations should be possible with $h = 2$ (Monk, 2003). We have now found that this is indeed possible, and so it may not be necessary to seek evidence for binding site interactions or other nonlinearities to faithfully model the Hes1 GRN. Furthermore, by fixing $h = 2$

we studied parameter sensitivity and found ranges of the nuclear membrane parameters (i.e., permeability) and active transport speed which produce oscillatory dynamics. As can be seen in Table 5.2, these ranges are quite broad and suggest that allowing for a Hill coefficient of 2 could be a generic feature of systems including a nuclear membrane and active transport. Oscillatory dynamics are observed over a wider range of the parameter l. This is due to the fact that active transport moves proteins created close to the cell membrane towards the nucleus, ensuring enough protein accumulates in the nucleus to shut down hes1 mRNA production.

It has been estimated that motor proteins transport cargo along microtubules at a speed of approximately $5.00 \times 10^{-5}\text{cms}^{-1}$ (Smith and Simmons, 2001). Our value for the rate of active transport in the second column of Table 5.1, namely $a = 1.25 \times 10^{-6}\text{cms}^{-1}$, is lower than this estimate, but it should be kept in mind that our value incorporates not only transport but also implicitly incorporates reactions required for active transport, such as binding to and dissociation from microtubules, as well as competition between newly synthesised molecules of Hes1 protein to attach to microtubules. It should also be kept in mind that molecules can become temporarily stuck on microtubules, slowing down the average rate of active transport (Smith and Simmons, 2001). A more advanced study of active transport would require consideration of stochastic effects, in which context it might be fruitful to take a spatial stochastic approach in a similar manner to Hellander and Lötstedt (2010). In any case, our range of values for the active transport rate such that sustained oscillatory dynamics occur does include the estimate of $5.00 \times 10^{-5}\text{cms}^{-1}$. Moreover our range of values for the nuclear membrane thickness indicate that the numerical solution is robust to variation in this parameter, which is reassuring as this value is likely to vary between cells.

Figure 5.3a shows how the total nuclear concentrations of hes1 mRNA and Hes1 protein vary over time, and Figure 5.3b shows how the total cytoplasmic concentrations of hes1 mRNA and Hes1 protein vary over time. By comparing Figures 5.3a and 5.3b

Parameter	Value in simulations	Range over which oscillations are observed
D_{i_j}	$3.13\times10^{-11}\text{cm}^2\text{s}^{-1}$	$6.67\times10^{-12}\text{cm}^2\text{s}^{-1}$ to $1.13\times10^{-9}\text{cm}^2\text{s}^{-1}$
α_m	$6.25\times10^{-11}\text{Ms}^{-1}$	$\geq 2.50\times10^{-12}\text{Ms}^{-1}$
$\hat{p}$	$1.00\times10^{-9}\text{M}$	$3.17\times10^{-11}\text{M}$ to $7.69\times10^{-7}\text{M}$
h	5	≥ 2
μ_m	$1.25\times10^{-3}\text{s}^{-1}$	$2.08\times10^{-4}\text{s}^{-1}$ to $4.00\times10^{-3}\text{s}^{-1}$
α_p	0.0555s^{-1}	$\geq 2.50\times10^{-3}\text{s}^{-1}$
μ_p	$1.25\times10^{-3}\text{s}^{-1}$	$2.08\times10^{-4}\text{s}^{-1}$ to $3.79\times10^{-3}\text{s}^{-1}$
D_m	$6.25\times10^{-12}\text{cm}^2\text{s}^{-1}$	$\geq 2.50\times10^{-14}\text{cm}^2\text{s}^{-1}$
D_p	$2.08\times10^{-12}\text{cm}^2\text{s}^{-1}$	$\geq 1.67\times10^{-14}\text{cm}^2\text{s}^{-1}$
d	$1\times10^{-5}\text{cm}$	$\leq 4.70\times10^{-4}\text{cm}$
a	$1.25\times10^{-6}\text{cms}^{-1}$	$7.50\times10^{-9}\text{cms}^{-1}$ to $1.08\times10^{-4}\text{cms}^{-1}$
l	$6.32\mu\text{m}$	nuclear membrane (3μm) to 10.7μm

Table 5.1: *Parameter values used in simulations of the extended Hes1 model and ranges over which sustained oscillatory dynamics are observed.*

Parameter	Value in simulations	Range over which oscillations are observed
D_m	$6.25\times10^{-12}\text{cm}^2\text{s}^{-1}$	$\geq 1.38\times10^{-13}\text{cm}^2\text{s}^{-1}$
D_p	$2.08\times10^{-12}\text{cm}^2\text{s}^{-1}$	$\geq 7.92\times10^{-14}\text{cm}^2\text{s}^{-1}$
d	$1.00\times10^{-5}\text{cm}$	$\leq 3.70\times10^{-4}\text{cm}$
a	$1.25\times10^{-6}\text{cms}^{-1}$	$1.92\times10^{-9}\text{cms}^{-1}$ to $8.33\times10^{-5}\text{cms}^{-1}$

Table 5.2: *Nuclear membrane (permeability) and active transport parameter values used in simulations of the extended Hes1 model with fixed Hill coefficient $h = 2$ and ranges over which sustained oscillatory dynamics are observed.*

with, respectively, Figures 4.2a and 4.2b, we see that oscillatory dynamics are retained in the model when a nuclear membrane and active transport are added to it. Yet there are some quantitative differences between our new plots and those for the original model. For example, a greater proportion of Hes1 enters the nucleus in our new plots, for whereas in Figure 4.2 the height of the peaks in nuclear Hes1 were only approximately 1.5% of those in the cytoplasm, Figure 5.3 shows that they are now approximately 33% of those in the cytoplasm. Thus, although our new assumption of slow diffusion across the nuclear membrane hinders the entry of Hes1 into the nucleus, our other new assumption of cytoplasmic active transport of Hes1 is more than enough to overcome this. The increased proportion of Hes1 protein in the nucleus influences the production of hes1 mRNA. To be specific, since Hes1 is a transcription factor which inhibits its own gene, hes1 mRNA production is reduced by the increased proportion of nuclear Hes1 protein. In particular, hes1 mRNA levels in the nucleus drop to zero between consecutive peaks in Figure 5.3a, a result not encountered in Figure 4.2a.

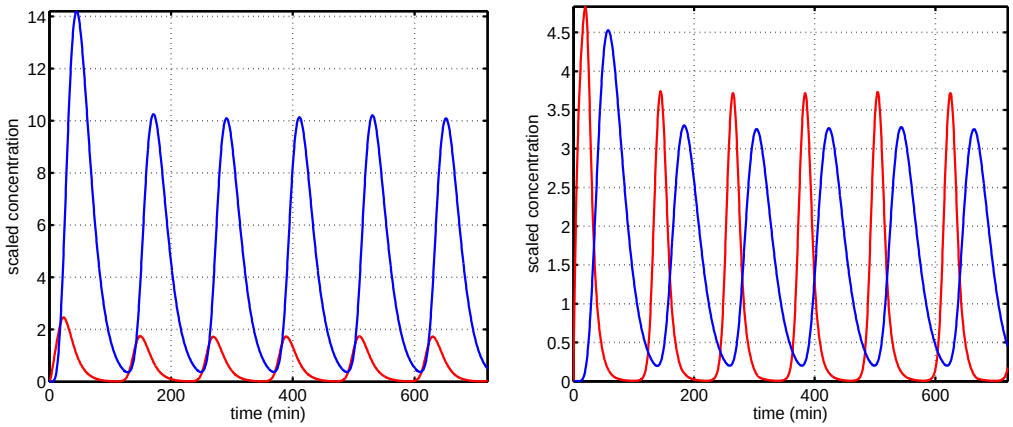

(a) *nuclear compartment* **(b)** *cytoplasmic compartment*

Figure 5.3: *Plots of the total concentrations (in non-dimensional units) of hes1 mRNA (red) and Hes1 protein (blue) in (a) the nucleus and (b) the cytoplasm for the extended Hes1 model. The period of oscillation is approximately 120 minutes. Parameter values as per column 2, Table 5.1.*

We have examined the dependence of the nuclear to cytoplasmic ratio of Hes1 on the speed of active transport. Figure 5.4 shows 100 different values of a, plotted in increments of $2.08 \times 10^{-7}\text{cms}^{-1}$ (the sixth value, $1.25 \times 10^{-6}\text{cms}^{-1}$ is the default value used in simulations). All other parameter values are found in column 2, Table 5.1. The nuclear to cytoplasmic ratio is obtained by taking the mean value of the total concentration of Hes1 protein in the nucleus over a 1000 minute time period and dividing it by the mean total value attained in the cytoplasm over the same time period. The plot shows that the nuclear to cytoplasmic ratio of Hes1 protein increases monotonically as a is increased and tends to a limiting value. We leave these observations as predictions for experimentalists to corroborate.

Figures 5.5a and 5.5b show respectively how hes1 mRNA and Hes1 protein concentrations vary spatially within the cell from times $t = 150$ to 300 minutes. At time $t = 150$ minutes, we see that nuclear hes1 mRNA levels are high and that there is also hes1 mRNA concentrated outside the nucleus. The presence of hes1 mRNA in the cytoplasm causes the production by translation of Hes1 protein, which is actively transported towards the nucleus (see times 150 and 180 minutes). When Hes1 reaches

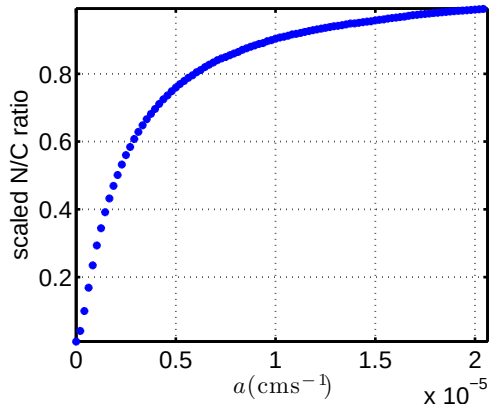

Figure 5.4: *Graph showing nuclear to cytoplasmic (N/C) ratio of Hes1 protein plotted against a, the active transport speed. The plot shows that the nuclear to cytoplasmic ratio of Hes1 protein increases monotonically as a is increased and tends to a limiting value.*

the MTOC directly outside the nucleus, it is no longer actively transported but moves by diffusion alone. Hence Hes1 levels build up directly outside the nucleus. This build up is exacerbated by the nuclear membrane, across which Hes1 moves by slow diffusion. As levels of Hes1 rise in the nucleus, the transcription of hes1 mRNA is inhibited (see times 180 and 210 minutes). Without mRNA transcription, no new Hes1 protein can be created by translation. Hence levels of Hes1 fall throughout the cell by natural degradation (see times 210 and 240 minutes). In the absence of Hes1, mRNA transcription is no longer inhibited and this process resumes (at time 240 minutes). The cycle just described now repeats, and indeed the oscillatory period of two hours (120 minutes) is clear from comparing times 150 and 180 minutes with times 270 and 300 minutes respectively.

When compared to the spatial profiles of the original Hes1 model (see Figures 4.3a and 4.3b) the spatial profiles for hes1 mRNA are not changed qualitatively by our new extensions to the model — the local concentration in the nucleus still reaches a much higher peak than in the cytoplasm. However, the behaviour of Hes1 protein is changed. Instead of building up outside the nucleus as in Figure 5.5b, it spreads out across the

cytoplasm in the absence of active transport and an explicit nuclear membrane (see Figure 4.3b).

5.4 Modelling spatial effects in the nucleus

Until now we have assumed that the diffusion coefficients for all species in each compartment are equal. While this assumption helps reduce the number of parameters in the model, it may not be the most accurate approach. For example it is known that proteins experience macromolecular crowding in the nucleus (Bancaud et al., 2009), so a different nuclear protein diffusion coefficient may be more appropriate. To this end, in Figure 5.6 we present the results of simulations exploring the effect of varying the diffusion coefficients of the molecules in the nucleus. As shown in the plots, changing the diffusion coefficients causes a change in the amplitude and period of the oscillations.

We have also assumed that transcription of hes1 mRNA occurs throughout the nucleus (as if the gene is uniformly distributed). However, a more accurate way to model transcription would be to localise mRNA production to a smaller sub-region of the nucleus. This can be achieved in the model by modifying equation (4.1) as follows:

$$\frac{\partial [m_n]}{\partial t} = D_{m_n} \nabla^2 [m_n] + G(x,y) \left(\frac{\alpha_m}{1 + ([p_n]/\hat{p})^h} \right) - \mu_m [m_n], \tag{5.7}$$

where

$$G(x,y) = \begin{cases} 1, & \text{if } x^2 + y^2 \leq r^2, \\ \\ 0, & \text{if } x^2 + y^2 > r^2, \end{cases} \tag{5.8}$$

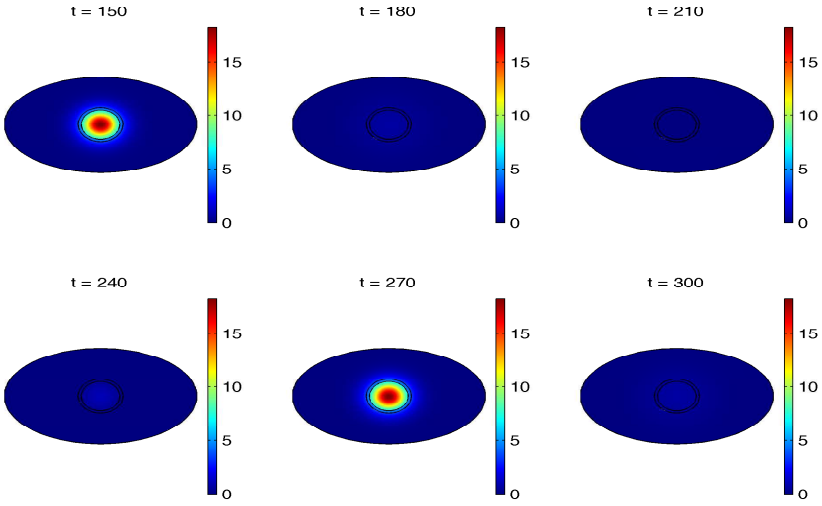

(a) *hes1 mRNA*

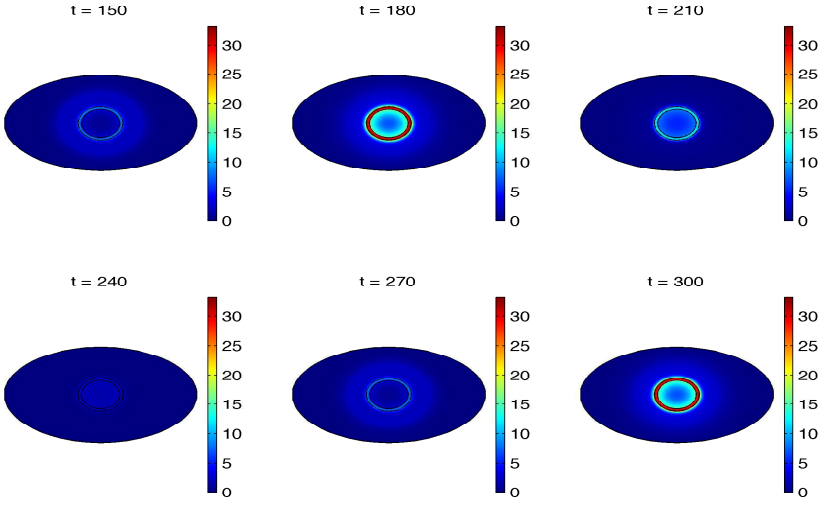

(b) *Hes1 protein*

Figure 5.5: *Plots showing the spatio-temporal evolution of (a) hes1 mRNA and (b) Hes1 protein from times t = 150 to t = 300 minutes at 30 minute intervals for the extended Hes1 model. The concentrations exhibit oscillatory dynamics in both time and space. Parameter values as per column 2, Table 5.1.*

and where r is the production zone radius. Simulation results from this modified model are presented in Figure 5.7. The plots in Figure 5.7(a) show the mRNA concentration in the nucleus over time as we reduce the production zone radius (r) and keep the mRNA production rate (α_m) constant. Oscillatory dynamics are maintained until a critical value of the radius r is reached between 0.90μm and 0.49μm. The lower three plots show that there is a loss of oscillatory dynamics when the production zone is too small. The plots in Figure 5.7(b) show the mRNA concentration in the nucleus over time as we decrease the production zone radius but increase the mRNA production rate (dividing the default value of α_m by the area of the production zone). It is revealed in these plots that oscillatory dynamics can be maintained for smaller values of r.

5.5 Convection as the sole transport mechanism of cytoplasmic Hes1 protein

Our spatio-temporal modelling approach allows us to address questions which cannot be answered using ODE or DDE models. For example, we can investigate different ratios of active transport and diffusion such that sustained oscillatory dynamics occur in the extended Hes1 model. We begin to explore this by decreasing the importance of cytoplasmic protein diffusion relative to its active transport. Setting the diffusion coefficient D_{p_c} to zero we were still able to find sustained oscillatory dynamics for a range of active transport rates a. Representative results are shown in Figure 5.8 for two different values of a. Note that we run our simulations for 800 minutes here so that we can ensure our predefined criteria for oscillatory dynamics are satisfied. Consistent with intuition, the plots shown in Figure 5.8 show that a greater proportion of protein accumulates in the nucleus as the active transport rate a is increased. Our results suggest that sustained oscillatory dynamics will occur as long as sufficient quantities

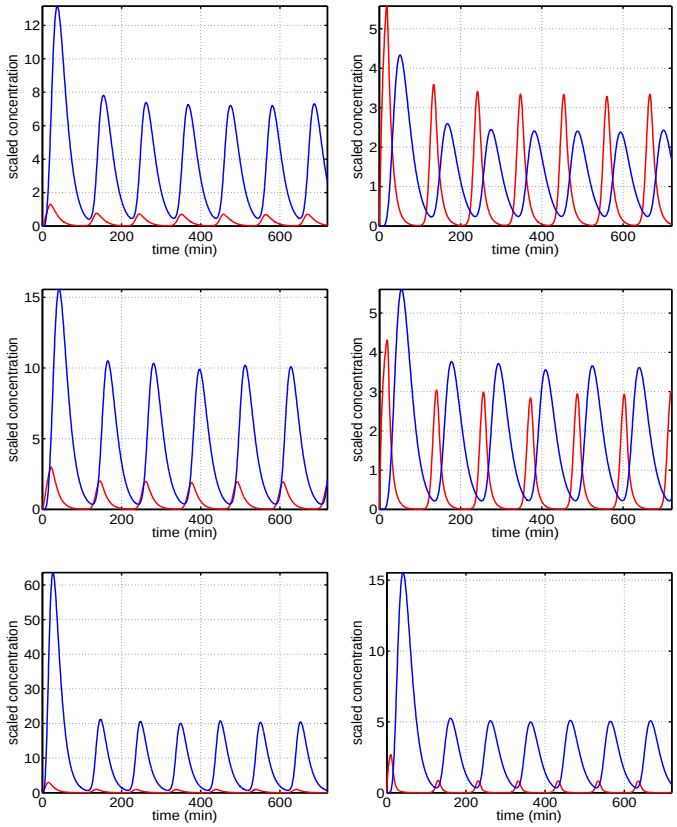

Figure 5.6: *Plots showing the effect on the concentration profiles of varying the mRNA and protein diffusion coefficients. In each row, the left plot shows the total concentrations in the cytoplasm and the right plot shows the total concentrations in the nucleus (Hes1 protein in blue, hes1 mRNA in red). Plots in the first row correspond to the case where all four diffusion coefficients are different, i.e.,* $D_{p_c} = 3.13 \times 10^{-11}\text{cm}^2\text{s}^{-1}$, $D_{m_c} = 2D_{p_c}$, $D_{p_n} = 5D_{p_c}$, $D_{m_n} = D_{p_c}/10$. *Plots in the second row correspond to the case where the nuclear diffusion coefficients are increased, i.e.,* $D_{p_c} = D_{m_c} = 3.13 \times 10^{-11}\text{cm}^2\text{s}^{-1}$ *and* $D_{p_n} = D_{m_n} = 10D_{p_c}$. *Plots in the third row show the result of increasing the diffusion coefficients of mRNA compared with protein diffusion coefficients, i.e.,* $D_{p_c} = D_{p_n} = 3.13 \times 10^{-11}\text{cm}^2\text{s}^{-1}$ *and* $D_{m_c} = D_{m_n} = 10D_{p_c}$. *All other parameter values are found in column 2, Table 5.1.*

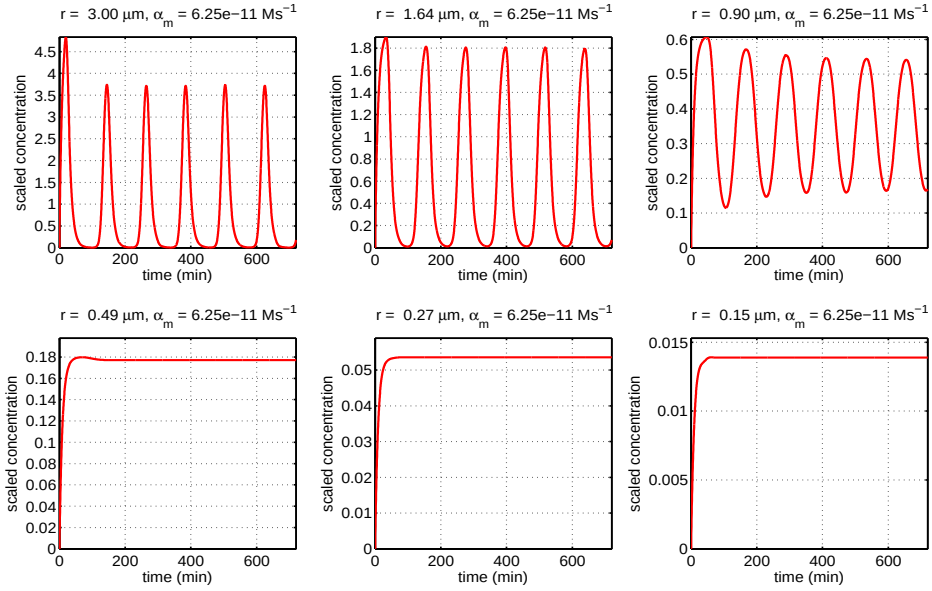

(a) *Parameter r varying, constant value of parameter α_m*

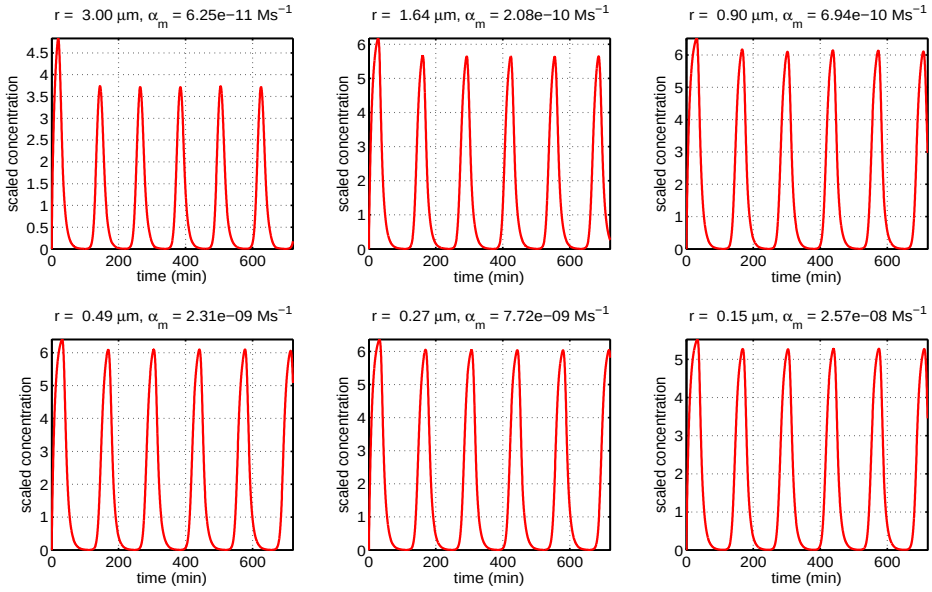

(b) *Both parameter r and parameter α_m varying*

Figure 5.7: *Plots showing the effect on mRNA concentration in the nucleus of localising transcription. In these simulations transcription (i.e., mRNA production) is localised to a region in the nucleus defined by equation (5.8). (a) The radius r of the production zone is decreased while the mRNA production rate α_m is kept constant. As can be seen, oscillatory dynamics are present until r becomes too small. (b) The radius r of the production zone is decreased but the mRNA production rate α_m is increased (dividing the baseline value of α_m by the area of the production zone). As can be observed, oscillatory dynamics are present for all values of r. Parameter values as per column 2, Table 5.1.*

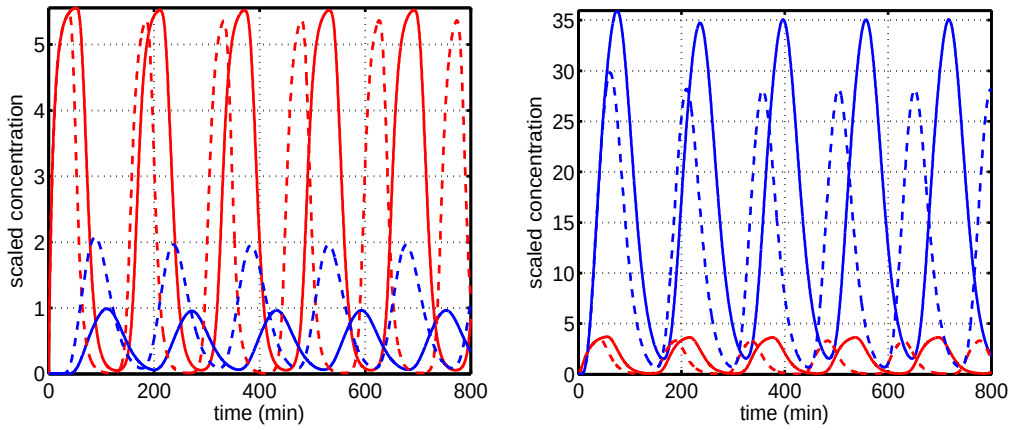

(a) *nuclear compartment* **(b)** *cytoplasmic compartment*

Figure 5.8: *Plots of the total concentrations of hes1 mRNA (red) and Hes1 protein (blue) in (a) the nucleus and (b) the cytoplasm for the extended Hes1 model in the absence of cytoplasmic protein diffusion. Parameter values are as in the second column of Table 5.1, except that* $D_{p_c} = 0$*. The solid lines represent the case where* $a = 1.67 \times 10^{-7} cm\ s^{-1}$ *and the dashed lines represent the case where* $a = 2.50 \times 10^{-7} cm\ s^{-1}$*.*

of Hes1 protein reach the nucleus, regardless of the precise transport mechanism they use to reach it. We leave this result as a prediction of the model since we are not aware of any experiments which can demonstrate this. In the next section, we consider the opposite situation to that considered here, decreasing the importance of active transport relative to diffusion.

5.6 Microtubule disruption numerical experiment

Microtubules are important in a diverse array of cellular functions, ranging from cell division to intracellular trafficking. Consequently microtubule-disrupting drugs are used in cancer therapy and are studied experimentally (Jordan and Wilson, 2004; Kavallaris, 2010; Carbonaro et al., 2011). Although we are not aware of microtubule-disrupting drugs being used on the Hes1 pathway, we shall consider the effect of such drugs in our extended Hes1 model and leave our observations as predictions. Clearly microtubule-disrupting drugs will disrupt active transport along microtubules, so we

Parameter	Value in simulations	Range over which oscillations are observed
D_{i_j}	$3.13 \times 10^{-11}\text{cm}^2\text{s}^{-1}$	$3.33 \times 10^{-11}\text{cm}^2\text{s}^{-1}$ to $1.46 \times 10^{-9}\text{cm}^2\text{s}^{-1}$
α_m	$6.25 \times 10^{-11}\text{Ms}^{-1}$	$\geq 6.87 \times 10^{-11}\text{Ms}^{-1}$
$\hat{p}$	$1.00 \times 10^{-9}\text{M}$	$1.05 \times 10^{-9}\text{M}$ to $1.00 \times 10^{-5}\text{M}$
h	5	≥ 6
μ_m	$1.25 \times 10^{-3}\text{s}^{-1}$	$1.25 \times 10^{-4}\text{s}^{-1}$ to $1.21 \times 10^{-3}\text{s}^{-1}$
α_p	0.0555s^{-1}	$\geq 0.0583\text{s}^{-1}$
μ_p	$1.25 \times 10^{-3}\text{s}^{-1}$	$1.25 \times 10^{-4}\text{s}^{-1}$ to $1.21 \times 10^{-3}\text{s}^{-1}$
D_m	$6.25 \times 10^{-12}\text{cm}^2\text{s}^{-1}$	$\geq 9.58 \times 10^{-12}\text{cm}^2\text{s}^{-1}$
D_p	$2.08 \times 10^{-12}\text{cm}^2\text{s}^{-1}$	$\geq 6.25 \times 10^{-12}\text{cm}^2\text{s}^{-1}$
d	$1 \times 10^{-5}\text{cm}$	$\leq 8.00 \times 10^{-6}\text{cm}$
a	0	-
l	$6.32\mu\text{m}$	nuclear membrane ($3\mu\text{m}$) to $6.24\mu\text{m}$

Table 5.3: *Parameter values used in simulations of the extended Hes1 model in the case where the active transport rate is set to zero, and ranges over which sustained oscillatory dynamics are observed.*

set the active transport rate a equal to zero in our extended model and otherwise retain the parameter values in the second column of Table 5.1 (for convenience, the complete set of parameters is stated also in the second column of Table 5.3). Figure 5.9 shows the total concentrations for Hes1 protein and hes1 mRNA over time. The system no longer satisfies the predefined criteria for sustained oscillatory dynamics (at least 5 distinct peaks in the total concentration of the transcription factor in the nucleus); rather the oscillations are damped. This marks a qualitative change in the dynamics. In a general sense, this is an encouraging result — a qualitative change in dynamics is the type of response we might seek from drug therapy.

Figure 5.9 also shows quantitative changes in the dynamics. For example, a smaller proportion of Hes1 now enters the nucleus (relative to Figure 5.3) — the total concentration of Hes1 in the nucleus is only roughly 1% of that in the cytoplasm in Figure 5.9. This reduction is to be expected since Hes1 is no longer actively transported towards the nucleus.

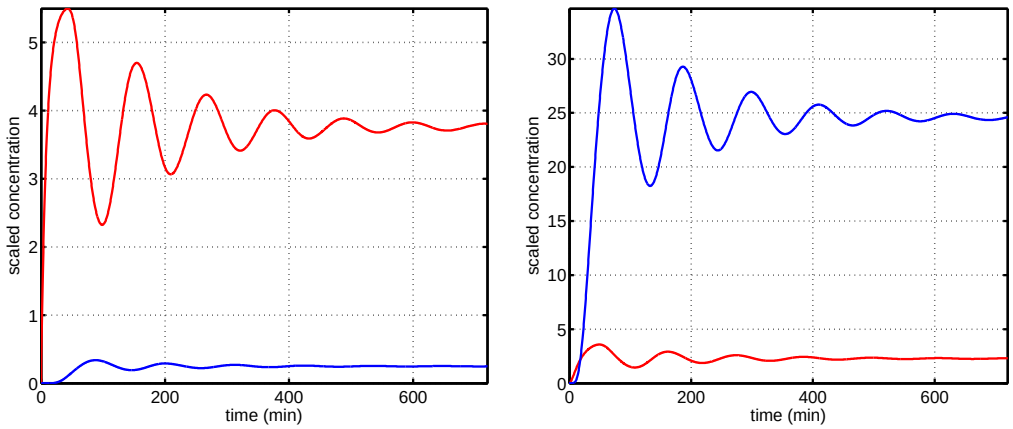

(a) *nuclear compartment* **(b)** *cytoplasmic compartment*

Figure 5.9: *Plots of the total concentrations of hes1 mRNA (red) and Hes1 protein (blue) in (a) the nucleus and (b) the cytoplasm for the extended Hes1 model in the absence of active transport. The concentrations exhibit damped oscillations. Parameter values as per column 2, Table 5.3.*

The damped nature of the oscillations can be seen in Figure 5.10, which, like Figures 4.3 and 5.5 shows the spatio-temporal evolution of hes1 mRNA and Hes1 protein from times $t = 150$ to 300 minutes at 30 minute intervals. For the entire 150 minute time interval mRNA levels are high in the nucleus and protein levels are high in the cytoplasm. The nuclear membrane effectively restricts the location of each species to the compartment in which it is produced. Notice that some of the protein has reached the cell membrane, something that was not observed in the model with active transport (see Figure 5.5).

Although our set of parameter values (second column, Table 5.3) in the extended model without active transport did not yield sustained oscillatory dynamics, we found that by varying each parameter individually then such dynamics could occur. Ranges of values for each parameter such that sustained oscillations occur are stated in the third column of Table 5.3. Note that these ranges are narrower than those presented in Tables 4.1 and 5.1 and that, unlike in Tables 4.1 and 5.1, they do not contain the experimental measurements for the parameters μ_m and μ_p. Furthermore, unlike in Table 5.1, the experimental measurement for d is not contained in the range for d in Table 5.3.

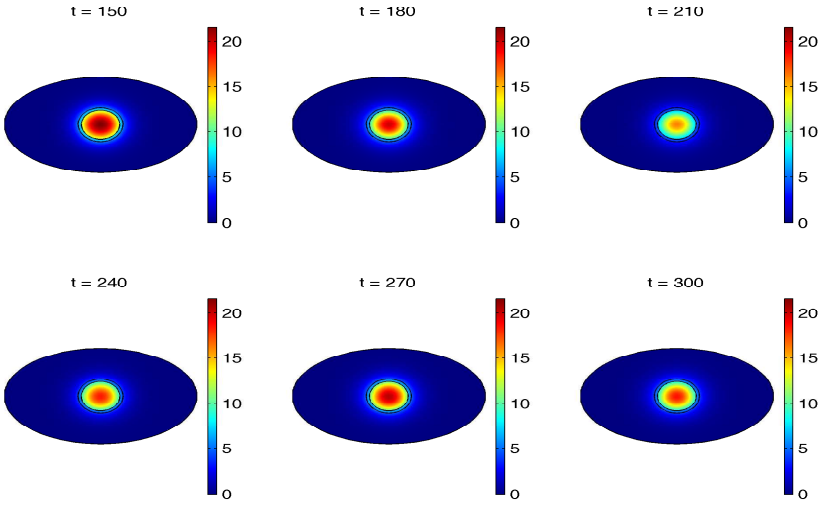

(a) *hes1 mRNA*

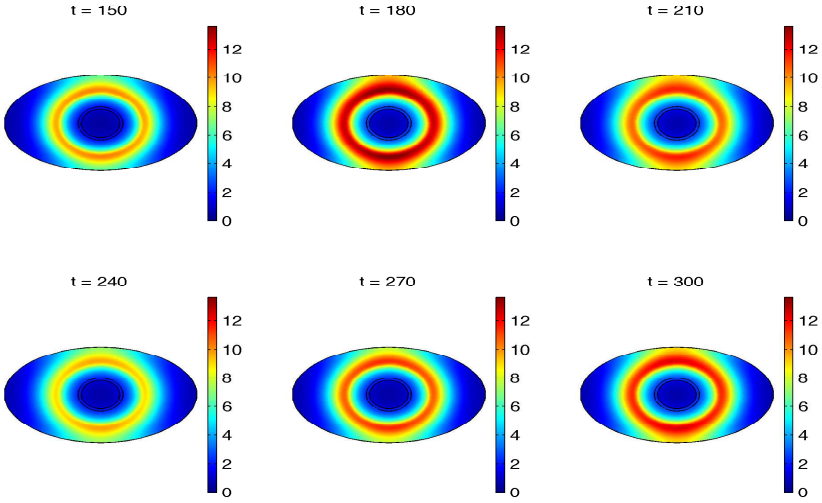

(b) *Hes1 protein*

Figure 5.10: *Plots showing the spatio-temporal evolution of (a) hes1 mRNA and (b) Hes1 protein from times t = 150 to t = 300 minutes at 30 minute intervals for the extended Hes1 model in the absence of active transport. The concentrations exhibit damped oscillations in time and space. Parameter values as per column 2, Table 5.3.*

5.7 The influence of cell shape

As mentioned in section 2.2, cell shape can influence intracellular signal transduction (Meyers et al., 2006; Neves et al., 2008). The influence of cell geometry on the Notch-Delta and NF-κB pathways has recently been investigated by Terry and coworkers, who found through spatio-temporal modelling that oscillatory behaviour in these pathways is to some extent robust to changes in the shapes and relative sizes of the nucleus and cytoplasm (Terry et al., 2011; Terry and Chaplain, 2011). We have performed numerous simulations to study the influence of cell shape on the extended Hes1 model, with parameters as in the second column of Table 5.1. We run our simulations for long enough to check whether our predefined criteria for oscillatory dynamics is satisfied. We present some of these results in Figures 5.11 and 5.12. It is clear from these figures that sustained oscillatory dynamics are strongly robust to changes in cell shape. Such robustness is reassuring since the shape of eukaryotic cells is highly variable (Baserga, 2007; Pincus and Theriot, 2007).

Only one of the geometries in Figures 5.11 or 5.12 shows significant damping after the initial peaks in Hes1 protein and hes1 mRNA total concentrations. This occurs in the second row in Figure 5.12, where the MTOC surrounding the nucleus is significantly increased in size. The increased size of the MTOC reduces the size of the region in which active transport may occur. Hence the results in the second row in Figure 5.12 are similar to those presented in section 5.6 in which the active transport rate is set to zero.

In general, we found that the qualitative behaviour of the extended Hes1 model is much more robust to variety in cell shape than the quantitative behaviour — oscillatory dynamics can be retained when the domain is altered whilst, for example, the proportion of Hes1 that enters the nucleus will change and also the period seems very sensitive to cell shape. Hence, to obtain quantitatively accurate results, we should use a domain

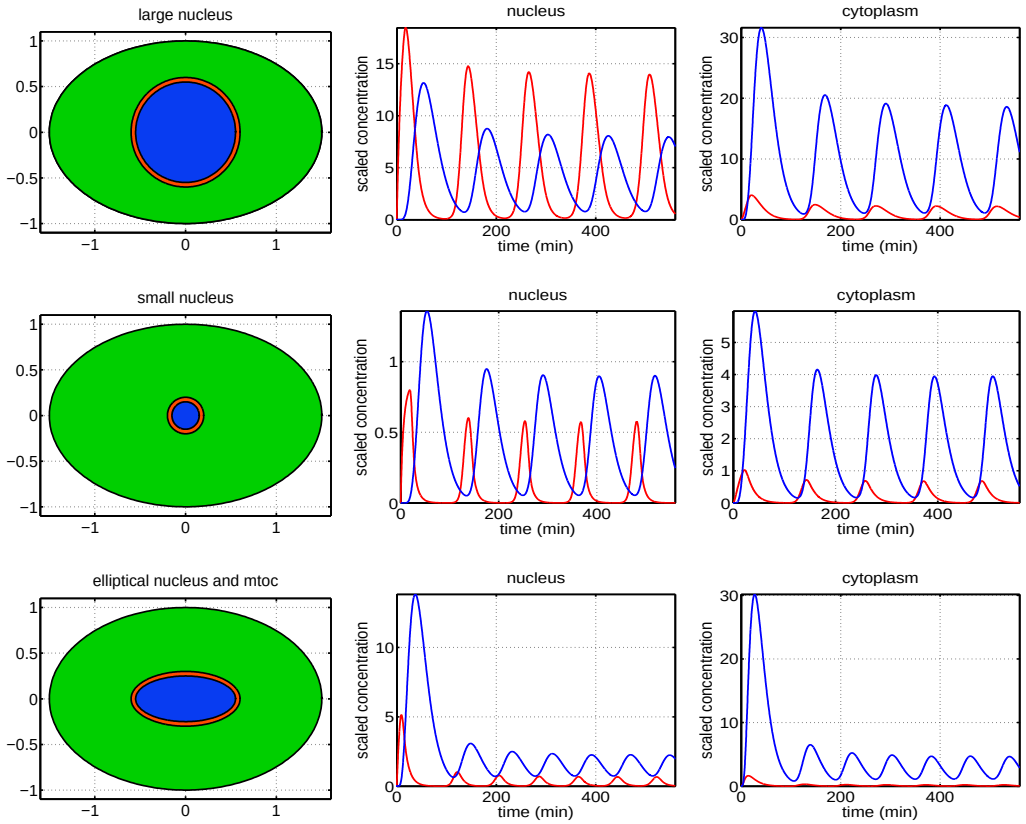

Figure 5.11: *Plots showing the effect on the extended Hes1 model of varying the nuclear shape. In each row, the left plot shows the shape on which we solve, and the middle and right plots show the corresponding numerical results. Spatial units here are non-dimensional, with one non-dimensional spatial unit corresponding to* $10\mu m$*. Total concentrations for Hes1 protein are displayed in blue and for hes1 mRNA in red. Parameter values as per column 2, Table 5.1.*

that exactly matches a living cell.

We explore the effect of using a realistic cell shape in Figures 5.14 and 5.15. For this, we have used an image of an osteosarcoma cell since the Hes1 pathway is known to play a critical role in the development of osteosarcomas (Zhang et al., 2008). The image of the osteosarcoma cell, taken from Davidson (2011), is shown in Figure 5.13a, and the imported domain used for simulations is shown in Figure 5.13b. An additional region was added to account for the MTOC.

The realistic cell domain does not change the solution qualitatively - oscillations are

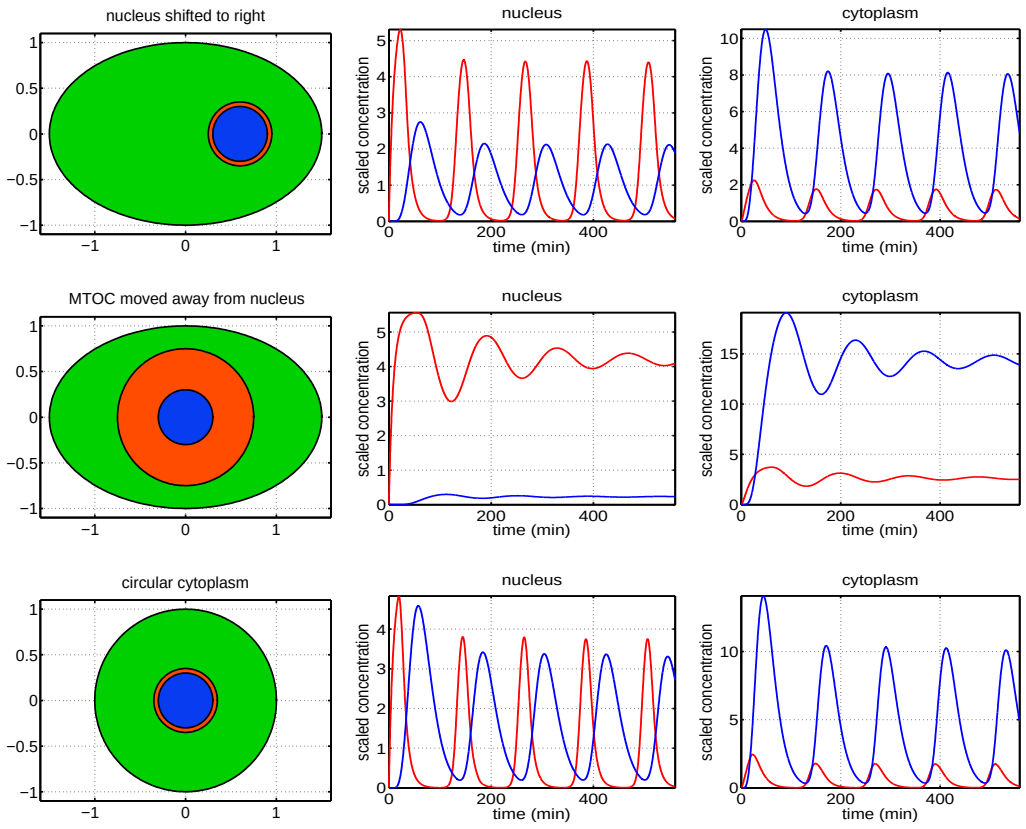

Figure 5.12: *Plots showing the effect on the extended Hes1 model of varying the nucleus position (first row), the MTOC position (second row), and the cell shape (third row). In each row, the left plot shows the shape on which we solve, and the middle and right plots show the corresponding numerical results. Spatial units here are non-dimensional, with one non-dimensional spatial unit corresponding to* $10\mu m$*. Total concentrations for Hes1 protein are displayed in blue and for hes1 mRNA in red. Parameter values as per column 2, Table 5.1.*

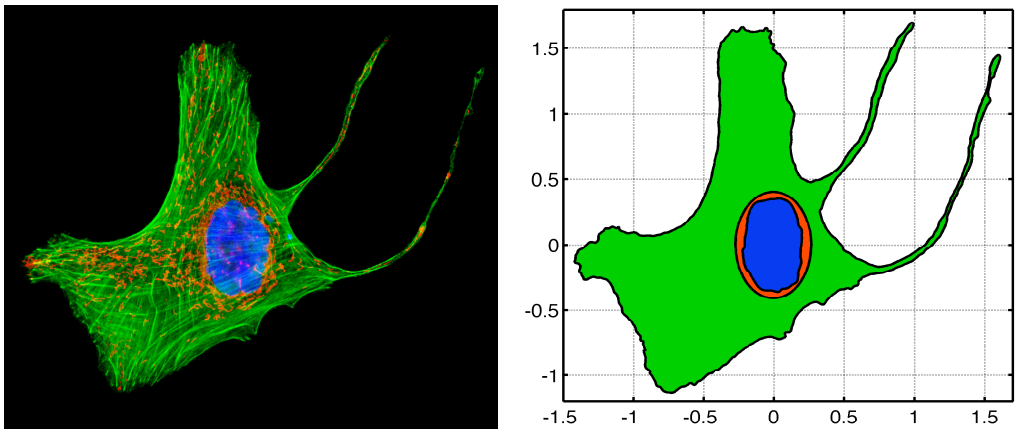

(a) *image of cell* **(b)** *imported cell domain*

Figure 5.13: *Images of (a) an osteosarcoma cell (U-2 OS) (reproduced with permission from Davidson (2011)) and (b) an imported image of this cell with axes displayed in non-dimensional spatial units (one non-dimensional spatial unit corresponds to* $10\mu m$*), which is used as a domain in numerical simulations. A third region directly outside the nucleus was added to the imported domain (shown as orange), the outer boundary of which represents the MTOC cf. Figure 5.2.*

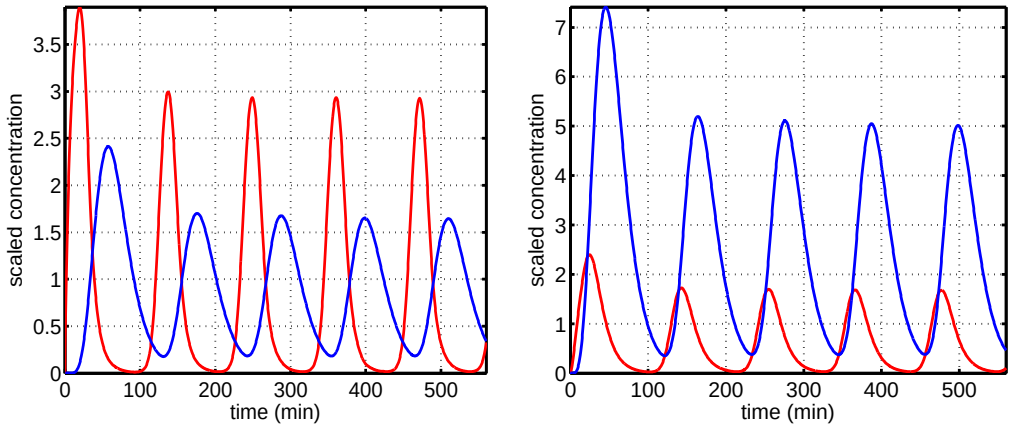

(a) *nuclear compartment* **(b)** *cytoplasmic compartment*

Figure 5.14: *Plots of the total concentrations of hes1 mRNA (red) and Hes1 protein (blue) in (a) the nucleus and (b) the cytoplasm for the extended Hes1 model solved over an osteosarcoma cell domain as shown in Figure 5.13b. The period of oscillation is approximately* 112.5 *minutes. Parameter values as per column 2, Table 5.1.*

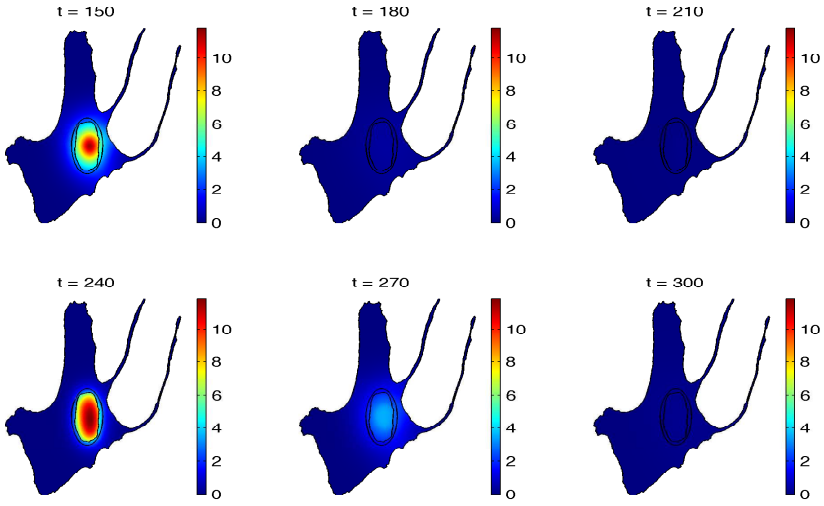

(a) *hes1 mRNA*

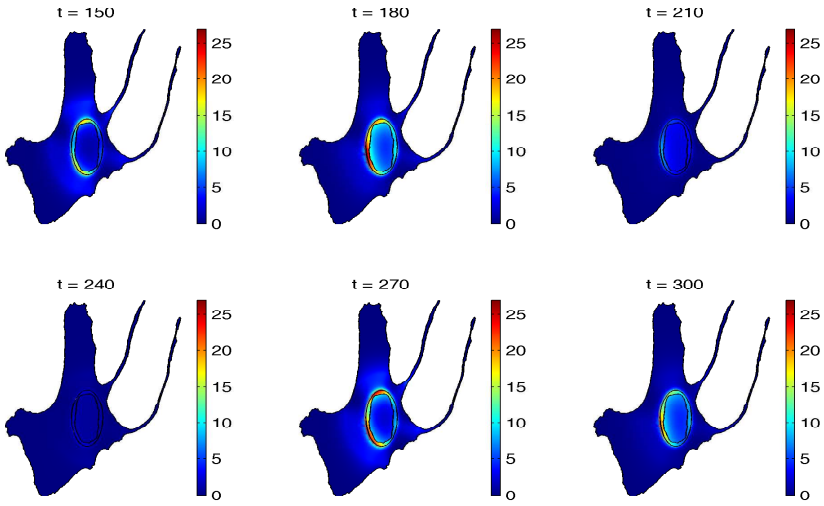

(b) *Hes1 protein*

Figure 5.15: *Plots showing the spatio-temporal evolution of (a) hes1 mRNA and (b) Hes1 protein within the cell from times* $t = 150$ *to* 300 *minutes at* 30 *minute intervals for the extended Hes1 model solved over an osteosarcoma cell domain as shown in Figure 5.13b. The concentrations exhibit oscillatory dynamics in both time and space. Parameter values as per column 2, Table 5.1.*

evident from the total concentration plots of Figure 5.14. However, there are quantitative differences between the total concentration plots in Figure 5.14 and those in Figure 5.3 (where the only difference in the system being solved is the domain used). For instance, the total concentration of Hes1 protein in both the nucleus and cytoplasm is reduced in Figure 5.14 relative to Figure 5.3, and there is also a notable reduction in Hes1 protein total concentration compared to hes1 mRNA total concentration in both the nucleus and cytoplasm. Interestingly, the ratio of nuclear to cytoplasmic protein is retained.

Spatial profiles with the osteosarcoma cell domain are presented in Figure 5.15. Comparing Figures 5.15 and 5.5 allows us to see why the total protein concentration in Figure 5.14 is significantly less than that in Figure 5.3. Whilst protein is produced uniformly around the nucleus in Figure 5.5, this is not the case in the osteosarcoma cell in Figure 5.15 because the nucleus is much nearer to the cell membrane and we have made the assumption that protein is produced a small distance from the nucleus. Protein is mainly produced in the osteosarcoma cell in the areas above and to the left of the nucleus, where there is space for this to occur.

5.8 Drug treatment

5.8.1 Inhibition of the proteasome

As in section 4.6.1 we consider here the impact of proteasome inhibition. We now show the result of inhibiting the proteasome in the extended Hes1 model by reducing the decay rate for Hes1 protein μ_p by a factor of 100. To aid comparison with experimental data we run our simulations for 240 minutes.

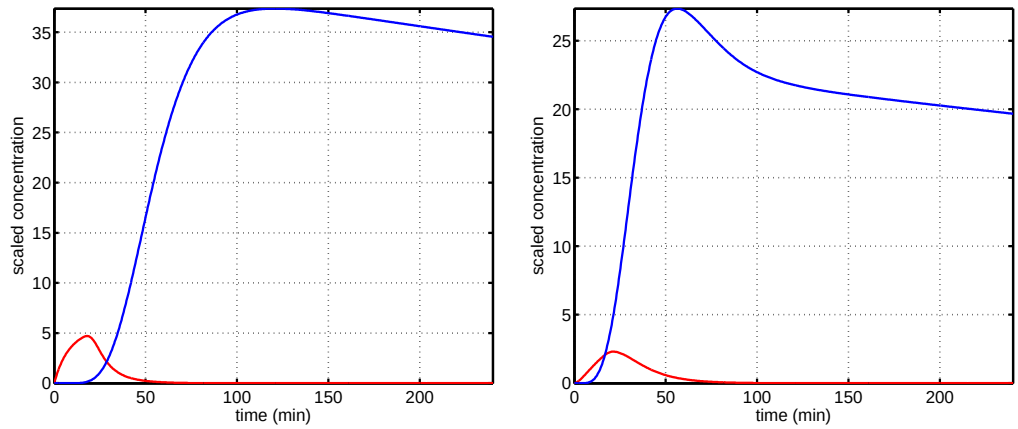

(a) *nuclear compartment* **(b)** *cytoplasmic compartment*

Figure 5.16: *Plots of the total concentrations (in non-dimensional units) of hes1 mRNA (red) and Hes1 protein (blue) in (a) the nucleus and (b) the cytoplasm for the Hes1 extended model when the proteasome is inhibited. No oscillations are observed. Parameter values as per column 2, Table 5.1 with* μ_p *reduced by a factor* 100*.*

Our simulation results of the proteasome inhibition experiment are presented in Figures 5.16 and 5.17. Figure 5.16a shows a plot of the total concentrations of hes1 mRNA and Hes1 protein in the nucleus over time, while Figure 5.16b shows the corresponding total concentrations in the cytoplasm. Finally, Figure 5.17 shows the spatio-temporal evolution of the mRNA and protein concentrations respectively over the same time period. As in section 4.6.1 we do not find oscillations in the concentration levels, which is in line with the experimental results of Hirata et al. (2002). However, unlike in section 4.6.1 the protein accumulates mainly in the nucleus (compare Figure 4.12 with Figure 5.17). The spatial distribution of proteins is not commented on in Hirata et al. (2002), hence we leave the results of our numerical experiment as a prediction of the model. We hope these results will inspire experimentalists to conduct additional experiments.

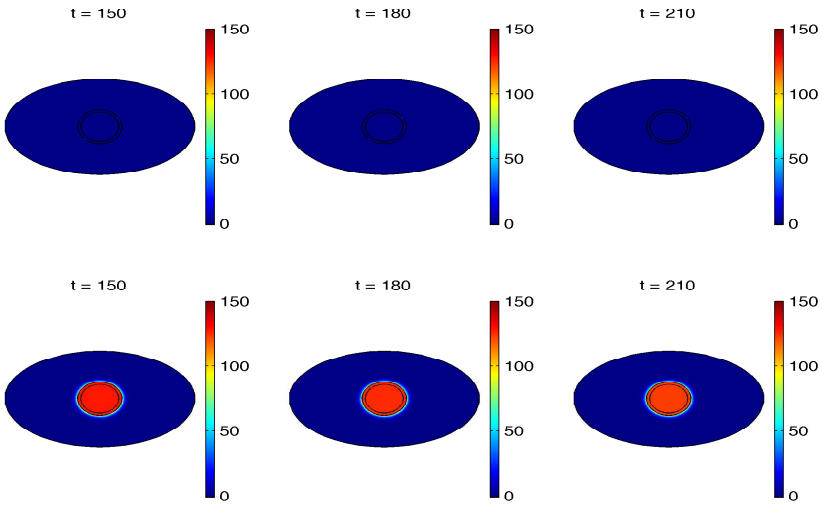

Figure 5.17: *Plots showing the spatio-temporal evolution of hes1 mRNA (first row) and Hes1 protein (second row) from times* $t = 150$ *to* 210 *minutes at* 30 *minute intervals for the Hes1 extended model when the proteasome is inhibited. Hes1 protein is distributed almost almost exclusively in the nucleus and within the MTOC for each time point. hes1 mRNA concentration is so low it is not visible. Parameter values as per column 2, Table 5.1 with* μ_p *reduced by a factor* 100*.*

5.8.2 Translation inhibition

Following section 4.6.2 we now consider the effect of inhibiting the key process of translation for the extended Hes1 model. We mimic this experiment using model by decreasing α_p by a factor of 100 and running our simulation for 300 minutes.

Our simulation results of the translation inhibition experiment are presented in Figures 5.18 and 5.19. Figure 5.18a shows a plot of the total concentrations of hes1 mRNA and Hes1 protein in the nucleus over time, while Figure 5.18b shows the corresponding total concentrations in the cytoplasm. Finally, Figure 5.19 shows the spatio-temporal evolution of the mRNA and protein concentrations respectively over the same time period. As can be seen from all these plots, no oscillations in the concentration levels are observed, in line with the experimental results of (Hirata et al., 2002). Furthermore, unlike in the proteasome inhibition experiment, notice that there is good agreement between the Hes1 reaction-diffusion model and the extended He1 model (compare

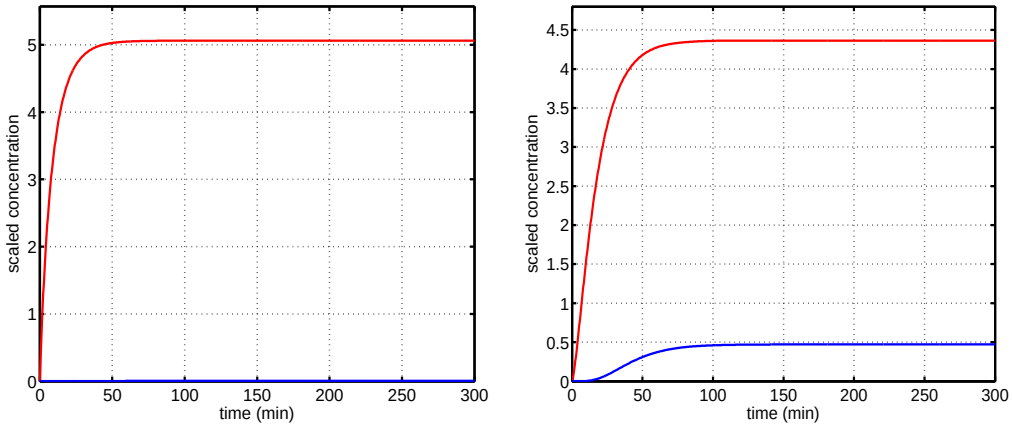

(a) *nuclear compartment* **(b)** *cytoplasmic compartment*

Figure 5.18: *Plots of the total concentrations (in non-dimensional units) of hes1 mRNA (red) and Hes1 protein (blue) in (a) the nucleus and (b) the cytoplasm for the Hes1 reaction-diffusion model when translation is inhibited. No oscillations are observed. Parameter values as per column 2, Table 5.1 with α_p reduced by a factor* 100*.*

Figure 4.14 and Figure 5.19).

5.9 The influence of extrinsic noise: exploring model dependence on initial conditions

We now exam the sensitivity of the extended Hes1 model to changes in initial conditions. In order to vary the initial conditions, we adopt the same procedure that we used for the Hes1 reaction-diffusion model (see section 4.7). Once again, Figure 5.20a shows the total concentration of protein over the entire cell for 10 simulations with different initial conditions. After an initial transient period (which appears dependent on initial conditions), the total concentration level settles into an oscillatory behaviour (or limit cycle). The corresponding hes1 mRNA versus Hes1 protein phase plane is displayed in Figure 5.20b. The amplitude, period and phase are largely unaffected by the changes in initial conditions. Hence, although the presented study of random initial conditions is not comprehensive, from the simulations presented it appears that the

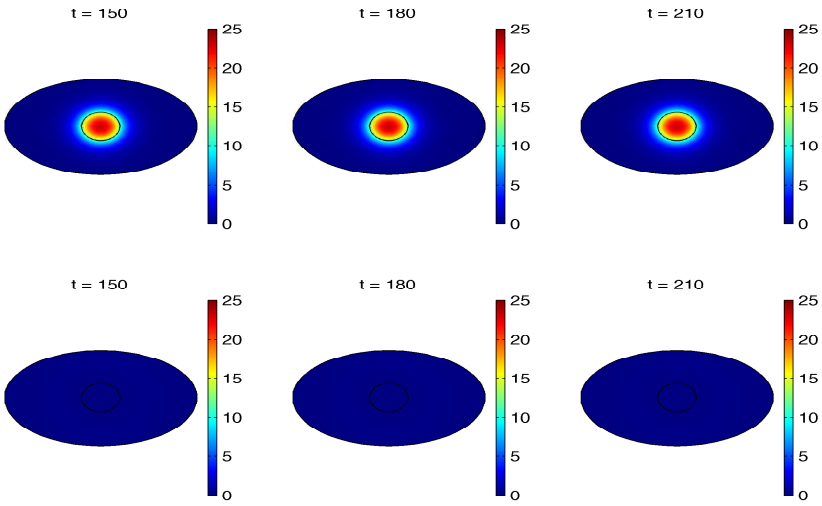

Figure 5.19: *Plots showing the spatio-temporal evolution of hes1 mRNA (first row) and Hes1 protein (second row) from times* $t = 150$ *to* 210 *minutes at* 30 *minute intervals for the Hes1 reaction-diffusion model when translation is inhibited. hes1 mRNA is found in high concentration in the nucleus. Hes1 protein concentration is so low it is not visible. Parameter values as per column 2, Table 5.1 with* α_p *reduced by a factor* 100*.*

model behaviour is robust to changes in initial conditions.

5.10 Discussion

In this chapter we have extended the Hes1 reaction-diffusion model presented in the previous chapter. The model was extended by including a nuclear membrane and active transport. We accounted for the permeability of the nuclear membrane by considering its thickness and the fact that diffusion across it is slower than in the nucleus or cytoplasm, and we assumed that proteins were convected from the cytoplasm to the nucleus in order to model translocation along microtubules.

Experiments have shown that stimulation of the Hes1 GRN can cause hes1 mRNA and Hes1 protein levels to oscillate for up to 720 minutes. These oscillations are understood to be driven by a negative feedback loop. Therefore (as in the previous chapter) we explored numerically our extended model in the context of sustained oscillatory

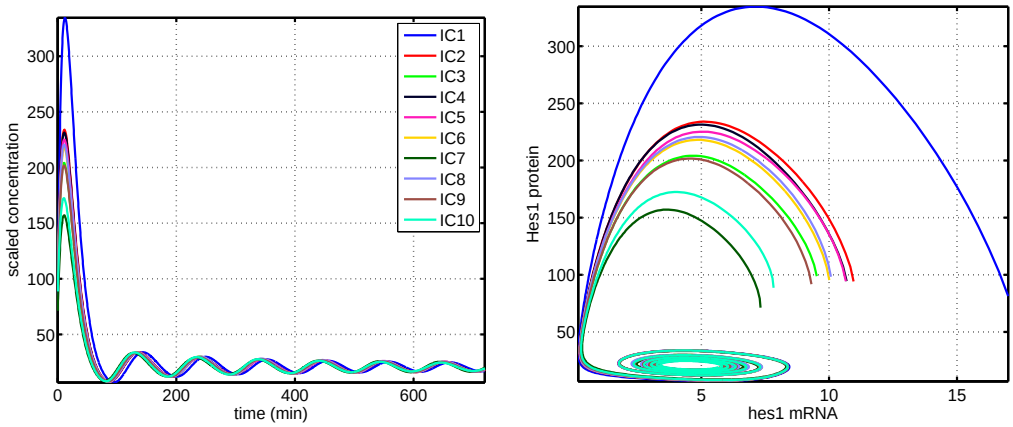

(a) *10 simulations with different ICs* **(b)** *corresponding phase plane*

Figure 5.20: *Plots of the total concentrations Hes1 protein (blue) integrated over the entire cell for the extended Hes1 model with different initial conditions. After an initial transient period induced by the initial conditions, the model appears robust to changes in initial conditions. Parameter values as per column 2, Table 5.1.*

dynamics. We found ranges of values for the model parameters such that sustained oscillatory dynamics occurred, noting that these parameters were consistent with available experimental measurements. We also found that our model extensions acted to broaden the parameter ranges that yielded oscillations compared with the simple Hes1 reaction-diffusion model (see chapter 4). Hence oscillatory behaviour is made more robust by the inclusion of both the nuclear membrane and active transport.

Given that cell shape can influence intracellular signalling (Meyers et al., 2006; Neves et al., 2008), we investigated the effect on the dynamics of various cell geometries, finding for our extended Hes1 model that oscillatory dynamics are strongly robust to changes in the size and shape of the cell and its nucleus. Such results are consistent with other recent spatio-temporal modelling studies of intracellular signalling pathways (Terry et al., 2011; Terry and Chaplain, 2011). In the interest of making accurate quantitative statements, we explored more realistic domains, hence we imported our domain from an image of an osteosarcoma cell — the Hes1 GRN is known to play a critical role in the development of osteosarcomas (Zhang et al., 2008). We were able to

make quantitative observations regarding, for example, the proportion of Hes1 that enters the nucleus. Our quantitative data serve as predictions until accurate experimental data become available.

We demonstrated that our extended model is robust to localising mRNA production to a small (gene like) region of the nucleus if the transcription rate parameter is scaled appropriately. It is unlikely that the diffusion coefficient for molecules in the nucleus would be the same for molecules in the cytoplasm and it is also unlikely that the diffusion coefficient for different molecular specifies would be the same. To this end, we showed that our model still yields oscillatory dynamics using a number of differential diffusion coefficient combinations. We also explored the scenario of protein transport by pure convection in the cytoplasm (i.e., no diffusion) and found that our model could also yield oscillatory dynamics under this extreme condition. This implies that the precise transport mechanism is not important, what is important is that the protein reaches the nucleus sufficiently fast. Furthermore, we showed that our model is robust to changes in initial conditions.

Motivated by experiments involving microtubule-disrupting chemotherapeutic drugs (Jordan and Wilson, 2004; Kavallaris, 2010; Carbonaro et al., 2011), we considered the special case in our extended model where active transport rates were set to zero. We found that this narrowed the ranges of values for model parameters such that sustained oscillatory dynamics occurred. We also considered the effect of proteasome inhibitor drugs and translation inhibition drugs. The model was able to reproduce known experimental data qualitatively (Hirata et al., 2002). Although the translation inhibition experiment yielded similar results for both the reaction-diffusion model and extended model of the Hes1 GRN, the proteasome inhibition experiment yielded some interesting differences. In particular, the extended model showed Hes1 protein levels only in the nucleus after the proteasome inhibition numerical experiment. In contrast, the original reaction-diffusion model showed Hes1 protein levels spread uniformly throughout

the entire cell. Given the lack of direct experimental data for active transport along microtubules of Hes1, this numerical experiment proposes a method for checking the existence of active transport of Hes1. By simply treating the cell with proteasome inhibitors, the subsequent spatial distribution of Hes1 protein could indicate whether or not Hes1 is actively transported into the nucleus.

Chapter 6

A spatial stochastic model of the Hes1 gene regulatory network

6.1 Introduction

It is clear from the previous two chapters that mathematical models of the Hes1 GRN can benefit from the inclusion of cell structure and accounting for movement of intracellular molecules. While these models were able to reproduce the qualitative behaviour of the Hes1 GRN, i.e., oscillatory dynamics, they were not able to account for variability in period and amplitude that is found in the corresponding experimental data.

In biological systems there are numerous sources of stochasticity and heterogeneity, and these can have important consequences for understanding the overall system behaviour. Intrinsic noise is commonly found in many intracellular signalling pathways (Shahrezaei and Swain, 2008; Barik et al., 2008, 2010). This noise can arise due

to low abundance of molecular species, randomness in certain key processes (e.g. binding and unbinding of transcription factors to promoter sites), stochasticity in production processes (transcription, translation) and degradation events (Wilkinson, 2009). Clearly, mathematical models of GRNs with low copy numbers will be more faithful the more they seek to account for stochastic and spatial features of these networks.

Very few spatial stochastic models exist in the literature but this is beginning to change. Some of the first models of this kind were of the Min System in an *Escherichia coli* cell (Howard and Rutenberg, 2003; Fange and Elf, 2006). Howard & Rutenberg used a stochastic analogue of a 1D system of reaction-diffusion equations and found that, for some parameter values, the protein concentrations were low enough that fluctuations were essential for the generation of patterns. In the model of Fange & Elf trajectories were generated using the next subvolume method (NSM), and numerical simulations were able to reproduce all documented Min phenotypes, where deterministic or non-spatial models could not. A spatial stochastic model of the MAPK pathway was developed in Takahashi et al. (2010). This model was implemented numerically using a Green's function reaction dynamics scheme, which allows for individual particle level simulation of molecular species. Using this technique, MAPK responses that could not be observed using a mean-field approach were produced. Another recent spatial stochastic model was developed to study in detail a generic transcription factor binding and unbinding to DNA (van Zon et al., 2006). Here, the spatial stochastic model was able to support the use of well-stirred, zero-dimensional models for describing noise in gene expression. It is clear from these few examples that spatial stochastic modelling can provide insight into intracellular signalling pathways that other approaches can not. For a comprehensive review of spatial stochastic modelling of intracellular processes, see Burrage et al. (2011).

The development of mathematical models which reflect both spatio-temporal and stochastic aspects of GRNs can be regarded as an important computational tool in making

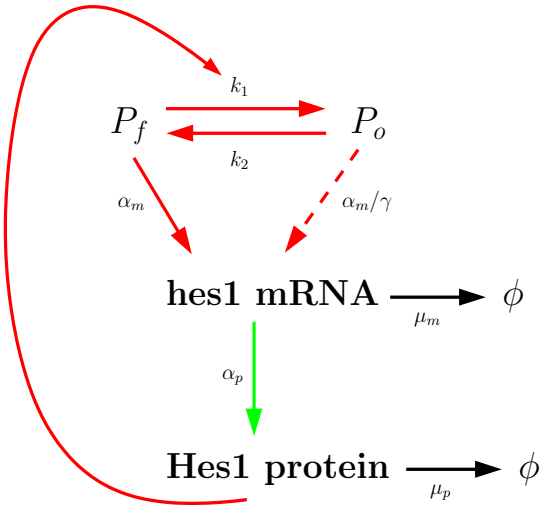

Figure 6.1: *The negative feedback loop in the Hes1 GRN (with explicit promoter states). When the promoter site is free, hes1 mRNA is transcribed at its maximal rate. hes1 mRNA then produces Hes1 protein via the process of translation. Hes1 protein occupies the promoter and represses the transcription of its own mRNA. The occupied promoter site is still able to produce hes1 mRNA, but at a significantly reduced rate (Takebayashi et al., 1994). Reaction arrows displayed in red only occur at the promoter site, while those in green occur only in the cytoplasm and those in black occur everywhere within the cell.*

predictions about the behaviours of GRNs and in the optimising of targeted drug treatment. In this chapter we propose a novel spatial stochastic model of the Hes1 GRN. We focus our study on Hes1 oscillations observed in embryonic stem (ES) cells, as the quality and abundance of Hes1 expression data for this cell line far exceeds all others.

6.2 Spatial stochastic model formulation

We present here the formulation of the stochastic reaction-diffusion model, detailing the reactions and how diffusion events are handled.

The basic assumptions concerning the molecular reactions in the Hes1 feedback loop follow previous modelling efforts (Monk, 2003) and the previous two chapters. Figure 6.1 shows a revised schematic description of the network. Our model explicitly

considers the spatial distributions of the species so reactions are now localised to separate compartments of the cell, as indicated by the colours of the arrows. A key feature of all previous models of the Hes1 GRN is that they rely on a phenomenological Hill function term, which approximates the reduction in hes1 mRNA production caused by Hes1 protein occupying its promoter site. The model presented in this chapter now assumes that the promoter site exists in two states — a free state or one occupied by Hes1 protein, represented by P_f and P_o respectively. This is a first approximation, because — as we mentioned previously — there are actually multiple promoter sites that Hes1 dimers can bind to, see (Zeiser et al., 2007). Hence, all reactions are modelled by elementary mass action kinetics. Since our model is explicitly spatial and discrete, we can model the switching of gene states easily, so a Hill function approach is neither necessary nor appropriate.

6.2.1 The reaction-diffusion master equation

To account for intrinsic stochasticity we model the reaction-diffusion kinetics as a continuous-time, discrete-space Markov process. The state of the system is the discrete number of molecules of each of the species as a function of time. The likelihood of a transition is described by its reaction propensity, which defines the probability of transition from the state x to $x + N_r$ per unit time:

$$x \xrightarrow{\omega_r(x)} x + N_r, \tag{6.1}$$

where $N_r \in \mathbb{Z}^S$ is the transition step and is defined as the rth column in the stoichiometric matrix N and $\omega_r(x)$ is the reaction propensity function. When the system can be considered well mixed, the stochastic simulation algorithm (SSA) (Gillespie, 1976) or variants of it are typically used to generate statistically exact realisations of the process.

To introduce molecular motion due to diffusion, the spatial domain is subdivided into non-overlapping voxels in a mesh, cf. Figure 6.2. Diffusion is modelled as first order events where a species S_l in voxel ψ_i moves to an adjacent voxel ψ_j, i.e.,

$$S_{li} \xrightarrow{q_{lij} x_{li}} S_{lj}, \tag{6.2}$$

where x_{li} is the number of molecules of species l in voxel i, and q_{lij} is a diffusion rate constant that depends on D_l, the diffusion coefficient of species l, and on the size and shapes of voxels ψ_i and ψ_j. The equation that governs the time evolution of the probability density of the system is called the reaction-diffusion master equation (RDME). We assume that both hes1 mRNA and Hes1 protein can diffuse as described above, with diffusion coefficient $D = 6.00 \times 10^{-13} \mathrm{m}^2 \mathrm{min}^{-1}$ (Matsuda et al., 2008). We do not allow promoter species to diffuse, rather we assume the promoter species remain in the gene subdomain.

For fine discretisations, the classical SSA becomes inefficient. The NSM (Elf and Ehrenberg, 2004) is an algorithm adapted for simulations of the RDME, and it inherits good scaling properties from the Next Reaction Method (NRM) (Gibson and Bruck, 2000). For all following simulations, we have used NSM as implemented in the URDME (Unstructured Reaction-Diffusion Master Equation) software framework (Drawert et al., 2012). URDME uses unstructured tetrahedral and triangular meshes such as shown in Figure 6.2, thus enabling simulations to be performed on complex geometries. The diffusion rate constants q_{lij} are automatically computed for the unstructured mesh as described in more detail in earlier studies, see Engblom et al. (2009) and Drawert et al. (2012).

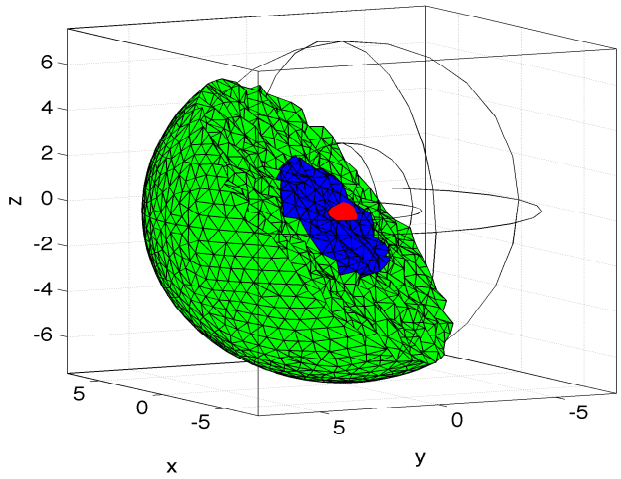

Figure 6.2: *The 3D meshed domain used in numerical simulations of the spatial stochastic Hes1 model. The domain is discretised such that 10,946 voxels make up the domain. Axes units here are in μm. The cell is represented by a sphere, centre (0,0), with radius 7.5μm. The nucleus is shown here as a blue sphere, centre (0,0), radius 3μm. The cytoplasm (shown in green) is the part of the cell that is outside the nucleus. The gene subdomain is chosen to be the voxel closest to the centre of the cell (0,0), a distance r from the nuclear membrane (shown in red).*

6.2.2 Domain, initial and boundary conditions

The computational domain is shown in Figure 6.2. The cell is represented by two concentric spheres with centre (0,0) and radius 7.5μm and 3μm respectively. The inner sphere models the nucleus. These values are chosen to be consistent with experimental measurements of ES cells (Zhou et al., 2001). The promoter site, or gene subdomain, is taken to be a single voxel at a radial distance r from the nuclear membrane. Unless otherwise stated we choose the promoter site to be at $r = 3\mu$m, i.e., the voxel closest to the centre of the cell (0,0). We arbitrarily choose initial conditions such that 60 Hes1 proteins are uniformly distributed in the cytoplasmic subdomain, 10 mRNA molecules in the nuclear subdomain and a single free promoter is found in the gene subdomain (our model does not appear to be sensitive to initial conditions — see section 6.6). Zero-flux boundary conditions are applied at the cell membrane and continuity of flux boundary conditions are applied at the nuclear membrane as a means of modelling the

Reaction	Description	Localisation	Parameter values
$P_f + protein \underset{k_2}{\overset{k_1}{\rightleftharpoons}} P_o$	Binding/unbinding of Hes1 protein to promoter	Promoter site	$k_1 = 1.00 \times 10^9 \text{M}^{-1}\text{min}^{-1}$, $k_2 = 0.1\text{min}^{-1}$
$P_f \xrightarrow{\alpha_m} mRNA$	Basal transcription of hes1 mRNA	Promoter site	$\alpha_m = 3.00\text{min}^{-1}$
$P_o \xrightarrow{\alpha_m/\gamma} mRNA$	Repressed transcription of hes1 mRNA	Promoter site	$\alpha_m = 3.00\text{min}^{-1}, \gamma = 30.00$
$mRNA \xrightarrow{\alpha_p} mRNA + protein$	Translation of Hes1 protein	Cytoplasm	$\alpha_p = 1.00\text{min}^{-1}$
$mRNA \xrightarrow{\mu_m} \phi$	Degradation of hes1 mRNA	Entire cell	$\mu_m = 0.015\text{min}^{-1}$
$protein \xrightarrow{\mu_p} \phi$	Degradation of Hes1 protein	Entire cell	$\mu_p = 0.043\text{min}^{-1}$
$S_{li} \xrightarrow{q_{lij}x_{li}} S_{lj}$	Molecular diffusion	Entire cell	$D = 6.00 \times 10^{-13}\text{m}^2\text{min}^{-1}$
	Radial distance of gene from nuclear membrane	Nucleus	$r = 3\mu\text{m}$

Table 6.1: *Description of reactions in the stochastic spatial Hes1 model, their localisation, and initial parameter values used.*

transport in and out of the nucleus. A summary of the reactions, their sub-cellular localisation, and the initial parameters used in the simulations are found in Table 6.1.

6.3 Numerical simulation results

6.3.1 The model reproduces quantitative and qualitative behaviour of wild-type ES cells

We performed simulations of the Hes1 GRN model using the parameter values in Table 6.1 and in order to be consistent with biological experiments, we ran our simulations for 1200 minutes (Kobayashi et al., 2009). Five representative trajectories are displayed in Figure 6.3 (first row), along with corresponding periods (second row). The instantaneous period presented in the second row is estimated using a Morlet continuous time wavelet transform (CWT) as implemented in a MATLAB toolbox called WAVOS, see Harang et al. (2012) for details. Given the highly oscillatory and noisy nature of our trajectories, the use of standard Fourier techniques can lead to inaccurate estimates of the period, as Fourier analysis assumes stationarity of the signal and its basis functions are unbounded in time (Mallat, 1999). Wavelets, in contrast, are localised in both time and frequency. This localises the analysis, allowing the changes in

signal properties to be tracked over time (Torrence and Compo, 1998). Furthermore, we make use of gaussian edge elimination to minimise artefacts in the approximation of the period.

The evolution of the total number of proteins is in close agreement with recent experimental studies, in terms of qualitative behaviour and quantitative values for the period. Although there have been many experiments performed to analyse the oscillatory nature of the Hes1 protein, it is not clear what units are used to measure protein expression levels, hence it is difficult to compare the numbers of Hes1 protein predicted from our model with real experimental values. However, we have received estimates of the copy number of hes1 mRNA in ES cells from experimentalists (see Table S3 of the electronic supplementary material of Sturrock et al. (2013), which fall in the range 0 to 465, and our mRNA values also fall in this range as shown in Figure 6.4(a). Notice that although there are large amplitude oscillations or variations in the protein copy number levels, the hes1 mRNA copy numbers are relatively stable. This phenomenon of small variations in mRNA copy number leading to large variations in protein copy number is consistent with other studies, for example, see Hasty et al. (2000). It is reasonable to assume that protein levels will be higher than mRNA levels (see Kar et al. (2009) and Fusco et al. (2003)), hence the values predicted by our model (see Figure 6.3) may be consistent with experimental values. In 6.4(a) we illustrate how the signal is amplified from a single promoter site switching from a free or occupied state to a large drop or increase in protein copy number. Consistent with intuition, as the protein levels increase the likelihood of the promoter site becoming occupied also increases and so it is not surprising that peaks in protein levels are followed by occupation of the promoter site. Unlike the copy number of Hes1 protein, values for its period can be found in the literature. Experimentalists estimated that the period for Hes1 protein in ES cells lies in the range of 180 to 300 minutes. The periods from 100 different trajectories of our model are displayed in Figure 6.5, and many of these lie in

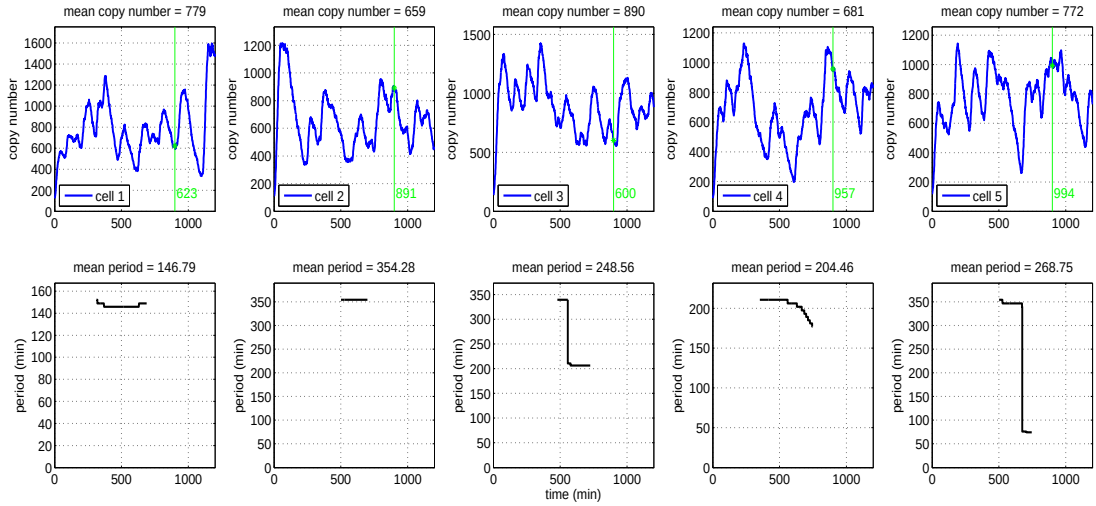

Figure 6.3: *In the first row, plots of the total numbers of Hes1 protein (found by summing the number of proteins over the entire cell domain) are presented against time for 5 different trajectories of the Hes1 model. The mean copy numbers are displayed in the titles of row 1. The green vertical line represents the transference of cells to a neural differentiation medium. The number highlighted in green is the copy number of Hes1 at this time. The second row shows the corresponding time varying period as approximated by a Morlet continuous time wavelet transform with gaussian edge elimination. The mean periods are displayed in the titles of row 2. Baseline parameter values are used, see column 4, Table 6.1.*

the same range reported by biologists (compare Figure 6.5 with supplemental Figure S1 of Kobayashi et al. (2009)). Since our model accounts for intrinsic noise, it is able to reproduce the highly variable period and amplitude found in the expression of Hes1 protein in ES cells. This is a feature that the reaction-diffusion model and extended model were not able to reproduce.

Furthermore, we include a plot of spatial snapshots of the spatio-temporal evolution of Hes1 protein in Figure 6.6. Such spatial plots can be compared with experimental movie clips of bioluminescence imaging of Hes1 protein in ES cells (see supplemental movie file of Kobayashi et al. (2009) for example).

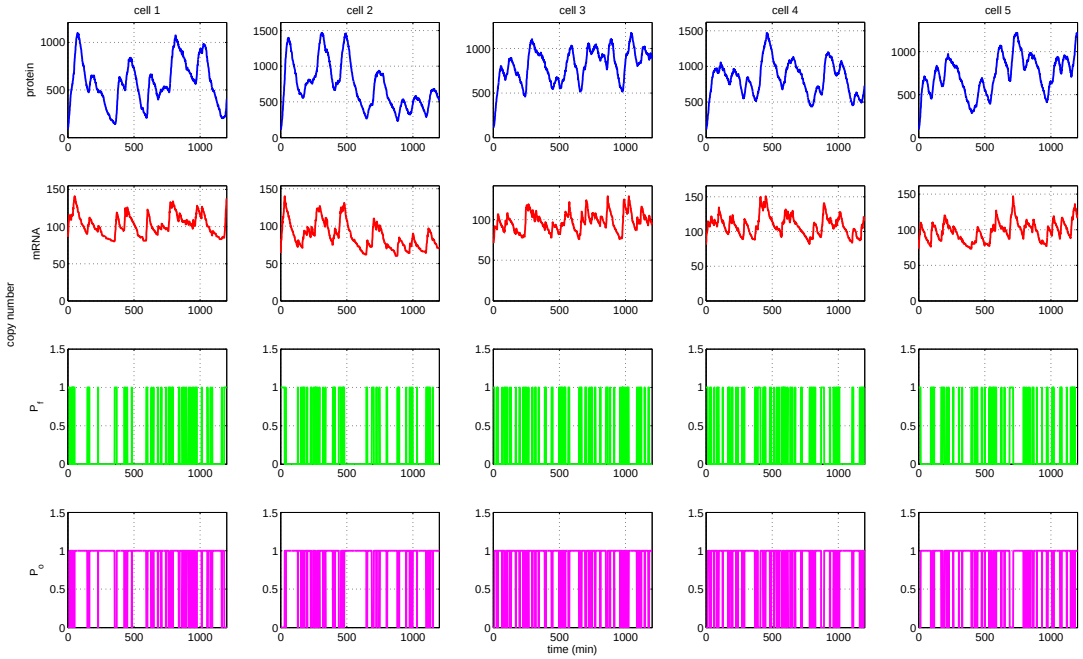

(a)

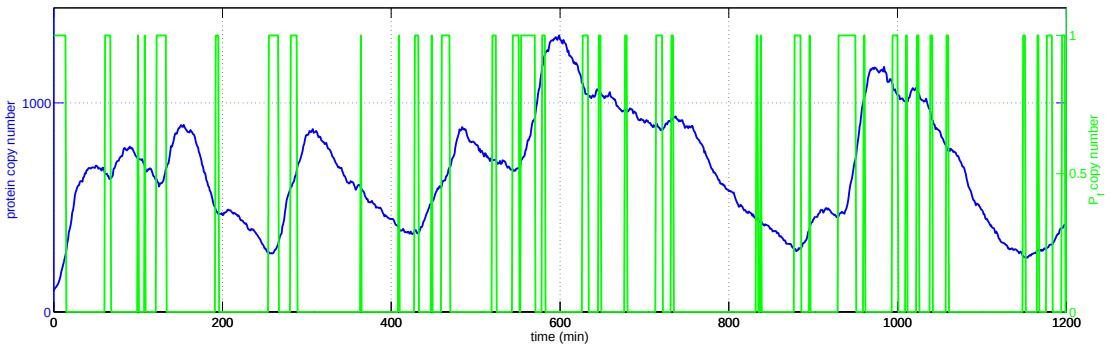

(b)

Figure 6.4: *(a) Plots showing the total copy number of all species over time for 5 different trajectories of the Hes1 model (see Table 6.1 for parameter values). It can be seen from these plots that the time in which the promoter site is occupied (free) corresponds to troughs (peaks) in the copy number of hes1 mRNA and consequently troughs (peaks) in the copy number of Hes1 protein. (b) Plots showing the total copy number of Hes1 protein and the corresponding value of the free promoter, P_f, over time. It can be seen from this plot that if the promoter is free for a long enough period of time, then this produces a peak in Hes1 expression. This is particularly evident at approximately* 600 *minutes.*

6.3.2 Intrinsic noise can explain variability in ES cell differentiation

Our model produces some trajectories that either have a period that is unrealistically long ($>$ 400 minutes) or simply do not oscillate with non-negligible amplitude. We shall label these trajectories as cells exhibiting 'persistent expression' (PE) of Hes1. For example, in Figure 6.5 we can observe 15 trajectories falling into this category. In ES cells, as stated earlier, persistent high levels of Hes1 was indicative of cells that would differentiate into mesodermal cells. Hence, our model can yield predictions concerning the differentiation response of ES cells. In particular, given a batch of ES cells, it is possible to predict how many would differentiate into neural and mesodermal cells at a specific time. We have illustrated this idea in the top row of Figure 6.3. The green vertical line indicates the time at which cells are transferred to a neural differentiation medium (900 minutes) with the copy number of Hes1 at this time given beside the line. Cells with high expression of Hes1 protein at this time would differentiate into mesodermal cells while those displaying low expression levels would differentiate into neurons. If we define high and low expression as the copy number being greater than or less than the mean respectively, then we suggest that of the trajectories displayed in Figure 6.3, cells 2, 4 and 5 would differentiate into mesodermal cells and cells 1 and 3 would differentiate into neurons. Hence, by accounting for intrinsic noise, our simple model is able to reproduce the variability encountered experimentally in ES cell differentiation.

6.4 Parameter sweeps

Here we explore the parameter space of our model in a bid to find the main sources of stochasticity and variability exhibited in its trajectories. We achieve this mainly

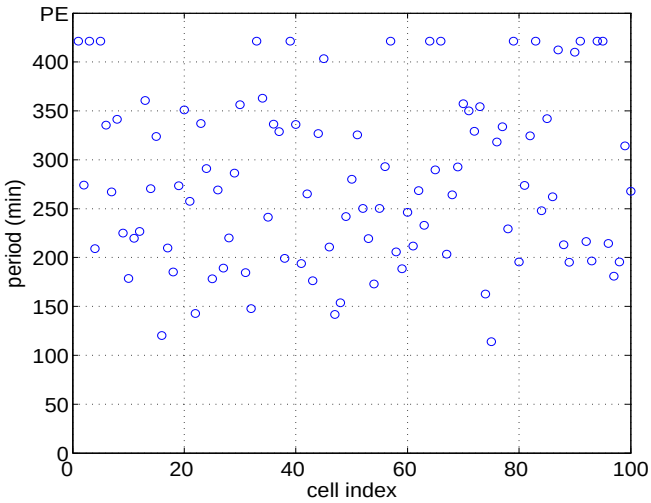

Figure 6.5: *Plot showing the period of 100 different trajectories. The periods were calculated using a Morlet continuous wavelet transform with gaussian edge elimination. Baseline parameter values are used, see column 4, Table 6.1.*

through parameter sweeps. A parameter sweep is performed by holding all parameter values at their baseline values (see column 4, Table 6.1), then varying a single parameter over some finite range and recording one hundred trajectories for each new parameter set produced. For each trajectory recorded, we compute its mean period (as in Figure 6.5) and visualise the output in a histogram. We perform parameter sweeps for all parameters in the model and those figures that are not explicitly discussed here are deferred to section 11.2.3 of the Appendix. We discuss here the two parameters for which we do not have experimental measurements, namely, k_1 and k_2 as well as two spatial parameters, D and r. Note that by only varying one parameter at a time, we are neglecting most of the parameter space. A future study will investigate the full parameter space of our model using data clustering techniques.

In general we found from the parameter sweeps that the model produces broad distributions of periods whenever oscillatory dynamics are found. Provided the sweep does not yield trajectories entirely exhibiting persistent expression of Hes1 then we find great variety in the mean periods computed.

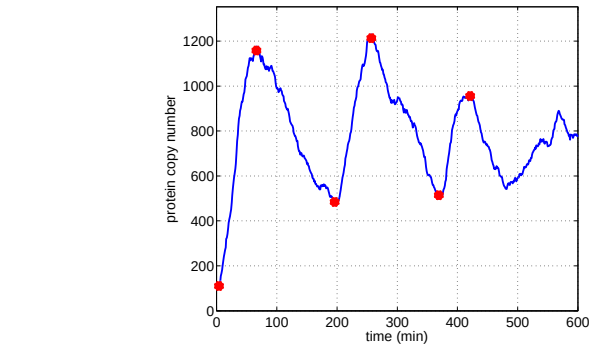

(a)

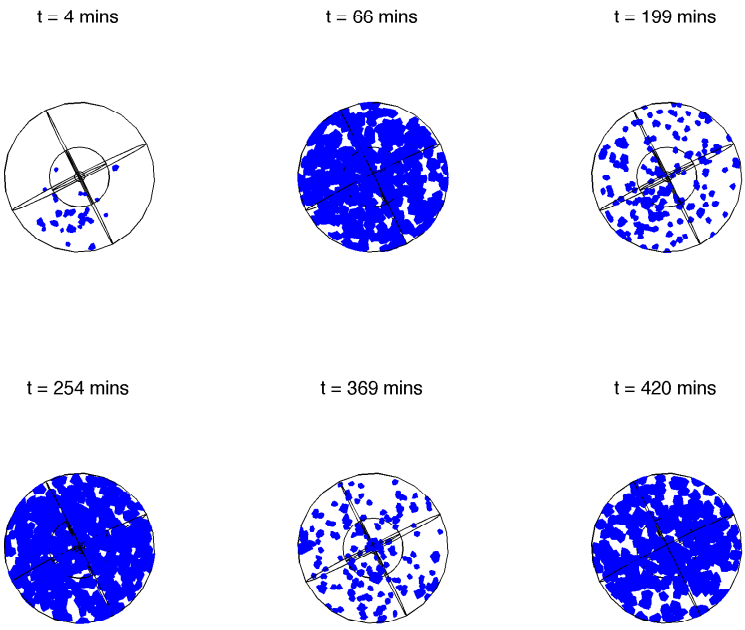

(b)

Figure 6.6: *(a) Plot showing the total Hes1 protein copy number over a period of* 600 *minutes from a single trajectory of the Hes1 model, and (b) Plots showing the corresponding spatial distributions of Hes1 protein. Baseline parameter values are used, see column 4, Table 6.1. The times for these spatial snapshots were chosen to correspond to the peaks and troughs of oscillations in Hes1 protein copy number shown in (a) above. These times are highlighted by the red asterisks in (a). In (b) blue voxels indicate regions of the cell which contain Hes1 protein.*

6.4.1 Hes1 must bind to the promoter sufficiently fast for oscillations to be observed

The rate at which Hes1 protein binds to the promoter region of the hes1 gene is an important parameter in our model. It is responsible for the negative feedback Hes1 protein exhibits on its own mRNA production. We vary k_1 over the range $(1.00 \times 10^7 - 1.00 \times 10^{10})\,\mathrm{M}^{-1}\mathrm{min}^{-1}$, which is in line with experimental measurements of protein-DNA binding rates (Tafvizi et al., 2011). The histogram displaying the mean periods from the parameter sweep of k_1 is displayed in Figure 6.7. The results are consistent with intuition — if k_1 is too small, Hes1 protein is unlikely to bind to the promoter site and so the majority of trajectories display PE. Experimentalists have compared the expression levels of wild-type Hes1 and a functionally defective Hes1 mutant, which is unable to bind to the N or E box DNA sequence, in hematopoietic progenitor cells. The authors reported no repression of Hes1 when the mutant levels were monitored, in contrast to the wild-type case (Yu et al., 2006). This is comparable to low values of k_1 in our model, which produce trajectories which mainly exhibit persistent expression (i.e., no repression of Hes1 levels). Hence, using our model we can investigate both mutant and wild-type Hes1 genes. If we set $k_1 = 0$ then all trajectories are found to display PE, with high values of protein. As k_1 is increased, we obtain a broad range of periods, which appear to be quite robust to change provided k_1 is above approximately $2.50 \times 10^8\,\mathrm{M}^{-1}\mathrm{min}^{-1}$.

The parameter value for which we have the least information in our model is k_2, the rate at which protein unbinds from the promoter site, making the promoter free again. We vary k_2 in the interval $0.1 - 1 min^{-1}$ and the histogram containing this parameter sweep is displayed in Figure 6.8. For lower values of k_2 ($0.01\mathrm{min}^{-1}$ to $0.34\mathrm{min}^{-1}$) we can observe a broad range of periods, but as k_2 is increased, we find more and more trajectories displaying PE of Hes1. This can be interpreted biologically as the promoter

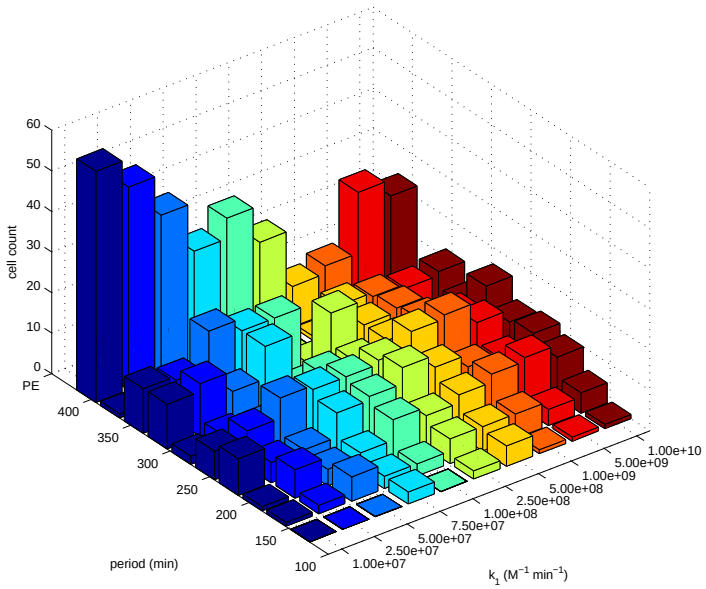

Figure 6.7: *Histogram plot showing the effect on the period of oscillations of changing the parameter k_1, the rate of Hes1 protein binding to the promoter site.* 10 *values of k_1 from the range* $1.00 \times 10^7\,\mathrm{M}^{-1}\mathrm{min}^{-1}$ *to* $1.00 \times 10^{10}\,\mathrm{M}^{-1}\mathrm{min}^{-1}$ *were chosen, and* 100 *trajectories for each different value were recorded. All other parameters in the model (see column 4, Table 6.1) were held constant. The mean periods were computed and divided into 'bins' varying from* 100 *mins to persistent expression (PE), i.e., greater than* 400 *mins. For lower values of k_1, most of the computed mean periods fall into the PE bin. As k_1 is increased, less and less mean periods are found in the PE bin. Provided k_1 is greater than approximately* $2.50 \times 10^8\,\mathrm{M}^{-1}\mathrm{min}^{-1}$*, it appears to be relatively robust to change, with broad ranges of periods found.*

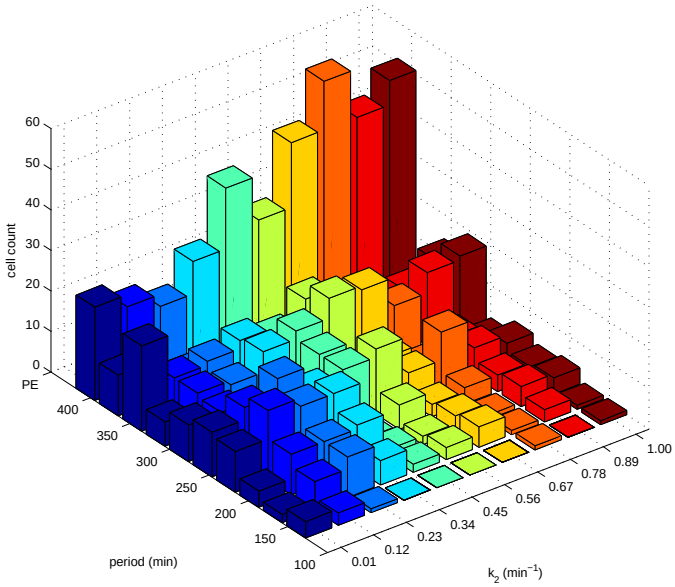

Figure 6.8: *Histogram plot showing the effect on the period of oscillations of changing the parameter k_2, the rate of Hes1 protein unbinding from the promoter site.* 10 *values of* k_2 *from the range* $(0-1)\text{min}^{-1}$ *were chosen, and* 100 *trajectories for each different value were recorded. All other parameters in the model (see column 4, Table 6.1) were held constant. The mean periods were computed and divided into 'bins' varying from 100 mins to persistent expression (PE), i.e., greater than* 400 *mins. Consistent with intuition and in contrast to the case of* k_1*, for larger values of* k_2*, most of the computed mean periods fall into the PE bin. As* k_2 *is decreased, less and less mean periods are found in the PE bin. Provided* k_2 *is less than approximately* 0.56min^{-1}*, it appears to be robust to change, with broad ranges of periods recorded.*

site becoming free too quickly, which would prevent the negative feedback from taking effect. As in the case of parameter k_1, if we set $k_2 = 0$ we find no oscillations in the trajectories of our model. However, in contrast to k_1, we find low protein levels.

6.4.2 Oscillatory dynamics are only found for sufficiently large diffusion coefficients

We found in chapters 4 and 5 that PDE models of Hes1 oscillations exhibited oscillatory dynamics for a finite range of values of the diffusion coefficient, i.e., if the diffusion coefficient was too large or too small then oscillations ceased. We investigate

a range of values for the diffusion coefficient in our model, in order to see if the same properties are retained in our stochastic model (see Figure 6.9 for the corresponding parameter sweep). Interestingly, in the context of observing oscillatory dynamics, it appears that D is bounded below, but not above. No matter how large the diffusion coefficient is made, the model still yields oscillations. This is likely to be a result of the stochastic nature of our model. Even if the diffusion coefficient is very large, it is still not a certainty that the protein will find the gene site almost instantly, which is the case in the corresponding continuum model. However, if the diffusion coefficient is too small, then mRNA and protein will stay in the subdomain where they originated, which is reflective of the continuum case. Overall, our spatial stochastic model is more robust to changes in the diffusion coefficient than a continuum model of the same GRN. In particular. oscillatory dynamics are observed for any diffusion coefficient greater than or equal to $D = 5.00 \times 10^{-14}\text{m}^2\text{min}^{-1}$.

6.4.3 Oscillatory behaviour is robust to changes in the position of the promoter site if the diffusion coefficient is large enough

It is known that some genes are located closer to the nuclear membrane than others, which increases their sensitivity to transcription factors (Cole and Lippincott-Schwartz, 1995). Evidence of precisely where the Hes1 gene is located within the nucleus is lacking, and in any case this is likely to change from cell to cell. Hence, given the symmetry of our domain, we investigate the influence of varying the distance r of the promoter site from the nuclear membrane for 3 different diffusion coefficients (see Figure 6.10 for the parameter sweeps). For a low value of the diffusion coefficient ($D = 1.00 \times 10^{-14}\text{m}^2\text{min}^{-1}$), we find that the location of the promoter site strongly influences the oscillatory behaviour observed. Persistent expression of Hes1 is observed when the promoter site is placed further away from the nuclear membrane, and as the

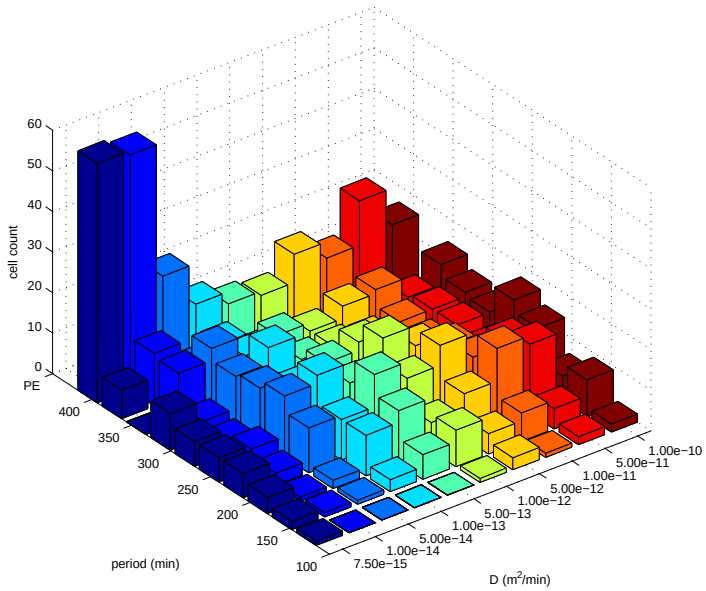

Figure 6.9: *Histogram plot showing the effect on the period of oscillations of changing the parameter D, the diffusion coefficient.* 10 *values of D from the range* $7.50 \times 10^{-15}\,\mathrm{m^2 min^{-1}}$ *to* $1.00 \times 10^{-10}\,\mathrm{m^2 min^{-1}}$ *were chosen, and 100 trajectories for each different value were recorded. All other parameters in the model (see column 4, Table 6.1) were held constant. The mean periods were computed and divided into 'bins' varying from 100 mins to persistent expression (PE), i.e., greater than* 400 *mins. For lower values of D, most of the computed mean periods fall into the PE bin. As D is increased, less mean periods are found in the PE bin. Provided D is greater than approximately* $5.00 \times 10^{-14}\,\mathrm{m^2 min^{-1}}$*, D appears to be robust to change, with broad ranges of periods recorded.*

promoter site is moved closer to the nuclear membrane, we find a broader distribution of periods. A slight dependence on promoter site location is observed for the default value of the diffusion coefficient, $D = 6.00 \times 10^{-13}\text{m}^2\text{min}^{-1}$. Here, if the promoter site is too close to the nuclear membrane, more trajectories exhibiting PE are found. Finally, for larger diffusion coefficients, specifically $D = 1.00 \times 10^{-11}\text{m}^2\text{min}^{-1}$, we find a broad range of oscillatory dynamics which are robust to promoter site location.

6.5 Controlling differentiation responses via drug treatment

We explore here the influence of inhibiting the proteasome in the context of our spatial stochastic model in a similar manner to the previous two chapters. The proteasome is a large proteolytic protein complex found in all eukaryotic cells that is the primary site for degradation of most intracellular proteins. The proteolytic activities of the proteasome can be inhibited by the class of drugs known as proteasome inhibitors. It is known that exposing fibroblast cells to proteasome inhibitors (specifically 100 μM of ALLN) results in increased levels of Hes1 protein and decreased levels of hes1 mRNA. In particular, it was shown that hes1 mRNA levels peak 1 hour after proteasome inhibition treatment (Hirata et al., 2002). We reproduce this experiment using our model by decreasing μ_p by a factor of 100 and running our simulation for 240 minutes (see Figure 6.11). The model is able to reproduce the experiment qualitatively, i.e., mRNA levels peak quickly then stabilise at a low number while protein levels saturate at high levels. We performed 100 simulations with μ_p decreased by a factor 100 and found that the average time for hes1 mRNA levels to peak was 29.36 minutes (shorter than that of fibroblast cells and similar to the peak times we found for the PDE models, see

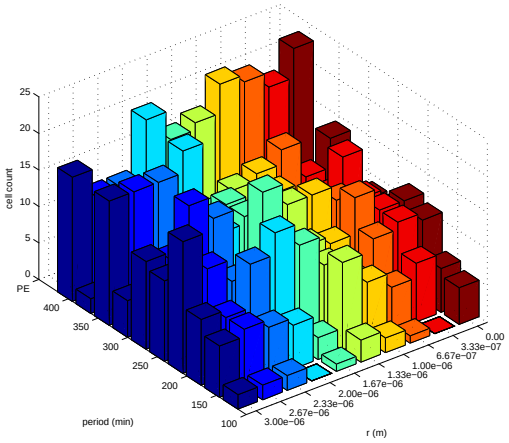

(a) $D = 1.00 \times 10^{-11}\text{m}^2\text{min}^{-1}$

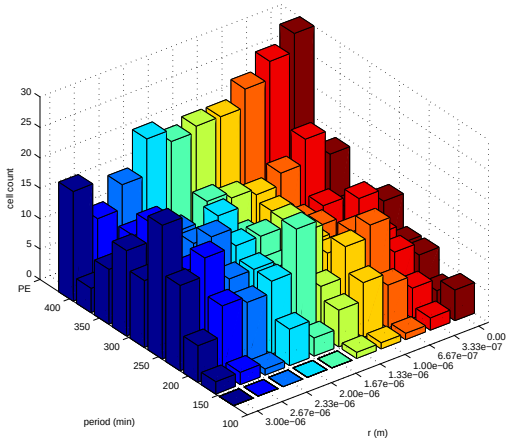

(b) $D = 6.00 \times 10^{-13}\text{m}^2\text{min}^{-1}$

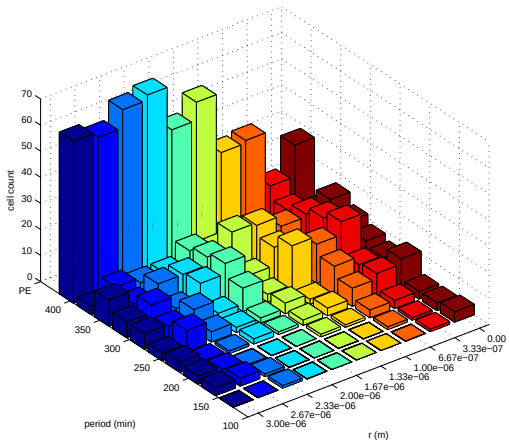

(c) $D = 1.00 \times 10^{-14}\text{m}^2\text{min}^{-1}$

Figure 6.10: *Histogram plots showing the effect on the period of oscillations of changing the parameter r, the distance of the promoter site from the nuclear membrane for 3 different values of D, the diffusion coefficient. The second histogram, (b), corresponds to the default value for D, so in this case we only varied r, all other parameters were held constant (see column 4, Table 6.1). In the case of (a), we chose a faster diffusion coefficient ($D = 1.00 \times 10^{-11}\,\text{m}^2\text{min}^{-1}$) and in (c) we chose a slower diffusion coefficient ($D = 1.00 \times 10^{-14}\,\text{m}^2\text{min}^{-1}$). For all* 3 *histograms displayed,* 10 *values of r from the range* $(0-3)\mu\text{m}$ *were chosen, and* 100 *trajectories for each different value were recorded. The mean periods were computed and divided into 'bins' varying from 150 mins to persistent expression (PE), i.e., greater than* 400 *mins. In (a) and (b) we see little variation in the mean periods recorded, suggesting r is robust to change and not a sensitive parameter. However, in (c), when the diffusion coefficient is slower, we find the position of the promoter site is important for determining the mean period distribution. We find that with a slower diffusion coefficient, it is possible to observe oscillatory dynamics if the promoter site is located closer to the nuclear membrane.*

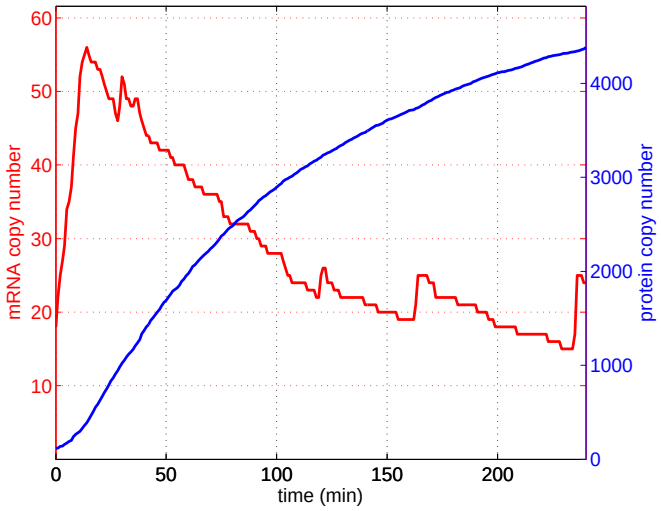

Figure 6.11: *A single trajectory from a proteasome inhibition numerical experiment. The total numbers of hes1 mRNA (red) and Hes1 protein (blue) are plotted against time. Baseline parameter values are used, with the exception of* μ_p *which is reduced by a factor* 100.

Figures 4.11 and 5.16). We are not aware of proteasome inhibition experiments performed in ES cells, and so leave this result as a quantitative prediction of the model. Using our model, we can also make the prediction that ES cells treated with proteasome inhibitors are more likely to differentiate into mesodermal cells.

Treating cells with cycloheximide inhibits the key process of translation in cells. Experiments have been performed in fibroblast cells to monitor levels of hes1 mRNA in response to this treatment. In the experiments a sustained increase of hes1 mRNA levels is reported (Hirata et al., 2002). We mimic this experiment with our spatial stochastic model by decreasing α_p by a factor of 100 and running our simulation for 300 minutes. The results of this numerical experiment are shown in Figure 6.12 (and can be compared with Figures 4.13 and 5.18). Our model is able to reproduce qualitative behaviour, i.e., an increase in hes1 mRNA numbers. In terms of exact numbers, we recorded the mean copy number of hes1 mRNA produced by our model under translation inhibition conditions and compared it with the wild-type case (recording 100 means for each case then taking the average of the means). The translation inhibition experiment caused mean mRNA levels to increase from 50 to 183 (more than threefold

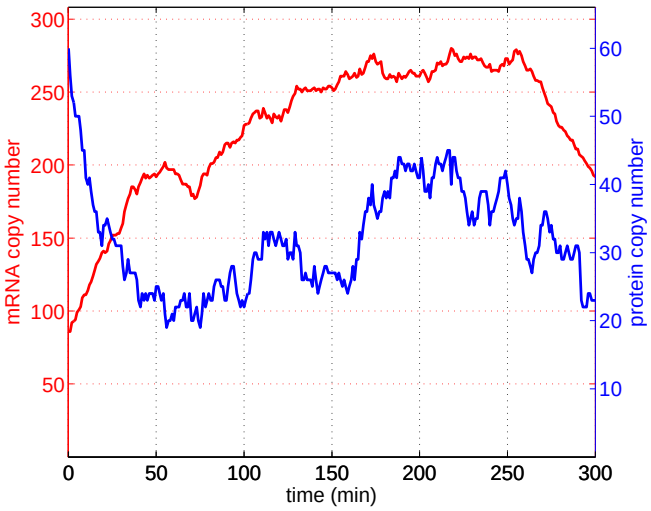

Figure 6.12: *A single trajectory from a translation inhibition numerical experiment. The total numbers of hes1 mRNA (red) and Hes1 protein (blue) are plotted against time. Baseline parameter values are used with the exception of* α_p *which is reduced by a factor* 100.

increase). We leave this result as a quantitative prediction of the model. Furthermore, we observe that protein levels are persistently low, so using our model we can make the prediction that ES cells undergoing translation inhibition would be more likely to differentiate into neuronal cells.

6.6 The influence of extrinsic noise: exploring model dependence on initial conditions

In this section we present the results of an initial condition sensitivity analysis. We choose ten different arbitrary initial conditions as stated in Table 6.2. In Figure 6.13 the mean periods of 100 realisations for each different initial condition is plotted in a histogram. There are only small differences in the mean period distributions. Hence, we conclude that our spatial stochastic model of the Hes1 GRN appears to be robust to changes in initial condition.

	P_f	P_o	*protein*	*mRNA*
$IC1$	0, -, -	1, -, -	0, 600, 0	0, 0, 0
$IC2$	1, -, -	0, -, -	0, 0, 0	0, 0, 60
$IC3$	0, -, -	1, -, -	0, 0, 0	0, 0, 0
$IC4$	1, -, -	0, -, -	0, 600, 0	0, 0, 60
$IC5$	0, -, -	1, -, -	0, 600, 600	0, 60, 60
$IC6$	0, -, -	1, -, -	0, 60, 0	1, 0, 0
$IC7$	1, -, -	0, -, -	0, 0, 0	0, 0, 120
$IC8$	0, -, -	1, -, -	1, 0, 0	1, 0, 0
$IC9$	1, -, -	0, -, -	10, 0, 0	0, 0, 120
$IC10$	0, -, -	1, -, -	0, 60, 60	0, 120, 120

Table 6.2: *Table showing the* 10 *different initial conditions used to test the model sensitivity/robustness to different initial conditions. The values are the initial number of free promoter, occupied promoter and the copy number of proteins and mRNA in the promoter, nucleus or cytoplasm respectively.*

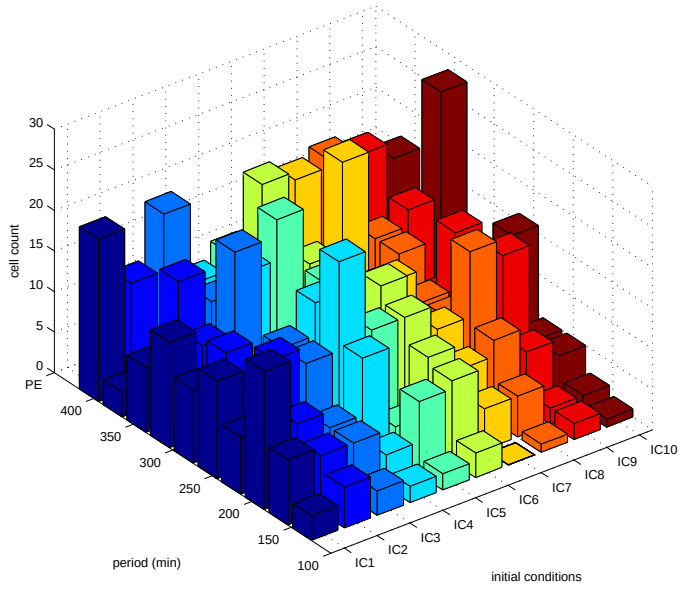

Figure 6.13: *Histogram plot showing the effect on the mean period of oscillation of using the* 10 *different initial conditions defined in column 4, Table 6.1. The initial conditions were chosen arbitrarily. The results of the plot show that the model is robust to changes in initial condition.*

6.7 Discussion

ES cells are pluripotent stem cells with the ability to differentiate into various cell types belonging to all three germ layers: ectoderm, mesoderm and endoderm. Application of these differentiated cells is highly anticipated for regenerative medicine, but ES cells respond heterogeneously to different cues, resulting in a mixture of various types of differentiated cells. The basic mechanism governing such heterogeneity in the differentiation of ES cells is not well understood but recent studies have suggested the cyclic expression of Hes1 plays a role.

In this chapter, we have presented a spatial stochastic model of the Hes1 GRN that yields results in close agreement with experimental studies. Transcriptional feedback systems in eukaryotic cells are inherently stochastic and spatial and the work presented here emphasises the need for mathematical models to account for this. With these modelling assumptions, we were able to propose intrinsic noise as the main driving force for the heterogeneity observed in ES cell differentiation responses.

In contrast to the PDE models of the Hes1 oscillator presented in the previous two chapters, our spatial stochastic model is able to reproduce the variability in period and amplitude of Hes1 oscillations observed in experiments. We were able to ask more questions of our model than recent stochastic DDE models (Barrio et al., 2006), as well as being able to directly compare our numerical simulations with bioluminescence movies of *in vivo* Hes1 expression. Additionally, our model does not rely on a Hill-function approximation to the negative feedback that Hes1 protein exerts on its own mRNA, the validity of which has been cast into doubt in recent years (Weiss, 2009).

Our model was able to produce the observed highly variable expression levels of Hes1 under a wide range of conditions. To this end, we presented extensive parameter sweeps in which we varied a single parameter at a time and presented (in histogram

format) the mean period distributions. We focussed on parameters for which we had the least information and also spatial parameters such as the location of the gene site within the nucleus. We were also able to demonstrate that our model is robust to changes in initial conditions.

Given the potential application for regenerative medicine, we have also proposed methods of controlling differentiation responses via drug treatment. Our model has predicted that applying proteasome inhibitors to an ES cell could yield a mesodermal cell while applying translation inhibitors could yield a neuronal cell. Our model was also able to reproduce experimental results in which hes1 transgenes were introduced to hematopoietic progenitor cell which encoded a mutant Hes1 protein lacking the DNA-binding domain (Yu et al., 2006).

The p53-Mdm2 gene regulatory network

Chapter 7

The p53-Mdm2 gene regulatory network

7.1 Introduction

We begin this chapter by reviewing the background biology of the p53-Mdm2 GRN. We go on to discuss some recent experimental data that has emerged in this area as well as reviewing mathematical modelling efforts. As in the case of the Hes1 GRN, we are able to demonstrate that using a strictly temporal approach can have limitations in modelling the p53-Mdm2 GRN.

7.2 Biological background

The pleiotropic p53 tumour suppressor protein is a well-established regulator of the cell cycle (Levine, 1997). In response to a variety of cellular stresses, such as DNA

damage, ribosome biogenesis defects, oncogene activation, hypoxia and chemotherapeutic drugs, p53 is activated and induces a range of responses including cell cycle arrest, senescence or apoptosis (programmed cell death) (Vousden and Prives, 2009; Vogelstein et al., 2000). The central role of p53 as a cell cycle regulator is highlighted in human cancers. Mutations that inactivate p53 function have been detected in more than 50% of human cancers (Bennet et al., 1999). Importantly, even tumours with wild type p53 have defects in upstream regulators or downstream effectors of p53. Therefore, inactivation of the p53 GRN is a common event in cancer development (Zilfou and Lowe, 2009; Toledo and Wahl, 2006).

In normal unstressed conditions, the levels and activity of p53 remain low, but in response to cellular stress, p53 levels are increased and the p53 pathway is activated. A vital negative regulator of p53 function in cells is the Mdm2 oncogene product. Mdm2 suppresses p53 function by at least two mechanisms. Firstly, Mdm2 interacts with the transactivation domain of p53 in the N-terminus inhibiting p53 transcriptional activity and secondly, Mdm2 acts as a ubiquitin E3-ligase, promoting p53 ubiquitination and proteasomal degradation. Mdm2 is also a target gene for p53. This creates a negative feedback loop which provides tight regulation of p53 function in cells (Coutts et al., 2009; Carter and Vousden, 2009). This negative feedback loop is depicted schematically in Figure 7.1.

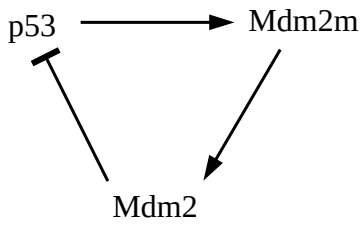

Figure 7.1: *Schematic diagram of the p53-Mdm2 gene regulatory network. p53 mRNA produces p53 protein, which then upregulates Mdm2 mRNA (stated as "Mdm2m" in the schematic) expression. Mdm2 then enhances degradation of p53 (through the process of ubiquitination).*

The importance of the p53-Mdm2 negative feedback loop was first demonstrated in

mouse animal model systems where deletion of Mdm2 caused embryonic lethality that was rescued by concomitant p53 deletion (Jones et al., 1995; de Oca Luna et al., 1995). Mdm2 is overexpressed in tumours with wild type p53 function, which could account for suppression of p53 function (Toledo and Wahl, 2006; Marine and Jochemsen, 2003). It has also been observed that Mdm2 protein levels dramatically decrease within the first 5 minutes after DNA damage, which allows for the accumulation of p53 (Stommel and Wahl, 2004). Therefore, a key activity of Mdm2 in cells is to suppress p53 function. Given the importance of p53 in controlling cell cycle and tumour development, it is not surprising that the p53-Mdm2 feedback loop is very tightly controlled in cells. The spatial localisation of p53 is also critical to maintaining cellular homeostasis. It is known that mislocalisation of p53, specifically cytoplasmic sequestration, is found in various tumour types, such as colorectal carcinoma, undifferentiated neuroblastoma and breast carcinoma (O'Brate and Giannakakou, 2003).

Experimental data have revealed that in response to gamma irradiation, p53 and Mdm2 concentrations exhibit oscillatory dynamics, both spatially and temporally (Geva-Zatorsky et al., 2006, 2010). It was found that isogenic cells in the same environment behaved in highly variable ways following DNA damaging gamma irradiation. In some cells more than 10 peaks in p53 and Mdm2 levels were observed, while in others low-frequency fluctuations that did not resemble oscillations were found (Geva-Zatorsky et al., 2006). These results have been confirmed by *in vivo* experiments (Hamstra et al., 2006) but the precise function of these oscillations is still under investigation (Zhang et al., 2007; Batchelor et al., 2009).

7.3 Mathematical modelling of the p53-Mdm2 gene regulatory network

7.3.1 Literature review

Mathematical models of the p53-Mdm2 system have taken a variety of forms. One of the earliest models was that of Bar-Or et al. (2000), which included an unknown intermediary component to the system representing the delayed synthesis of Mdm2 by p53 (despite extensive research into p53-Mdm2 interactions, no such intermediary has been identified to date). In the experimental paper of Geva-Zatorsky et al. (2006), six temporal models were presented which could explain the oscillatory dynamic observed. The first of these models contained the basic structure of the p53-Mdm2 negative feedback loop and failed to reproduce the oscillatory dynamic. The rest relied on delays or the introduction of nonlinearities to produce the observed oscillatory dynamic. Other authors have chosen different approaches, such as combining positive feedback loops with negative feedback loops in ODE metapopulation-like models (Ciliberto et al., 2005; Zhang et al., 2007). These models were the first to make the important distinction between nuclear and cytoplasmic concentrations. Some models have taken stochastic effects into account (Puszyński et al., 2008; Proctor and Gray, 2008; Ouattara et al., 2010) while others have used time delays (Tiana et al., 2002; Monk, 2003; Mihalas et al., 2006; Ma et al., 2005; Batchelor et al., 2008), in a manner similar to that discussed for the Hes1 GRN previously. A stochastic boolean network approach was formulated and applied to the p53-Mdm2 GRN in Liang and Han (2012). The main advantage of this approach is the cheap computational cost but it may lack the predictive power of other approaches. An attempt was made to model the spatial aspect of the system in Gordon et al. (2009), where an extra species was added to account for

a time delay. A spatio-temporal model of the p53-Mdm2 GRN was recently developed in Sturrock et al. (2011) and extensions were presented in Sturrock et al. (2012) (from which the contents of the next two chapters are taken). Even more recently, another spatio-temporal model of the p53-Mdm2 GRN appeared in the literature which took into account more biology (specifically, post-translational modifications and unidirectional nuclear transport) and yielded oscillatory dynamics for larger ranges of spatial parameters (Dimitrio et al., 2013).

7.3.2 Ordinary differential equation model

Let us denote concentrations of p53, Mdm2 mRNA and Mdm2 by $[p53]$, $[Mdm2m]$ and $[Mdm2]$ respectively. One possible way of translating the reaction schematic presented in Figure 7.1 into an ODE model is as follows:

$$\frac{d[p53]}{dt} = \beta - \left(\mu + \nu\left(\frac{[Mdm2]^{h_1}}{\widehat{Mdm2}^{h_1} + [Mdm2]^{h_1}}\right)\right)[p53], \tag{7.1}$$

$$\frac{d[Mdm2m]}{dt} = \alpha + \eta\left(\frac{[p53]^{h_2}}{\widehat{p53}^{h_2} + [p53]^{h_2}}\right) - \phi[Mdm2m], \tag{7.2}$$

$$\frac{d[Mdm2]}{dt} = \gamma[Mdm2m] - \rho[Mdm2], \tag{7.3}$$

where β, μ, ν, h_1, $\widehat{Mdm2}$, α, h_2, $\widehat{p53}$, ϕ, γ, and ρ are (strictly) positive constants. The ODE describing p53 is composed of a production term β, followed by a natural degradation term of rate μ, and finally a degradation term which is a bounded monotonically increasing function of Mdm2, with parameter ν, Hill coefficient h_1 and activation threshold $\widehat{Mdm2}$. The second ODE, modelling Mdm2 mRNA, has a production

term with basal rate α, followed by an enhanced production term dependent on the amount of p53 (taking the form of a Hill-like function), with rate η, Hill coefficient h_2, and critical concentration $\widehat{p53}$, modelling the activity of p53 as a transcription factor, and finally a natural degradation term of rate ϕ. The final ODE is for Mdm2 protein, which simply has a production term dependent on the amount of Mdm2 mRNA, rate γ, and a natural degradation term, rate ρ. After performing a large number of numerical simulations under a wide range of parameter sets we were not able to find sustained oscillatory dynamics for equations (7.1) – (7.3). For this system, we are not able to apply the classical Dulac's criterion to prove the non-existence of periodic solutions. Instead we adopt the approach outlined in Busenberg and Driessche (1993), which was first demonstrated in Busenberg and Driessche (1990). This approach extends Dulac's criterion to systems in $\mathbb{R}^3$. For a full account of Busenberg's criterion, see Appendix 11.3.1. We now apply this criterion to the system of equations (7.1) – (7.3) in order to prove that oscillatory dynamics can not exist.

Proof. Let $\mathscr{D}$ be an invariant region of the phase space and let $\mathbf{g}(p53, Mdm2m, Mdm2) = [g_1(p53, Mdm2m, Mdm2), g_2(p53, Mdm2m, Mdm2), g_3(p53, Mdm2m, Mdm2)]$ be a vector field which is piecewise smooth on $\mathscr{D}$ which satisfies the conditions

$$\mathbf{g} \cdot \mathbf{f} = 0 \text{ and } (\nabla \times \mathbf{g}) \cdot (1,1,1) < 0 \text{ on } \mathscr{D}^0 = \mathscr{D} - \partial\mathscr{D},$$

where $\partial\mathscr{D}$ is the boundary of $\mathscr{D}$, and where $\mathbf{f} = (f_1, f_2, f_3)$ is a Lipschitz continuous field on $\mathscr{D}^0$. Then the differential equation system $\frac{d[p53]}{dt} = f_1$, $\frac{d[Mdm2m]}{dt} = f_2$, and $\frac{d[Mdm2]}{dt} = f_3$, has no periodic solutions in $\mathscr{D}_0$.

Let f_1, f_2, f_3 denote the right hand side of (7.1), (7.2), and (7.3) respectively, i.e.,

$$\begin{aligned} f_1 &= \beta - \left(\mu + \nu\left(\frac{[Mdm2]^{h_1}}{\widehat{Mdm2}^{h_1} + [Mdm2]^{h_1}}\right)\right)[p53], \\ f_2 &= \alpha + \eta\left(\frac{[p53]^{h_2}}{\widehat{p53}^{h_2} + [p53]^{h_2}}\right) - \phi[Mdm2m], \\ f_3 &= \gamma[Mdm2m] - \rho[Mdm2]. \end{aligned}$$

Let $\mathbf{g}$ take the following form:

$$\begin{aligned} g_1 &= \frac{-1}{f_1}, \\ g_2 &= \frac{1}{2f_2}, \\ g_3 &= \frac{1}{2f_3}. \end{aligned}$$

Clearly, $\mathbf{g}\cdot\mathbf{f} = 0$ on $\mathscr{D}^0$, and some symbolic calculations yield the expression:

$$\begin{aligned} (\nabla\times\mathbf{g})\cdot(1,1,1) &= -\frac{\gamma}{2\left(\gamma[Mdm2m] - \rho[Mdm2]\right)^2} \\ &\quad - \frac{\nu[Mdm2]^{h_1}h_1\widehat{Mdm2}^{h_1}[p53]}{[Mdm2]\left(\left(-\beta + [p53]\nu + [p53]\mu\right)[Mdm2]^{h_1} + \widehat{Mdm2}^{h_1}\left(-\beta + [p53]\mu\right)\right)^2} \\ &\quad - \frac{\eta[p53]^{h_2}h_2\widehat{p53}^{h_2}}{2[p53]\left(\left(-\alpha + \phi[Mdm2m] - \eta\right)[p53]^{h_2} + \widehat{p53}^{h_2}\left(-\alpha + \phi[Mdm2m]\right)\right)^2} \\ &< 0, \end{aligned}$$

which is negative on $\mathscr{D}^0$. Therefore by Corollary 1 (shown in Appendix 11.3.1), there are no periodic solutions in $\mathscr{D}^0$. The invariance of the region $\mathscr{D}$ is easily obtain by

noting that the field **f** given by the right hand side of (7.1) – (7.3), when evaluated on the boundary $\partial\mathscr{D}$ of $\mathscr{D}$, never points towards the exterior of $\mathscr{D}$. □

Hence, although the ODE model seems to account for the important features of the negative feedback loop (Mdm2 enhances degradation of p53), it is unable to reproduce the observed oscillatory dynamics.

7.3.3 Delay differential equation model

As in the case of the Hes1 ordinary differential equation system, Monk (2003) added a delay (represented by τ) to equations (7.1) – (7.3) in order to account for transport, transcription and translation, yielding the following system of DDEs:

$$\frac{d[p53]}{dt} = \beta - \left(\mu + \nu\left(\frac{[Mdm2]^{h_1}}{\widehat{Mdm2}^{h_1} + [Mdm2]^{h_1}}\right)\right)[p53], \tag{7.4}$$

$$\frac{d[Mdm2m]}{dt} = \alpha + \eta\left(\frac{[p53(t-\tau)]^{h_2}}{\widehat{p53}^{h_2} + [p53(t-\tau)]^{h_2}}\right) - \phi[Mdm2m], \tag{7.5}$$

$$\frac{d[Mdm2]}{dt} = \gamma[Mdm2m] - \rho[Mdm2]. \tag{7.6}$$

Numerical simulations of system (7.4) – (7.6) produce oscillations (Monk, 2003), but do not distinguish between events taking place in the nucleus and cytoplasm. The grouping of many processes into one delay term also limits the number of questions that can be asked of the model. Given the success we had with modelling the relatively simple Hes1 GRN, we now adopt a partial differential equation approach to modelling the more complex p53-Mdm2 GRN.

Chapter 8

A reaction-diffusion model of the p53-Mdm2 gene regulatory network

8.1 Introduction

In this chapter, we develop and study a novel spatio-temporal model of the p53-Mdm2 GRN. In a similar manner to chapter 4 we advance previous models by accounting for space, the basic structure of the eukaryotic cell (a nucleus and cytoplasm) and diffusion of intracellular molecules. By accounting for these fundamental features of the eukaryotic cell, we are able to reproduce the oscillatory dynamics observed in experiments without the introduction of delays or additional unknown species.

8.2 Reaction-diffusion model formulation

In our formulation of a PDE model of the p53-Mdm2 GRN, we first modify the system of equations presented in equations (7.1) – (7.3) to include an additional species,

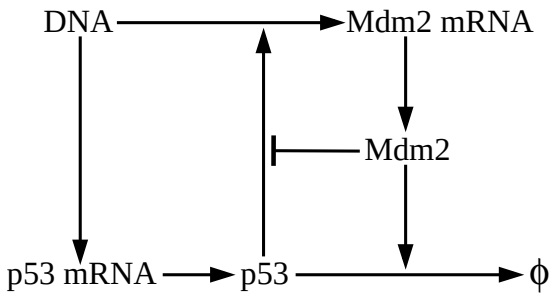

Figure 8.1: *Detailed schematic diagram of the p53-Mdm2 GRN. p53 mRNA produces p53 protein, which then upregulates Mdm2 mRNA expression. Mdm2 then enhances degradation of p53 (through ubiquitination) and inhibits the transcription of Mdm2 mRNA.*

namely, p53 mRNA. This allows for the accurate modelling of p53 translation in the cytoplasm. We also account for inhibition of p53 transcriptional activity by Mdm2; which means our model now accounts for the two main mechanisms of p53 repression by Mdm2 (Thut et al., 1997). However, we wish to stress that this is not necessary to produce oscillatory dynamics. Indeed, by simply adding diffusion and appropriately compartmentalising the ODE system defined by equations (7.1) – (7.3) we can reproduce the oscillatory dynamics observed in the p53-Mdm2 experimental data. In fact, this model was presented and explored in Sturrock et al. (2011). Here we present the model developed in Sturrock et al. (2012) which is displayed schematically in Figure 8.1.

We use the variables $[p53m]$, $[p53]$, $[Mdm2m]$, and $[Mdm2]$ to represent the concentrations of, respectively, p53 mRNA, p53 protein, Mdm2 mRNA, and Mdm2 protein. In keeping with the notation used for the Hes1 GRN models, a subscript n denotes a nuclear concentration and a subscript c denotes a cytoplasmic concentration.

As we did for the Hes1 model, we assume all species are subject to diffusion, mRNA is produced only in the nucleus, and protein is produced only in the cytoplasm. Diffusion coefficients are denoted in a similar manner to the Hes1 system: a subscript

indicates the localisation of the species, with n or c denoting a nuclear or cytoplasmic concentration and a subsubscript 1, 2, 3 or 4 referring to p53 mRNA, p53, Mdm2 mRNA, or Mdm2 respectively. We assume all species are subject to linear decay, with parameters ϕ, μ and ρ denoting mRNA decay, p53 protein decay, and Mdm2 protein decay respectively. In addition, we assume p53 undergoes Mdm2 dependent degradation in both the nucleus and cytoplasm. This is consistent with experimental data which shows that co-compartmentalisation of p53 and Mdm2 results in Mdm2 dependent degradation of p53 (Xirodimas et al., 2001). We assume that this degradation term is equal to a linear decay term with parameter ν, scaled by a bounded monotonically increasing function of Mdm2 protein concentration with Hill coefficient h_1 and activation threshold $\widehat{Mdm2}$. We make the assumption that p53 mRNA is produced at a constant rate ζ and Mdm2 mRNA is produced at a constant rate α. Furthermore, we assume Mdm2 mRNA undergoes nuclear p53 dependent production (taking the form of a Hill-like function), with rate η, Hill coefficient h_2, and critical concentration $\widehat{p53}$. This enhanced production term is also assumed to decrease as nuclear Mdm2 protein levels increase, with parameter θ. This assumption takes into account the fact that Mdm2 protein inhibits the transcriptional activity of p53 (Thut et al., 1997). Finally, we assume protein production occurs a small distance outside the nucleus (as in the case of the Hes1 model) and is dependent on the relevant concentration of mRNA, occurring at rate β for p53 protein and γ for Mdm2 protein.

The complete system of equations is given by:

$$\frac{\partial[p53m_n]}{\partial t} = D_{n_1}\nabla^2[p53m_n] + \zeta - \phi[p53m_n], \tag{8.1}$$

$$\frac{\partial[p53m_c]}{\partial t} = D_{c_1}\nabla^2[p53m_c] - \phi[p53m_c], \tag{8.2}$$

$$\begin{aligned}\frac{\partial[p53_c]}{\partial t} &= D_{c_2}\nabla^2[p53_c] + H(x,y)\beta[p53m_c] \\ &\quad - \left(\mu + \nu\left(\frac{[Mdm2_c]^{h_1}}{\widehat{Mdm2}^{h_1} + [Mdm2_c]^{h_1}}\right)\right)[p53_c],\end{aligned} \tag{8.3}$$

$$\frac{\partial[p53_n]}{\partial t} = D_{n_2}\nabla^2[p53_n] - \left(\mu + \nu\left(\frac{[Mdm2_n]^{h_1}}{\widehat{Mdm2}^{h_1} + [Mdm2_n]^{h_1}}\right)\right)[p53_n], \tag{8.4}$$

$$\begin{aligned}\frac{\partial[Mdm2m_n]}{\partial t} &= D_{n_3}\nabla^2[Mdm2m_n] + \alpha + \eta\left(\frac{[p53_n]^{h_2}}{(\widehat{p53} + [Mdm2_n]/\theta)^{h_2} + [p53_n]^{h_2}}\right) \\ &\quad - \phi[Mdm2m_n],\end{aligned} \tag{8.5}$$

$$\frac{\partial[Mdm2m_c]}{\partial t} = D_{c_3}\nabla^2[Mdm2m_c] - \phi[Mdm2m_c], \tag{8.6}$$

$$\frac{\partial[Mdm2_c]}{\partial t} = D_{c_4}\nabla^2[Mdm2_c] + H(x,y)\gamma[Mdm2m_c] - \rho[Mdm2_c], \tag{8.7}$$

$$\frac{\partial[Mdm2_n]}{\partial t} = D_{n_4}\nabla^2[Mdm2_n] - \rho[Mdm2_n], \tag{8.8}$$

where $H(x,y)$ is the function controlling cytoplasmic protein production in ribosomes defined in equation 4.5.

We apply zero initial conditions, zero-flux boundary conditions at the cell membrane, and continuity of flux boundary conditions across the nuclear membrane:

$$[p53m_n] = [p53m_c] = [p53_n] = [p53_c] = [Mdm2m_n] = [Mdm2m_c] = [Mdm2_n] = [Mdm2_c] = 0 \quad \text{at } t = 0, \tag{8.9}$$

$$D_{n_1}\frac{\partial[p53m_n]}{\partial\mathbf{n}} = D_{c_1}\frac{\partial[p53m_c]}{\partial\mathbf{n}} \text{ and } [p53m_n]=[p53m_c] \text{ at nuclear membrane,} \tag{8.10}$$

$$D_{n_2}\frac{\partial[p53_n]}{\partial\mathbf{n}} = D_{c_2}\frac{\partial[p53_c]}{\partial\mathbf{n}} \text{ and } [p53_n]=[p53_c] \text{ at nuclear membrane,} \tag{8.11}$$

$$D_{n_3}\frac{\partial[Mdm2m_n]}{\partial\mathbf{n}} = D_{c_3}\frac{\partial[Mdm2m_c]}{\partial\mathbf{n}} \text{ and } [Mdm2m_n]=[Mdm2m_c] \text{ at nuclear membrane,} \tag{8.12}$$

$$D_{n_4}\frac{\partial[Mdm2_n]}{\partial\mathbf{n}} = D_{c_4}\frac{\partial[Mdm2_c]}{\partial\mathbf{n}} \text{ and } [Mdm2_n]=[Mdm2_c] \text{ at nuclear membrane,} \tag{8.13}$$

$$\frac{\partial[p53m_c]}{\partial\mathbf{n}} = 0 \quad \text{at cell membrane,} \tag{8.14}$$

$$\frac{\partial[p53_c]}{\partial\mathbf{n}} = 0 \quad \text{at cell membrane,} \tag{8.15}$$

$$\frac{\partial[Mdm2m_c]}{\partial\mathbf{n}} = 0 \quad \text{at cell membrane,} \tag{8.16}$$

$$\frac{\partial[Mdm2_c]}{\partial\mathbf{n}} = 0 \quad \text{at cell membrane.} \tag{8.17}$$

As the p53 pathway is known to play a role in the development of osteosarcomas (Diller et al., 1990), we choose the imported shape of an osteosarcoma cell shown in Figure 5.13 as our domain. Our objective is to study sustained oscillatory dynamics, so we must find non-dimensional parameter values such that our model yields such dynamics. Nearly all of the parameters in our new modified model are contained in the original p53-Mdm2 model in Sturrock et al. (2011), which has already been studied in the context of oscillations. Hence, for these parameters, we choose the non-dimensional values used for the original model, which are stated in equation (60) in Sturrock et al. (2011). The remaining parameters are ζ and θ, for which we have found appropriate values by a simulation study. From our non-dimensional parameter values, we have calculated dimensional values and these are stated in the third column of Table 8.1. Details regarding non-dimensionalisation and the calculation of dimensional parameter values can be found in Appendix 11.3.2. As in section 4.3, all nuclear and cytoplasmic diffusion coefficients are made equal to each other, and we retain the notation D_{i_j} to indicate diffusion of species i (mRNA or protein) in location j (nucleus or cytoplasm).

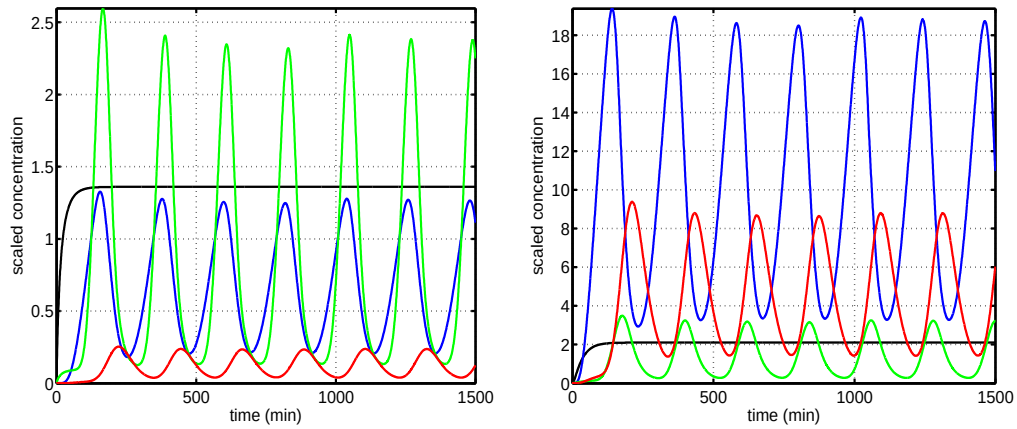

(a) *nuclear compartment* **(b)** *cytoplasmic compartment*

Figure 8.2: *Plots of the total concentrations of p53 mRNA (black), p53 (blue), Mdm2 mRNA (green), and Mdm2 (red) in (a) the nucleus and (b) the cytoplasm, for the p53-Mdm2 reaction-diffusion model. The period of oscillation is approximately 215 minutes. Parameter values as per column 2, Table 8.1.*

8.3 Numerical simulation results

We present here the numerical solutions of the PDE system defined by equations (8.1) – (8.8) subject to conditions (8.9) – (8.17) and parameters from the third column of Table 8.1. Figure 8.2 shows the total concentrations of p53 and Mdm2 in the nucleus and cytoplasm.

As in the case of numerical simulations of our Hes1 GRN reaction-diffusion model, we find that our spatio-temporal model of the p53-Mdm2 GRN yields sustained oscillatory dynamics. In addition, the period of oscillation lies in the 3 to 7 hour range of experimentally measured periods (Bar-Or et al., 2000; Geva-Zatorsky et al., 2006). We note that p53 mRNA levels reach a steady state because they are not involved directly in a negative feedback loop. These total concentration plots reveal that the mRNA concentration (for both p53 and Mdm2) is higher in the nucleus compared to the protein concentrations and vice versa for the cytoplasmic compartment. For the particular parameter set we chose (see column 3, Table 8.1) we find larger amplitude oscillations for p53 protein rather than Mdm2 protein — this is a phenomenon not inconsistent with

time course data for some cells presented in Geva-Zatorsky et al. (2010). We present plots in Figure 8.3 of how the dynamics of the p53-Mdm2 system evolve in space as well as time.

The spatial snapshots of Figure 8.3 can readily be compared with time-lapse microscopy images of individual cells with p53 and Mdm2 proteins fluorescently tagged (for example, a comparison can be made with Figure 1 of Geva-Zatorsky et al. (2010). In Figure 8.3a, we see that p53 has accumulated in the cytoplasm at $t = 300$ minutes. p53 then begins to diffuse across the nuclear boundary and enter the nucleus at $t = 360$ minutes. The presence of p53 in the nucleus upregulates the expression of Mdm2 (via Mdm2 mRNA) which results in enhanced decay of p53 (see $t = 420$ minutes). By $t = 540$ minutes, the p53 concentration begins to increase again, giving a period of oscillation of approximately 3 hours.

Figure 8.3b shows the plots of Mdm2 protein concentration over time. Notice that Mdm2 appears in abundance at $t = 420$ minutes, 60 minutes after p53 appears in abundance, reflecting the time for Mdm2 mRNA production, export from the nucleus and translation in the cytoplasm. The presence of Mdm2 in the cell causes the enhancement of p53 degradation which in turn causes the down-regulation of Mdm2 expression. This is shown at $t = 540$ minutes where Mdm2 levels have depleted considerably. The negative feedback Mdm2 exerts on p53 is made clear in these spatial plots by the fact that wherever Mdm2 levels are high in the cell, p53 levels are low and vice versa.

8.4 Parameter values

We have found ranges of values for all of the parameters in our reaction-diffusion model of the p53-Mdm2 GRN such that it exhibits sustained oscillatory dynamics, where (as in section 4.3) we define such dynamics as at least 5 distinct peaks in the total

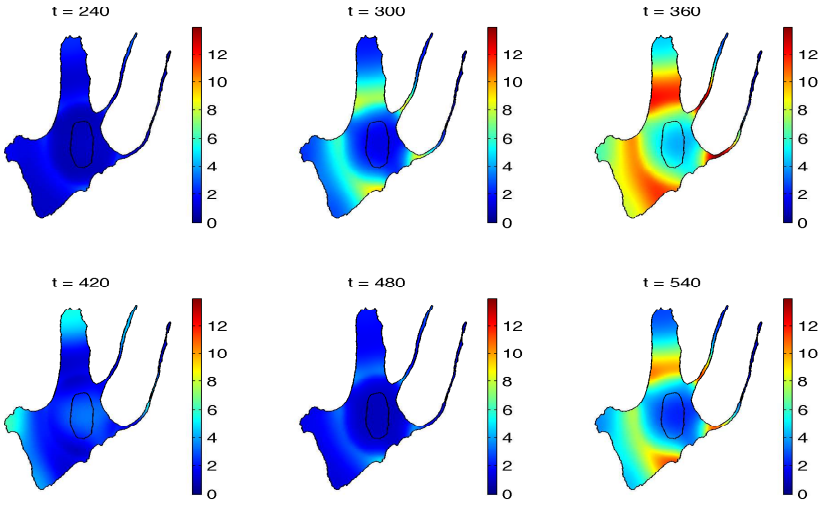

(a) *p53*

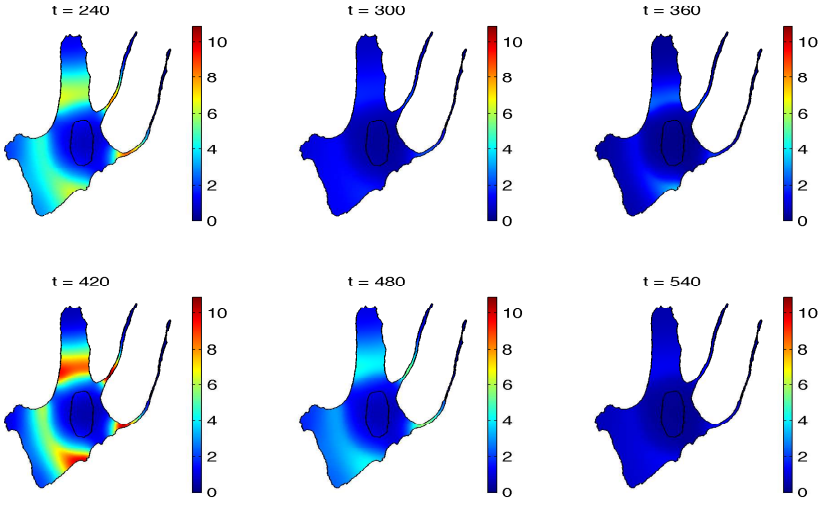

(b) *Mdm2*

Figure 8.3: *Plots showing the spatio-temporal evolution of (a) p53 and (b) Mdm2 within the osteosarcoma cell domain from times* $t = 240$ *to* $t = 540$ *minutes at* 60 *minute intervals for the reaction-diffusion p53-Mdm2 model. The concentrations exhibit oscillatory dynamics in both time and space. Parameter values as per column 3, Table 8.1.*

concentration of the transcription factor (in this case, p53) in the nucleus. Choosing this criteria rules out any heavily damped oscillatory solutions of our model but does not ignore solutions exhibiting sustained oscillatory dynamics. These ranges are given in the fourth column in Table 8.1. To find the range for each parameter, we varied it whilst holding all the other parameters fixed at their 'default' values, the dimensional versions of which are stated in the third column of Table 8.1.

Parameter	Description	Value in simulations	Range over which oscillations are observed
D_{i_j}	Diffusion coefficient of species i in compartment j	$3.00 \times 10^{-11}\text{cm}^2\text{s}^{-1}$	$1.00 \times 10^{-11}\text{cm}^2\text{s}^{-1}$ to $1.67 \times 10^{-8}\text{cm}^2\text{s}^{-1}$
ζ	Basal rate of p53 mRNA transcription	$2.92 \times 10^{-10}\text{Ms}^{-1}$	$\geq 5.83 \times 10^{-11}\text{Ms}^{-1}$
ϕ	Degradation rate of mRNA	$5.83 \times 10^{-4}\text{s}^{-1}$	$1.00 \times 10^{-4}\text{s}^{-1}$ to $1.10 \times 10^{-3}\text{s}^{-1}$
β	Translation rate of p53	0.33s^{-1}	$\geq 5.13 \times 10^{-2}\text{s}^{-1}$
μ	Degradation rate of p53	$1.00 \times 10^{-4}\text{s}^{-1}$	$\leq 4.33 \times 10^{-4}\text{s}^{-1}$
ν	Mdm2 dependent degradation of p53	$3.33 \times 10^{-2}\text{s}^{-1}$	$1.67 \times 10^{-3}\text{s}^{-1}$ to 3.33s^{-1}
h_1	Hill coefficient for Mdm2 dependent degradation of p53	2	≥ 1
$\widehat{Mdm2}$	Activation threshold for Mdm2 dependent degradation of p53	$3.20 \times 10^{-5}\text{M}$	$3.20 \times 10^{-6}\text{s}^{-1}$ to $2.10 \times 10^{-4}\text{s}^{-1}$
α	Basal rate of Mdm2 mRNA transcription	$2.92 \times 10^{-11}\text{Ms}^{-1}$	$\leq 2.25 \times 10^{-10}\text{Ms}^{-1}$
η	Maximal p53 dependent transcription of Mdm2 mRNA	$1.67 \times 10^{-9}\text{Ms}^{-1}$	$\geq 2.08 \times 10^{-10}\text{Ms}^{-1}$
h_2	Hill coefficient for p53 dependent transcription	4	≥ 1
$\widehat{p53}$	Threshold parameter of p53	$2.50 \times 10^{-6}\text{M}$	$\leq 1.65 \times 10^{-5}\text{M}$
θ	Mdm2 inhibition of p53 transcription	4.00	$\geq 15.60 \times 10^{-3}$
γ	Translation rate of Mdm2	0.67s^{-1}	$\geq 0.10\text{s}^{-1}$
ρ	Degradation rate of Mdm2	$8.33 \times 10^{-4}\text{s}^{-1}$	$1.33 \times 10^{-4}\text{s}^{-1}$ to $7.00 \times 10^{-3}\text{s}^{-1}$
l	Minimum radial distance of translation from centre of nucleus	$6.32\mu\text{m}$	$3.46\mu\text{m}$ to $9.27\mu\text{m}$

Table 8.1: *Description of parameters in the p53-Mdm2 reaction-diffusion model defined in section 8.1, values used in simulations, and ranges over which sustained oscillatory dynamics are observed.*

The p53-Mdm2 model permits oscillatory dynamics for a wide range of diffusion coefficients, which include the experimentally measured values of Matsuda et al. (2008) and Seksek et al. (1997). Only two of the parameters in Table 8.1 have been measured experimentally, namely the degradation rate μ of p53 protein and the degradation rate ρ of Mdm2 protein. According to Finlay (1993), these degradation rates are approximately $3.85 \times 10^{-4}\text{s}^{-1}$ for both p53 and Mdm2. This value lies within the ranges calculated which produce oscillatory dynamics (see Table 8.1 entries for μ and ρ).

Assuming that the decay rates of p53 mRNA and Mdm2 mRNA are of roughly the same order as the decay rate of hes1 mRNA, which has been estimated experimentally at $4.83 \times 10^{-4}\text{s}^{-1}$ (Hirata et al., 2002), then the range presented for ϕ is in agreement with experimentally measured values. To calculate the value and range for the parameter l, defined in Table 8.1 as the minimum radial distance of translation from the centre of the nucleus, we took the centre of the nucleus to be the origin in the non-dimensional domain in Figure 5.13. Interestingly, we find that protein translation must begin a small distance from the nuclear membrane for this case. Our ranges of values for the remaining parameters in Table 8.1 are consistent with the values found in the modelling literature, where analogous parameters exist (Proctor and Gray, 2008; Ciliberto et al., 2005; Puszyński et al., 2008; Geva-Zatorsky et al., 2006).

8.5 Proteasome inhibition numerical experiment

In this section, we consider the implications of treating the p53-Mdm2 GRN with proteasome inhibitors. It is known that exposing cells to proteasome inhibitors results in increased levels of p53 and Mdm2. In particular, it was shown in Maki et al. (1996) that gamma-irradiated cells treated with the proteasome inhibitor MG115 caused increased expression of p53. More recently, experiments conducted by Xirodimas et al. (2001) revealed that by treating cells with proteasome inhibitor MG132, both p53 and Mdm2 levels increased. Furthermore, both proteins localised in the nucleus. To model this effect, we decrease the protein degradation parameters, μ, ν, and ρ by a factor λ, which we will refer to as the *inhibition factor*. All other parameter values used for the simulations are as detailed in column 3, Table 8.1, but we divide μ, ν, and ρ by $\lambda = 300$ so that their values become:

$$\mu = 3.33 \times 10^{-7}\text{s}^{-1},\ \nu = 1.11 \times 10^{-4}\text{s}^{-1},\ \rho = 2.78 \times 10^{-6}\text{s}^{-1}. \tag{8.18}$$

In Figure 8.4 we can see how the decrease in protein degradation parameters has affected the total concentrations of the variables in our p53-Mdm2 GRN model. The numerical solutions no longer display oscillatory dynamics, but instead Mdm2 levels increase monotonically and p53 levels appear to saturate and reach a steady state. The total concentrations quickly exceed the levels in Figure 8.2 where the proteasome was not inhibited. Both p53 and Mdm2 appear in larger quantities in the cytoplasm as opposed to the nucleus. Mdm2 mRNA levels remain low in spite of increased levels of p53 as a result of Mdm2 protein directly inhibiting p53 transcriptional activity. Unsurprisingly, p53 mRNA levels are unaffected by this numerical experiment.

The spatial plots presented in Figure 8.5 show the spatial distributions of p53 and Mdm2 concentrations at $t = 1500$ minutes. Mdm2 concentrations are distributed evenly throughout the cell by this time and p53 concentrations are located mainly in the cytoplasm (where they are originally created). Although Mdm2 dependent degradation of p53 is decreased, it is not zero, so p53 is more likely to be found where it is initially made (i.e., the cytoplasm). Hence, our model was not able to reproduce the observed experimental phenomenon of p53 and Mdm2 localising in the nucleus. This implies our modelling assumptions are in some way flawed or not faithful to the underlying biology.

8.6 Discussion

The p53-Mdm2 GRN is known to have a central role in the response of the cell to cytotoxic or radiotoxic insults resulting in DNA damage. The localisation of p53 is

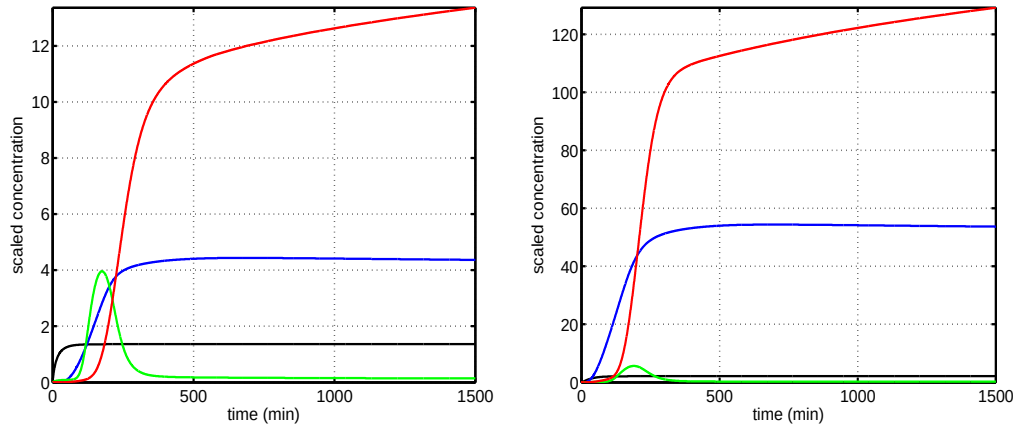

(a) *nuclear compartment* **(b)** *cytoplasmic compartment*

Figure 8.4: *Plots of the total concentrations of p53 mRNA (black), p53 (blue), Mdm2 mRNA (green) and Mdm2 (red) in (a) the nucleus and (b) the cytoplasm, for the p53-Mdm2 reaction-diffusion model. Parameter values as per column 3, Table 8.1, with the exception of parameters μ, ν, and ρ which are specified in equation* (8.18)*. The total concentrations of Mdm2 continue to increase over the* 1500 *minute time interval and accumulate mainly in the cytoplasmic compartment, whereas p53 levels saturate after $t = 250$ minutes, accumulating mainly in the cytoplasmic compartment.*

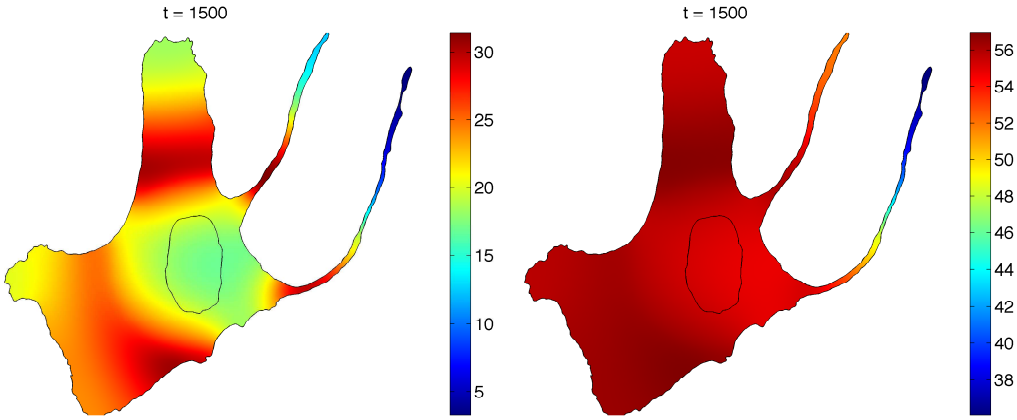

(a) *p53 concentration* **(b)** *Mdm2 concentration*

Figure 8.5: *Plots showing the spatial distribution of (a) p53 and (b) Mdm2 within the osteosarcoma cell domain of Figure 5.13 at time $t = 1500$ minutes, for the p53-Mdm2 reaction-diffusion model. The concentrations of p53 are localised mainly in the cytoplasm whereas Mdm2 is almost homogeneously distributed throughout the cell. Parameter values as per column 3, Table 8.1, with the exception of parameters μ, ν, and ρ which are specified in equation* (8.18)*.*

very important for maintaining cellular homeostasis and it is known to be mislocalised in many forms of human cancer (for a complete list, see Table 4 in O'Brate and Giannakakou (2003) and references therein). Furthermore hindering p53 translocation to the nucleus alters the transcriptome of the cell and contributes to carcinogenesis (Vousden and Prives, 2009). Hence a spatio-temporal model of the p53-Mdm2 GRN could shed light on processes that have clinical significance.

In this chapter, we have presented a reaction-diffusion model of the p53-Mdm2 GRN. It is known that p53 and Mdm2 concentrations can exhibit a dynamical, oscillatory response to gamma irradiation at the single cell level. Our numerical simulations reflect experimental findings both *in vitro* (Hirata et al., 2002; Geva-Zatorsky et al., 2006) and *in vivo* (Hamstra et al., 2006) and mark a conceptual advance in the modelling of intracellular processes. Furthermore, our period of oscillation (3.6 hours) fell within the 3 to 7 hour range measured in experiments (Bar-Or et al., 2000; Geva-Zatorsky et al., 2006). Additional complexities of post-transcriptional mRNA and post-translational protein modifications, while not explicitly incorporated into the model, occur within the timescales modelled and do not fundamentally change the sequence or timing of events.

Where possible, parameter values were taken from experimental measurements, otherwise they were chosen to be in agreement with other recent modelling efforts. As in the case of the Hes1 GRN, we demonstrated that the model is robust to changes in parameter values (when varying one parameter at a time).

Our proteasome inhibition numerical experiment highlighted an inconsistency between our numerical simulations and real biological data. In a biological experiment, treatment of a cell with proteasome inhibitor MG132 resulted in both p53 and Mdm2 proteins localising in the nucleus Xirodimas et al. (2001). However, our numerical experiment predicted p53 to localise mainly in the cytoplasm and Mdm2 to distribute itself

almost evenly throughout the cell. This led us to rethink our modelling assumptions and the next chapter contains a modified model of the p53-Mdm2 GRN that extends the one presented in this chapter and rectifies the inconsistency found in the proteasome inhibition experiment.

Chapter 9

The influence of the nuclear membrane and active transport on the p53-Mdm2 gene regulatory network

9.1 Introduction

In this chapter we consider extensions to the p53-Mdm2 reaction-diffusion model presented in chapter 8. The extensions we consider can only be made in an explicitly spatial setting and provide insight into the way p53 is transported into the nucleus.

9.2 Extended p53-Mdm2 model formulation

We now extend the p53-Mdm2 model defined in section 8.1 to include a nuclear membrane and active transport. The importance of modelling the nuclear membrane explicitly has been made clear in section 5.2 but, in terms of the p53-Mdm2 GRN specifically,

it is worth noting that p53 nucleocytoplasmic transport is known to be tightly regulated and that disruption to this transport can play a role in tumorigenesis (Ryan et al., 2001). We define the explicit nuclear membrane boundary conditions in a similar manner to the Hes1 model in section 5.2. Thus, recalling our notation from section 8.1 that D_{i_j} indicates diffusion of species i (mRNA or protein) in location j (nucleus or cytoplasm), and still assuming that D_{i_j} is constant (independent of i and j), we define mRNA and protein diffusion coefficients in the nuclear membrane as, respectively, $D_m = D_{i_j}/5$ and $D_p = D_{i_j}/15$ to reflect slow mRNA diffusion across the nuclear membrane and even slower protein diffusion, and we replace boundary conditions (8.10) – (8.13) with boundary conditions appropriate for a permeable thin boundary layer of thickness d defined by:

$$
\begin{aligned}
D_{n_1}\frac{\partial[p53m_n]}{\partial \mathbf{n}} &= \frac{D_m([p53m_n]-[p53m_c])}{d}, && (9.1)\\
D_{c_1}\frac{\partial[p53m_c]}{\partial \mathbf{n}} &= \frac{D_m([p53m_c]-[p53m_n])}{d}, && (9.2)\\
D_{n_2}\frac{\partial[p53_n]}{\partial \mathbf{n}} &= \frac{D_p([p53_n]-[p53_c])}{d}, && (9.3)\\
D_{c_2}\frac{\partial[p53_c]}{\partial \mathbf{n}} &= \frac{D_p([p53_c]-[p53_n])}{d}, && (9.4)\\
D_{n_3}\frac{\partial[Mdm2m_n]}{\partial \mathbf{n}} &= \frac{D_m([Mdm2m_n]-[Mdm2m_c])}{d}, && (9.5)\\
D_{c_3}\frac{\partial[Mdm2m_c]}{\partial \mathbf{n}} &= \frac{D_m([Mdm2m_c]-[Mdm2m_n])}{d}, && (9.6)\\
D_{n_4}\frac{\partial[Mdm2_n]}{\partial \mathbf{n}} &= \frac{D_p([Mdm2_n]-[Mdm2_c])}{d}, && (9.7)\\
D_{c_4}\frac{\partial[Mdm2_c]}{\partial \mathbf{n}} &= \frac{D_p([Mdm2_c]-[Mdm2_n])}{d}. && (9.8)
\end{aligned}
$$

In terms of active transport, it is known that p53 is shuttled towards the nucleus along microtubules (O'Brate and Giannakakou, 2003; Lomakin and Nadezhdina, 2010). Although there is no direct evidence for Mdm2 transport along microtubules, there is evidence to suggest that Mdm2 can be actively transported to the nucleus (Mayo and

Donner, 2001). Therefore, as we did in section 5.2 for the Hes1 model, we shall include convection terms in the cytoplasmic protein equations to account for active transport, which changes equations (8.3) and (8.7) to the following:

$$\begin{aligned}\frac{\partial [p53_c]}{\partial t} &= D_{c_1}\nabla^2[p53_c] - \nabla\cdot(\mathbf{a}\,[p53_c]) + H(x,y)\beta[p53m_c] \\ &\quad - \left(\mu + \nu\left(\frac{[Mdm2_c]^{h_1}}{\widehat{Mdm2}^{h_1} + [Mdm2_c]^{h_1}}\right)\right)[p53_c], \qquad (9.9)\\ \frac{\partial [Mdm2_c]}{\partial t} &= D_{c_3}\nabla^2[Mdm2_c] - \nabla\cdot(\mathbf{a}\,[Mdm2_c]) + H(x,y)\gamma[Mdm2m_c] \\ &\quad - \rho[Mdm2_c], \qquad (9.10)\end{aligned}$$

where the convective velocity **a** is defined as in equation (5.6) and is plotted in Figure 5.1. As we did for the extended Hes1 model, we assume that convection does not occur in the region between the MTOC and the nuclear membrane (the orange region in Figure 5.2). Hence, in this region, equations (8.3) and (8.7) apply.

9.3 Numerical simulation results

We performed simulations of the extended p53-Mdm2 model given by equations (8.1) – (8.8) and (9.9) – (9.10) subject to conditions (8.9), (8.14) – (8.17) and (9.1) – (9.6). We retained the parameter values used to simulate the p53-Mdm2 reaction-diffusion model stated in section 8.4 and for the additional parameters introduced by extending the model we chose values to give numerically stable sustained oscillations. Our parameter values are summarised in the second column of Table 9.1. As in the previous chapter, details regarding non-dimensionalisation and the calculation of dimensional parameter values can be found in Appendix 11.3.2. Parameter ranges such that the

extended model exhibits sustained oscillatory dynamics (defined as at least 5 peaks of p53 in the nucleus) were found and are stated in the third column of Table 9.1.

Notice that most of the ranges in Table 9.1 are wider than those in Table 8.1, and in particular this is true for the diffusion coefficient. Hence, as we found for the Hes1 model, extending the p53-Mdm2 model to include a nuclear membrane and active transport makes it a more robust oscillator. Our rate of active transport in the second column of Table 9.1 is similar to the rate of active transport used in the Hes1 model in Table 5.1. However, notice that, unlike in Table 5.1, our range of values for the active transport rate in Table 9.1 includes zero. Hence active transport is not needed for sustained oscillatory dynamics in the extended p53-Mdm2 model (see section 9.4 below). The parameter l permits oscillations over a larger range than in Table 5.1 but still does not permit sustained oscillations when translation occurs too close to the nucleus.

Parameter	Value in simulations	Range over which oscillations are observed
D_{i_j}	$3.00\times10^{-11}\text{cm}^2\text{s}^{-1}$	$3.67\times10^{-12}\text{cm}^2\text{s}^{-1}$ to $5.33\times10^{-8}\text{cm}^2\text{s}^{-1}$
ζ	$2.92\times10^{-10}\text{Ms}^{-1}$	$\geq 9.12\times10^{-12}\text{Ms}^{-1}$
ϕ	$5.83\times10^{-4}\text{s}^{-1}$	$2.00\times10^{-4}\text{s}^{-1}$ to $1.87\times10^{-4}\text{s}^{-1}$
β	0.33s^{-1}	$\geq 9.33\times10^{-3}\text{s}^{-1}$
μ	$1.00\times10^{-4}\text{s}^{-1}$	$\leq 1.67\times10^{-3}\text{s}^{-1}$
ν	$3.33\times10^{-2}\text{s}^{-1}$	$6.67\times10^{-4}\text{s}^{-1}$ to 1.17s^{-1}
h_1	2	≥ 1
$\widehat{Mdm2}$	$3.2\times10^{-5}\text{M}$	$5.60\times10^{-6}\text{M}$ to $8.00\times10^{-4}\text{M}$
α	$2.92\times10^{-11}\text{Ms}^{-1}$	$\leq 1.50\times10^{-10}\text{Ms}^{-1}$
η	$1.67\times10^{-9}\text{Ms}^{-1}$	$\geq 1.04\times10^{-10}\text{Ms}^{-1}$
h_2	4	≥ 1
$\widehat{p53}$	$2.50\times10^{-6}\text{M}$	$\leq 1.13\times10^{-4}\text{M}$
θ	4.00	$\geq 1.56\times10^{-2}$
γ	0.67s^{-1}	$\geq 0.05\text{s}^{-1}$
ρ	$8.33\times10^{-4}\text{s}^{-1}$	$2.33\times10^{-4}\text{s}^{-1}$ to $3.67\times10^{-3}\text{s}^{-1}$
D_m	$6.00\times10^{-12}\text{cm}^2\text{s}^{-1}$	$\geq 2.22\times10^{-14}\text{cm}^2\text{s}^{-1}$
D_p	$2.00\times10^{-12}\text{cm}^2\text{s}^{-1}$	$\geq 7.43\times10^{-15}\text{cm}^2\text{s}^{-1}$
d	$1.00\times10^{-5}\text{cm}$	$\leq 1.00\times10^{-3}\text{cm}$
a	$1.00\times10^{-6}\text{cms}^{-1}$	$\leq 5.83\times10^{-5}\text{cms}^{-1}$
l	$6.32\mu\text{m}$	$3.87\mu\text{m}$ to $11.8\mu\text{m}$

Table 9.1: *Parameter values used in the extended p53-Mdm2 model and ranges over which sustained oscillatory dynamics are observed.*

Figure 9.1 shows how the total concentrations of the variables in the extended p53-Mdm2 model vary over time in both the nucleus and cytoplasm. The model has

changed significantly from that which was presented in the previous chapter but the solution still exhibits oscillatory dynamics (compare Figures 9.1a and 9.1b with Figures 8.2a and 8.2b). However, there are numerous quantitative differences in the numerical solution. For instance, a far larger proportion of the p53 and Mdm2 proteins now enters the nucleus, on account of being actively transported towards it and despite the barrier of slower diffusion across the nuclear membrane. To be more specific, Figure 8.2 show that peaks in nuclear p53 total concentration are approximately 8% the height of peaks in cytoplasmic p53 total concentration, whereas in Figure 9.1 in our new results this has changed to 33%. For Mdm2, the change is from approximately 2.5% to 33%. The peaks in p53 total nuclear concentration are taller and narrower in our new results, exhibiting pulsatile-like dynamics and dropping to zero between consecutive peaks. Such dynamics are consistent with recent experimental data showing that, in response to DNA damage, p53 exhibits sharp pulses (Batchelor et al., 2009; Loewer et al., 2010). The period of oscillation is now shorter than the period observed for the reaction-diffusion model of the previous chapter. The observed period for the extended model is 3 hours, which is consistent with experimental data (Bar-Or et al., 2000; Geva-Zatorsky et al., 2006). As we mentioned in the previous chapter, p53 mRNA does not exhibit oscillations since it is not involved in a negative feedback loop and is not coupled to any other equations — this is why we can see steady state levels of p53 mRNA in Figure 9.1.

In Figure 9.2 we show spatial profiles for p53 and Mdm2 from times $t = 240$ minutes to $t = 540$ minutes at 60 minute intervals. At $t = 240$ minutes, it can be observed that p53 has accumulated in the cytoplasm and nucleus. In the nucleus it upregulates Mdm2 mRNA transcription, which leads to increased production of Mdm2 in the cytoplasm ($t = 300$ minutes). Mdm2 enhances degradation of p53, both in the cytoplasm and in the nucleus. In particular, since Mdm2 is actively transported to the nucleus, then Mdm2 dependent degradation of p53 is sufficiently strong to eradicate p53 there

($t = 360$ minutes). Mdm2 levels fall through natural degradation, which frees p53 from Mdm2 dependent degradation and allows levels of p53 to rise in the cytoplasm. Levels of p53 quickly then rise in the nucleus through active transport ($t = 420$ minutes). The process just described now repeats, producing oscillatory dynamics. The 180 minute period of oscillations is clear from Figure 9.2. It is also clear that the nuclear membrane retards the nuclear entry of p53 and Mdm2 — the local concentrations reach their highest levels in or next to the nuclear membrane. This result reinforces the idea, discussed in Gasiorowski and Dean (2003) and Chahine and Pierce (2009), that the nuclear pore complex is an attractive site for delivering chemotherapeutic drugs to disrupt or enhance intracellular signalling. Exploiting the spatial nature of our approach, we created 'computational animations' of the numerical solution of the extended p53-Mdm2 model. These animations can be readily compared with the experimental results obtained by Lahav et al. (2004) (supporting online material) where fluorescent fusion proteins were employed to visualise the protein concentration levels inside single cells. Upon doing this we find good qualitative agreement between the numerical solution and the experimental data.

As was the case with the extended Hes1 model in section 5.5, we found in the extended p53-Mdm2 model that oscillatory dynamics could occur even when the cytoplasmic protein diffusion coefficients were all set to zero (results not shown). In other words, it is possible to observe sustained oscillatory dynamics when proteins are transported to the nucleus by convection alone.

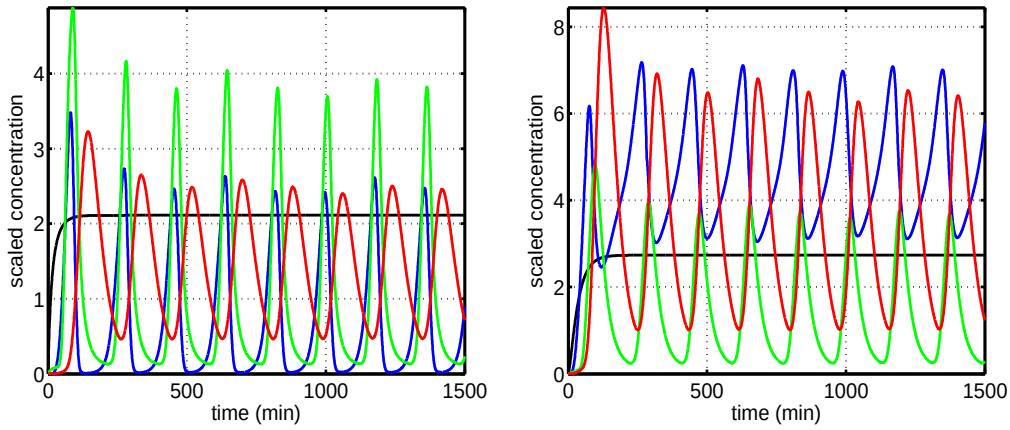

(a) *nuclear compartment* **(b)** *cytoplasmic compartment*

Figure 9.1: *Plots of the total concentrations of p53 mRNA (black), p53 (blue), Mdm2 mRNA (green), and Mdm2 (red) in (a) the nucleus and (b) the cytoplasm, for the extended p53-Mdm2 model. The period of oscillation is approximately* 180 *minutes. Parameter values as per column 2, Table 9.1.*

9.4 Microtubule disruption numerical experiment

In section 5.6 we mentioned that microtubules are seen as an attractive target for chemotherapeutic drugs. Hence we now consider the effect of such drugs in our extended p53-Mdm2 model. The effect of such drugs will be to disrupt active transport and therefore we set the active transport rate a equal to zero in our extended model. All other parameter values are as per the second column of Table 9.1 (for convenience, the complete set of parameters is also stated in the second column of Table 9.2 below).

Figure 9.3 shows the total concentrations for all model species over time. Sustained oscillatory dynamics can be seen but the oscillations are now smoother than when active transport was permitted, levels of nuclear p53 no longer drop to zero between successive peaks, the amplitude of p53 oscillations has grown enormously relative to Mdm2 oscillations in both the nucleus and the cytoplasm, and the oscillatory period has significantly increased (compare Figure 9.3 with Figure 9.1). The period is still in the range of experimental measurements (Bar-Or et al., 2000). There are also reductions in the overall amounts of nuclear p53 and nuclear Mdm2. For p53, peaks in total nuclear

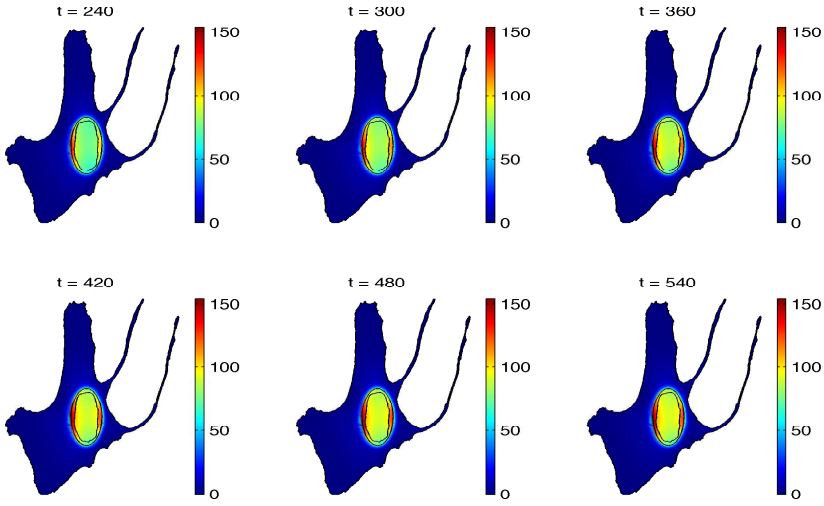

(a) *p53*

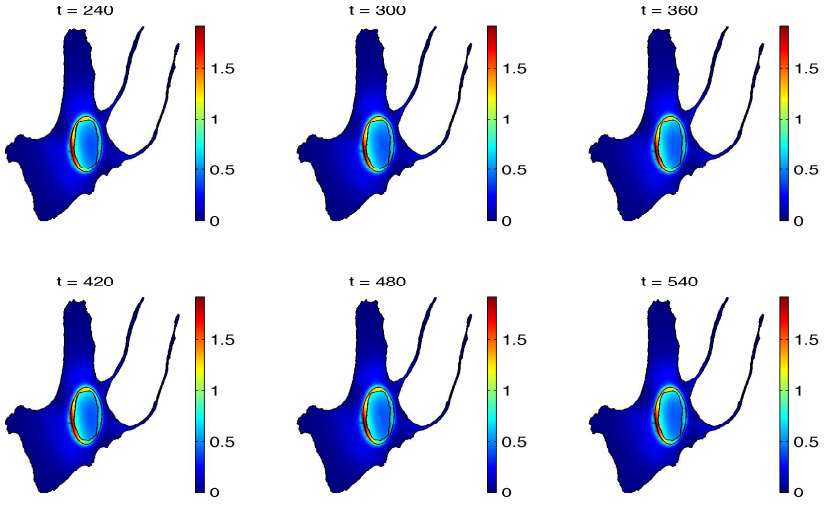

(b) *Mdm2*

Figure 9.2: *Plots showing the spatio-temporal evolution of (a) p53 and (b) Mdm2 within the osteosarcoma cell domain from times* $t = 240$ *to* $t = 540$ *minutes at* 60 *minute intervals for the extended p53-Mdm2 model. The concentrations exhibit oscillatory dynamics in both time and space. Parameter values as per column 2, Table 9.1.*

concentration are approximately 6% of the height of peaks in total cytoplasmic concentration in Figure 9.3, reduced from 33% in Figure 9.1, while for Mdm2 the reduction is from 33% in Figure 9.1 to 2.5% in Figure 9.3. These latter findings are consistent with *in vivo* experiments showing that the microtubule-depolymerizing agent nocodazole causes levels of nuclear p53 to fall (Roth et al., 2007), and is also consistent with experiments showing that the treatment of cells with microtubule-disrupting agents before subjecting these cells to DNA damage causes both nuclear p53 and nuclear Mdm2 levels to fall (Giannakakou et al., 2000).

Figure 9.4 shows spatial profiles for p53 and Mdm2 from times $t = 240$ minutes to $t = 540$ minutes at 60 minute intervals. These proteins are produced in the cytoplasm by the process of translation, a process which we earlier assumed to occur at least some minimal distance from the nuclear membrane. This assumption has a clear impact on the local concentrations of p53 and Mdm2 in Figure 9.4. New production of p53 and Mdm2 is maximal at this minimal distance where, by our assumptions, p53 mRNA and Mdm2 mRNA molecules diffusing outwards from the nucleus will first encounter ribosomes. Newly synthesised p53 and Mdm2 diffuse outwards into the cytoplasm, reaching the cell membrane in many places.

The spatial profiles in Figure 9.4 are quite different to those in Figure 9.2 where active transport was permitted and forced newly synthesised p53 and Mdm2 to rapidly translocate towards the nucleus. In the absence of directed transport towards the nucleus, the local concentrations of p53 and Mdm2 within or next to the nuclear membrane are hugely reduced. There is a chemotherapeutic implication. Chemotherapeutic drugs are often used in combination, a practice known as combination chemotherapy (Ferrari and Palmerini, 2007; Robati et al., 2008). The biggest advantage to this practice is that it minimises the chances of resistance developing to any one agent. Drugs which target proteins at the nuclear membrane will be ineffective if little of

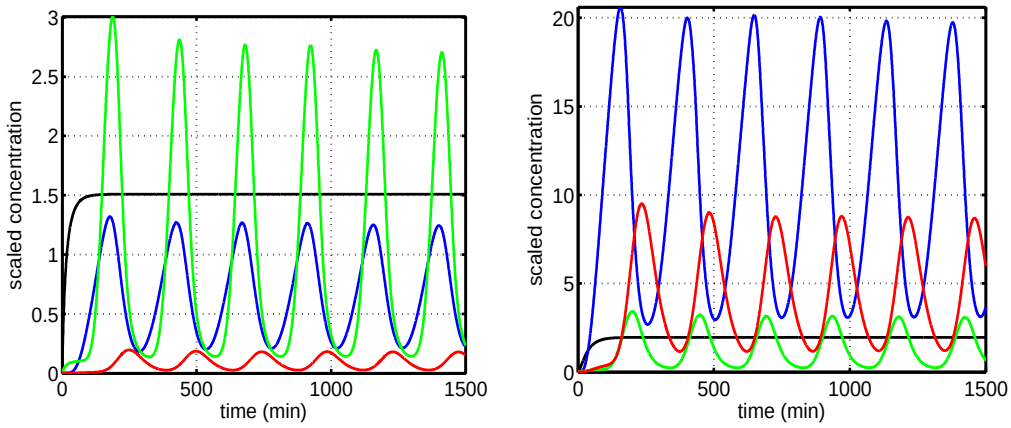

(a) *nuclear compartment* **(b)** *cytoplasmic compartment*

Figure 9.3: *Plots of the total concentrations of p53 mRNA (black), p53 (blue), Mdm2 mRNA (green) and Mdm2 (red) in (a) the nucleus and (b) the cytoplasm, for the extended p53-Mdm2 model in the absence of active transport. The period of oscillation is approximately* 242.5 *minutes. Parameter values as per column 2, Table 9.2.*

the protein reaches the nuclear membrane, but Figure 9.2 shows that microtubule-disrupting drugs may cause comparatively little of the protein to reach the nuclear membrane. Hence the effectiveness of drugs designed to act at nuclear pore complexes may be compromised by microtubule-disrupting drugs, and the combination of these two types of drug may not always represent an optimal treatment strategy.

Table 9.2 contains ranges of parameter values which permit oscillatory dynamics in the extended p53-Mdm2 model with no active transport. These ranges are narrower than those in Table 8.1 where there was no active transport and no explicit nuclear membrane, and are also narrower than the ranges in Table 9.1 where there was both active transport and an explicit nuclear membrane. These results are consistent with our findings for the Hes1 model in section 5.6. The parameter range for l now allows for protein translation to occur directly outside the nucleus. This is a result of the nuclear membrane slowing the entry of p53 to the nucleus, preventing Mdm2 levels from spiking too quickly.

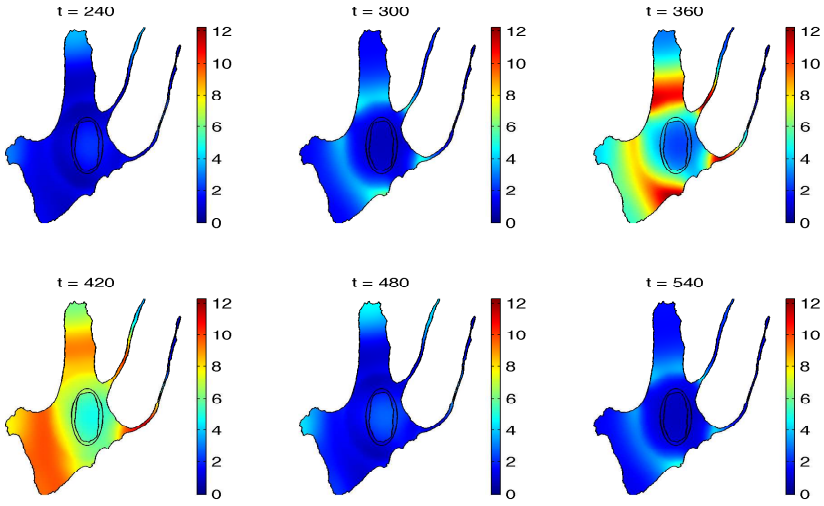

(a) *p53*

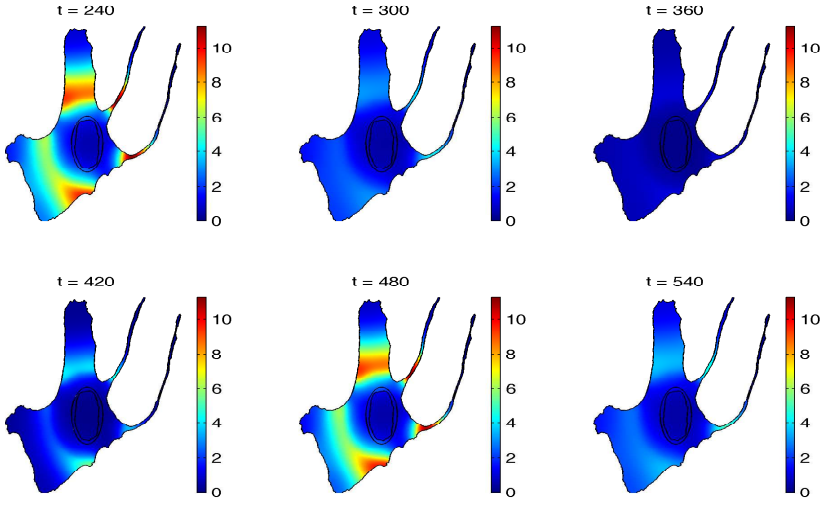

(b) *Mdm2*

Figure 9.4: *Plots showing the spatio-temporal evolution of (a) p53 and (b) Mdm2 within the osteosarcoma cell domain from times* $t = 240$ *to* $t = 540$ *minutes at* 60 *minute intervals, for the extended p53-Mdm2 model in the absence of active transport. The concentrations exhibit oscillatory dynamics in both time and space. Parameter values as per column 2, Table 9.2.*

Parameter	Value in simulations	Range over which oscillations are observed
D_{i_j}	$3.00\times10^{-11}\text{cm}^2\text{s}^{-1}$	$1.16\times10^{-11}\text{cm}^2\text{s}^{-1}$ to $5.00\times10^{-8}\text{cm}^2\text{s}^{-1}$
ζ	$2.92\times10^{-10}\text{Ms}^{-1}$	$\geq 5.83\times10^{-11}\text{Ms}^{-1}$
ϕ	$5.83\times10^{-4}\text{s}^{-1}$	$1.00\times10^{-4}\text{s}^{-1}$ to $1.03\times10^{-3}\text{s}^{-1}$
β	0.33s^{-1}	$\geq 0.06\text{s}^{-1}$
μ	$1.00\times10^{-4}\text{s}^{-1}$	$\leq 3.67\times10^{-4}\text{s}^{-1}$
ν	$3.33\times10^{-2}\text{s}^{-1}$	$1.33\times10^{-3}\text{s}^{-1}$ to 3.67s^{-1}
h_1	2	≥ 1
$\widehat{Mdm2}$	$3.2\times10^{-5}\text{M}$	$3.00\times10^{-6}\text{M}$ to $2.40\times10^{-4}\text{M}$
α	$2.92\times10^{-11}\text{Ms}^{-1}$	$\leq 2.33\times10^{-11}\text{Ms}^{-1}$
η	$1.67\times10^{-9}\text{Ms}^{-1}$	$\geq 2.17\times10^{-10}\text{Ms}^{-1}$
h_2	4	≥ 1
$\widehat{p53}$	$2.50\times10^{-6}\text{M}$	$\leq 1.35\times10^{-5}\text{M}$
θ	4.00	$\geq 1.60\times10^{-3}$
γ	0.67s^{-1}	$\geq 0.09\text{s}^{-1}$
ρ	$8.33\times10^{-4}\text{s}^{-1}$	$1.33\times10^{-4}\text{s}^{-1}$ to $6.67\times10^{-3}\text{s}^{-1}$
D_m	$6.00\times10^{-12}\text{cm}^2\text{s}^{-1}$	$\geq 1.50\times10^{-13}\text{cm}^2\text{s}^{-1}$
D_p	$2.00\times10^{-12}\text{cm}^2\text{s}^{-1}$	$\geq 2.50\times10^{-14}\text{cm}^2\text{s}^{-1}$
d	$1.00\times10^{-5}\text{cm}$	$\leq 2.00\times10^{-4}\text{cm}$
a	0	–
l	$6.32\mu\text{m}$	nuclear membrane (approx. 2 to 3μm) to 8.94μm

Table 9.2: *Parameter values used in the extended p53-Mdm2 model in the case where active transport rates are set to zero, and ranges over which sustained oscillatory dynamics are observed.*

9.5 Proteasome inhibition numerical experiment

We repeat here the proteasome inhibition numerical experiment which we performed on the reaction-diffusion model of the p53 GRN in section 8.5 for our extended p53-Mdm2 GRN model. In section 8.5, we noted that we were not able to reproduce the experiments conducted by Xirodimas et al. (2001), in which large levels of p53 and Mdm2 were recorded in the nucleus after treatment with proteasome inhibitor MG132. Following the same approach in section 8.5, we divide the protein degradation parameters, μ, ν, and ρ byλ, the inhibition factor. All other parameter values used for the simulations are as detailed in Table 9.1, but we divide μ, ν, and ρ by $\lambda = 300$ so that their values become those shown in equation (8.18). We do not reduce these protein degradation parameters to zero because proteasome inhibitors are not 100% efficient (Lightcap et al., 2000).

In Figure 9.5 we can see how the decrease in protein degradation parameters has affected the total concentrations of the variables in the p53-Mdm2 model including a

nuclear membrane and active transport. The system no longer exhibits oscillatory dynamics, but instead p53 and Mdm2 levels increase monotonically, quickly exceeding the levels in Figure 9.1 where there was no proteasome inhibition. We can now see the level of protein in the nucleus exceeds that of the cytoplasm. Furthermore, the protein levels in the cytoplasm are actually largely concentrated in the region between the nucleus and the MTOC, i.e., very close to the nucleus. This is reflected in the spatial plots presented in Figure 9.6, where we can see high local concentrations of p53 and Mdm2 in the nucleus at time t = 1500 minutes which accurately reflects the experimental findings of Xirodimas et al. (2001) and Maki et al. (1996). The reason p53 and Mdm2 accumulate in the nucleus is due to active transport directing both species towards the nucleus. Mdm2 levels rapidly increase because the degradation rate of Mdm2 protein is decreased. Notice that p53 levels also increase, but not as rapidly as Mdm2. As there is a higher concentration of Mdm2 in the cell, this increases the likelihood of p53 being degraded via Mdm2 (although ν has been decreased, it is not zero). Mdm2 mRNA levels remain low in spite of increased levels of p53 as a result of Mdm2 protein directly inhibiting p53 transcriptional activity. p53 mRNA levels are unaffected by this numerical experiment.

Combination chemotherapy was mentioned in section 9.4, and we noted that the combination of microtubule-disrupting drugs and drugs designed to act at nuclear pore complexes may not always represent an optimal treatment strategy. We can now add to this discussion. Figure 9.6 suggests that when proteins that are actively transported towards the nucleus are influenced by proteasome inhibitor drugs, their local concentration will rise significantly at the nuclear membrane. Hence the combination of drugs designed to act at nuclear pore complexes with proteasome inhibitor drugs may represent a potentially fruitful avenue for new chemotherapeutic experimental studies.

In Figure 9.7 we explore the relationship between the nuclear to cytoplasmic ratio of protein and the inhibition factor, λ. We achieved this by first calculating the total

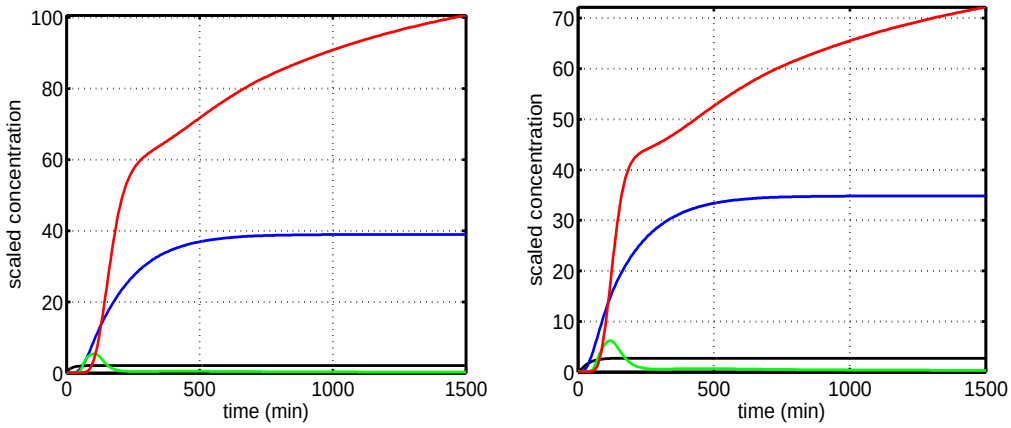

(a) *nuclear compartment* **(b)** *cytoplasmic compartment*

Figure 9.5: *Plots of the total concentrations of p53 mRNA (black), p53 (blue), Mdm2 mRNA (green) and Mdm2 (red) in (a) the nucleus and (b) the cytoplasm, for the extended p53-Mdm2 model. We also note that the proteins in the cytoplasm are largely concentrated in the region between the nucleus and the MTOC, i.e., very close to the nucleus, as can be seen in Figure 5.9. Parameter values as per column 2, Table 9.1, with the exception of parameters* μ*,* ν*, and* ρ *which are specified in equation* (8.18)*. The total concentrations of p53 and Mdm2 continue to increase over the* 1500 *minute time interval and accumulate mainly in the nuclear compartment.*

concentrations of nuclear and cytoplasmic protein over a 1500 minute time period for different values of λ. We then calculated the mean of these total concentrations and divided the nuclear mean by the cytoplasmic mean. Finally, we plotted this ratio against the value of λ. As can be seen from the plots, the nuclear to cytoplasmic ratio of p53 monotonically increases as λ is increased, whereas the nuclear to cytoplasmic ratio of Mdm2 saturates once λ reaches a value of approximately 150. From Figure 9.7, we can make the quantitative prediction that the proteasome inhibitor must effectively reduce the degradation rates by a factor of 200 before more p53 and Mdm2 will accumulate in the nucleus than in the cytoplasm.

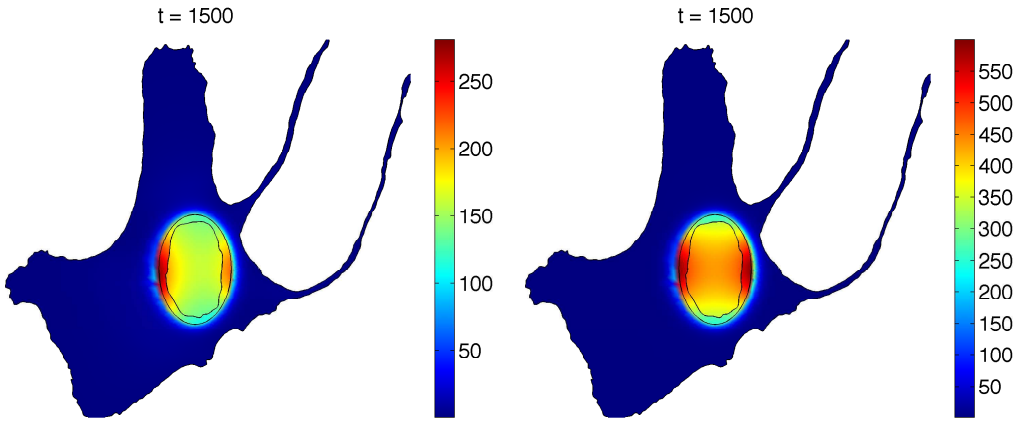

(a) *p53 concentration* **(b)** *Mdm2 concentration*

Figure 9.6: *Plots showing the spatial distribution of (a) p53 and (b) Mdm2 within the osteosarcoma cell domain at time* $t = 1500$ *minutes, for the extended p53-Mdm2 model. The concentrations of p53 and Mdm2 are localised mainly in the nucleus and between the nuclear membrane and the MTOC. Parameter values as per column 2, Table 9.1, with the exception of parameters* μ, ν, *and* ρ *which are specified in equation* (8.18).

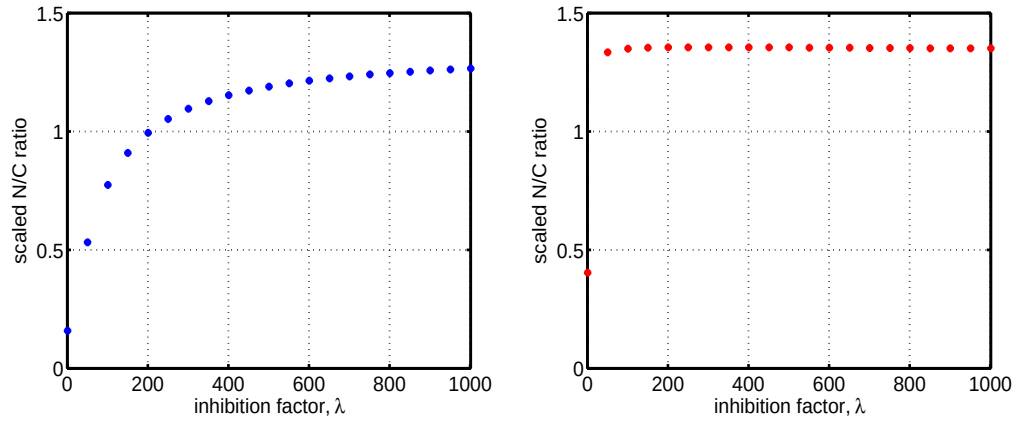

(a) *p53* **(b)** *Mdm2*

Figure 9.7: *Plots of the nuclear to cytoplasmic (N/C) ratio against the inhibition factor* λ *for (a) p53 and (b) Mdm2. Values of* λ *are plotted in increments of* 50, *starting with* 1 *and ending with* 1001. *Parameter values are found in column 2, Table 9.1, with the exception of parameters* μ, ν, *and* ρ *which are reduced by a factor* λ.

9.6 Discussion

In this chapter we have extended the spatio-temporal model of the p53-Mdm2 GRN presented in chapter 8. Our extensions consisted of introducing an explicit nuclear membrane and allowing active transport of proteins. We accounted for the permeability of the nuclear membrane by considering its thickness and the fact that diffusion across it is slower than in the nucleus or cytoplasm, and assumed that proteins were convected from the cytoplasm to the nucleus in order to model translocation along microtubules.

Experiments have shown that stimulation of the p53-Mdm2 GRN can cause p53 and Mdm2 concentrations to exhibit oscillatory dynamics, driven by a negative feedback loop. The concentrations oscillate with a period ranging from 3 to 7 hours (Bar-Or et al., 2000; Geva-Zatorsky et al., 2006), which our extended model was able to reproduce. Furthermore, we found ranges of values for the model parameters such that sustained oscillatory dynamics occurred, noting that these ranges were consistent with available experimental measurements. We also found that our model extensions acted to broaden the parameter ranges that yielded oscillations compared with the previous results of chapter 8. Hence oscillatory behaviour is made more robust by the inclusion of both the nuclear membrane and active transport.

In the interests of making accurate quantitative statements, we explored our extended p53-Mdm2 model on a domain that was imported from an image of an osteosarcoma cell — the p53 pathway is known to be deregulated in osteosarcomas. We were able to make quantitative observations regarding, for example, the proportion of p53 that enters the nucleus. In particular, we saw that peaks in total nuclear concentration were 33% the height of peaks in total cytoplasmic concentration, whereas this proportion was only 8% in the reaction-diffusion model. Hence, although the nuclear membrane acts as a barrier to p53 nuclear localisation, active transport nevertheless increases this localisation. Our quantitative data serve as predictions until accurate experimental

data become available. We made qualitative observations too, noting that our new p53-Mdm2 model exhibited pulsatile-like dynamics in keeping with several experimental studies (Batchelor et al., 2009; Loewer et al., 2010).

Motivated by experiments involving microtubule-disrupting chemotherapeutic drugs (Jordan and Wilson, 2004; Kavallaris, 2010; Carbonaro et al., 2011), we considered the special case in our new models where active transport rates were set to zero. We found that this narrowed the ranges of values for model parameters such that sustained oscillatory dynamics occurred. For our p53-Mdm2 model, we found reductions in the levels of nuclear p53 and nuclear Mdm2, in qualitative agreement with experimental data in Roth et al. (2007) and Giannakakou et al. (2000). We also considered the effect of proteasome inhibitor drugs in our p53-Mdm2 model by reducing protein degradation rates. This increased levels of p53 and Mdm2, especially in the nucleus, and again these results matched experimental data (Maki et al., 1996; Xirodimas et al., 2001). Hence, we were able to overcome the shortcomings of our reaction-diffusion model presented in chapter 8. The active transport modelling assumption is critical for our proteasome inhibition numerical experiment to reproduce real biological data. Ignoring our nuclear membrane assumption results in even larger quantities of p53 and Mdm2 accumulating in the nucleus (plots not shown).

From the spatial profiles for the p53-Mdm2 model, we observed that the nuclear membrane retards the nuclear entry of p53 and Mdm2, with the local concentrations of these species reaching their highest levels in or next to the nuclear membrane. Such results indicate that the nuclear pore complex is an attractive site for delivering chemotherapeutic drugs to disrupt or enhance intracellular signalling, as discussed in Gasiorowski and Dean (2003) and Chahine and Pierce (2009). Our spatial profiles also suggested that microtubule-disrupting drugs may cause comparatively little protein to reach the nuclear membrane whereas proteasome inhibitor drugs may increase protein levels both at the nuclear membrane and in the nucleus. We drew conclusions in terms of

combination chemotherapy, suggesting that the effectiveness of drugs designed to act at nuclear pore complexes may be limited by microtubule-disrupting drugs but enhanced by proteasome inhibitor drugs. Computational animations of our spatio-temporal simulations closely matched the experimental results of Lahav et al. (2004) where concentration profiles of proteins in single cells were imaged utilising fluorescent fusion proteins. With the continuing advance of imaging techniques in individual cells (Kherlopian et al., 2008; Michalet et al., 2005), it will become increasingly important to model intracellular dynamics using a spatio-temporal framework.

Chapter 10

Discussion and future directions

We conclude this thesis with a brief summary of the major points and some possible avenues of future exploration. Of course, this is by no means exhaustive, and we refer the reader to the appropriate chapters for a more detailed account.

10.1 Discussion

The primary message arising from the work presented in this thesis is that spatio-temporal modelling of gene regulatory networks is a valuable pursuit. Spatio-temporal modelling has significant advantages over more traditional temporal approaches — not only is it more faithful to the underlying biology but spatio-temporal simulations can be more readily compared with experimental data. Furthermore, the approach allows for more questions to be asked of the GRNs under study.

Results from previous mathematical models have reflected simplified experimental findings but have not distinguished explicitly between spatial compartments within the cell and have not considered (explicit) spatial movement of molecules. We have

developed novel spatio-temporal models of two well characterised GRNs: the Hes1 GRN and the p53-Mdm2 GRN. The Hes1 GRN plays a role in somitogenesis and embryonic stem cell differentiation, whereas the p53-Mdm2 GRN is critical for regulating the cell-cycle. Both are implicated in human cancer and have been the subject of intensive research over the past decade. This research has been conducted via two parallel (complementary) streams: biological experimentation and mathematical modelling.

Building on directly from previous DDE models, we formulated equivalent PDE models on cell-like domains with separate nuclear and cytoplasmic compartments (with reactions localised appropriately). In general, we solved the models numerically using the finite element method as implemented in the software package COMSOL 3.5a, using triangular basis elements and Lagrange quadratic basis functions along with a backward Euler time-stepping method of integration. We chose the finite element method due to its ability to handle complicated geometries (the eukaryotic cell usually takes an irregular shape) and boundaries with relative ease. The numerical simulation results of our spatio-temporal reaction-diffusion models (presented in chapters 4 and 8) have demonstrated the existence of oscillatory dynamics in negative feedback systems both for relatively simple (Hes1) and more complex (p53-Mdm2) GRNs and have been able to focus on reactions occurring both in the cell nucleus and in the cytoplasm. The use of PDEs allows spatial effects to be examined explicitly and facilitates the study of how protein localisation is regulated. In chapter 4 we investigated the effect of spatial dimension on the Hes1 GRN, something that can only be done using a spatial model. We found that for 1D, 2D, and 3D simulations our model yielded qualitatively similar results and quantitatively similar results for 2D and 3D simulations.

In chapters 5 and 9 we extended our reaction-diffusion models by including a nuclear membrane and active transport. We accounted for the permeability of the nuclear membrane by considering its thickness and the fact that diffusion across it is slower than in the nucleus or cytoplasm, and we assumed that proteins were convected from the

cytoplasm to the nucleus in order to model translocation along microtubules. The extended models were able to produce sustained oscillations with periods consistent with experimental data (Hirata et al., 2002; Bar-Or et al., 2000; Geva-Zatorsky et al., 2006). We found ranges of values for the model parameters such that sustained oscillatory dynamics occurred, noting that these ranges were consistent with available experimental measurements. We also found that our model extensions acted to broaden the parameter ranges that yielded oscillations compared with the reaction-diffusion models. Hence oscillatory behaviour is made more robust by the inclusion of both the nuclear membrane and active transport.

Given that cell shape can influence intracellular signalling (Meyers et al., 2006; Neves et al., 2008), we investigated the influence on the numerical simulations of varying the cell domain, finding for our extended Hes1 model that oscillatory dynamics are strongly robust to changes in the size and shape of the cell and its nucleus. In general we found that qualitative dynamics were unaffected by varying the cell shape but quantitative dynamics were affected quite substantially. Hence, in the interests of making accurate quantitative statements, we explored our extended p53-Mdm2 model on a domain that was imported from a high resolution microscopy image of an osteosarcoma cell — the p53-Mdm2 pathway is known to be deregulated in osteosarcomas.

Motivated by experiments involving microtubule-disrupting chemotherapeutic drugs, we considered the special case in our extended models where active transport rates were set to zero. Strikingly, we found that this experiment had major implications for the extended Hes1 GRN model. The numerical simulations displayed a qualitative change — damped oscillations were now observed. Unfortunately, we can not corroborate our findings with experimental data in this case, but instead leave this numerical experiment as a prediction of the model. For our p53-Mdm2 extended model, we found reductions in the levels of nuclear p53 and nuclear Mdm2, in qualitative agreement with experimental data. We found that this narrowed the ranges of values

for model parameters such that sustained oscillatory dynamics occurred.

We also investigated the influence of proteasome inhibitors on both the p53-Mdm2 and Hes1 GRNs. We achieved this by decreasing the protein degradation parameters in our models. In each case, interesting biological insights were gained. For the case of the Hes1 GRN, both of our reaction-diffusion (chapter 4) and extended model (chapter 5) were able to reflect temporal data regarding the how the concentration of Hes1 protein changed once the cell was treated with a proteasome inhibitor. Given the spatial nature of our models, we were also able to make predictions about how proteasome inhibition influenced the spatial distribution of Hes1 proteins. We left our spatial distribution plots as predictions of the model. Importantly, the reaction-diffusion model with continuity of flux boundary conditions yields different spatial distributions to the extended model. Hence, once corroborated with experimental evidence, we will be able to find out which model is more accurate and gain an insight into how transport of Hes1 protein is regulated. For the case of p53-Mdm2, experimental evidence of how p53 and Mdm2 localise following proteasome inhibition is available. We found that our reaction-diffusion model fell short of reproducing the experimental data but that our extended model succeeded. Furthermore, for the Hes1 GRN we investigated the influence of translation inhibitors. Here, we were able to reproduce temporal data concerning the total concentrations of hes1 mRNA and Hes1 protein in the cell. In this case, the spatial distributions for both the reaction-diffusion model and extended model were consistent.

Encouraged by the results from our PDE approach, we formulated an equivalent stochastic reaction-diffusion model of the Hes1 GRN in chapter 6. In our spatial stochastic model, all reactions are modelled using elementary mass action kinetics. This is in contrast to all previous modelling efforts where a Hill function approximation was used for Hes1 binding to the promoter site. Since our model is explicitly spatial, such an approach is neither appropriate nor necessary.

We computed trajectories of the reaction-diffusion master equation using a spatially extended Gillespie algorithm (the next subvolume method) as implemented in URDME (Drawert et al., 2012). We estimated the period of our model trajectories using a continuous time wavelet transform (as implemented in WAVOS, a MATLAB toolbox).

In the case of the Hes1 GRN, in contrast to our PDE models, our spatial stochastic model is able to reproduce the variability in period and amplitude of Hes1 oscillations observed in experiments. As a result of this, we have stated that intrinsic noise can explain heterogeneity in ES cell differentiation (see chapter 6 for details). We also showed our model was robust to parameter changes through various parameter sweeps. We were able to ask more questions of our model than recent stochastic DDE models, as well as being able to directly compare our numerical simulations with bioluminescence movies of *in vivo* Hes1 expression.

As there is potential application for regenerative medicine, we have also proposed methods of controlling differentiation responses via drug treatment. Our model has predicted that applying proteasome inhibitors to an ES cell could yield a mesodermal cell while applying translation inhibitors could yield a neuronal cell. Our model was also able to reproduce experimental results in which hes1 transgenes were introduced to hematopoietic progenitor cell which encoded a mutant Hes1 protein lacking the DNA-binding domain (Yu et al., 2006).

Computational animations of our spatio-temporal simulations closely matched the experimental results of Geva-Zatorsky et al. (2010) and Kobayashi et al. (2009) where concentration profiles of proteins in single cells were imaged utilising fluorescent fusion proteins. With the continuing advance of imaging techniques in individual cells, it will become increasingly important to model intracellular dynamics using a spatio-temporal framework.

10.2 Future directions

The work we have presented in this thesis has merely 'scratched the surface' of what can be done with spatio-temporal modelling of GRNs. Future work will consider extending the models further in several ways, as well as performing detailed analysis of the current models.

10.2.1 Partial differential equation models

We are currently undertaking a nonlinear analysis of the Hes1 reaction-diffusion model which has led to the study of a nonlinear and nonlocal eigenvalue problem. Cells can change shape on the same timescale as oscillatory nuclear-cytoplasmic translocation of Hes1 or p53, and so we may develop a model with a moving boundary on an evolving domain. Based on cell imagery, we will consider more realistic support functions for our translation and active transport terms. We may also study the interactions between different signalling pathways, i.e., "cross-talk". For example, it is known that the p53-Mdm2 GRN can co-operate with and antagonise the NF-κB GRN, which is central to many stressful, inflammatory, and innate immune responses (Pommier et al., 2004; Perkins, 2007). We are not aware of any spatio-temporal modelling studies of interacting GRNs, though there have been temporal studies (Puszyński et al., 2009). Our p53-Mdm2 model is based on a reduced description of the GRN, and we may explore the consequences of including more reactions and species in the model. We may also explore the effect of different chemotherapeutic drugs on the Hes1 and p53-Mdm2 GRNs. One aspect of intracellular dynamics which we have not included in our current models, but which is of relevance to our studies, is that of molecular crowding, i.e., volume exclusion events due to other molecules or organelles. Molecular crowding generates an environment where diffusion is hindered by obstacles and traps, resulting

in a form of molecular movement called “anomalous diffusion” (Mendez et al., 2010). Anomalous diffusion refers to a form of molecular movement in which the mean-square displacement of a molecule is not linear in time and this kind of movement has been observed in many experimental studies (Weiss et al., 2004; Wachsmuth et al., 2000; Caspi et al., 2000). In order to account for molecular crowding in mathematical models, numerous different approaches have been taken. In deterministic models, fractional partial differential equations have been employed with success in simplified settings but have proved challenging in more realistic settings (Yadav et al., 2008). Many authors have taken a spatial stochastic approach to account for macromolecular crowding, and numerical studies have proven more tractable than in the deterministic case — for a recent example, see Marquez-Lago et al. (2012). Hence, in the future we may explore the influence of anomalous diffusion on both our PDE and spatial stochastic models of GRNs.

10.2.2 Spatial stochastic Hes1 gene regulatory network model

Future work will consider extending the Hes1 spatial stochastic model in various ways. In particular, we will explicitly account for transport across the nuclear membrane and dimerisation of Hes1 monomers. We aim to use our spatio-temporal modelling approach to shed light on the localisation of the Hes1 dimerisation reaction. This reaction has been identified as a possible target for cancer treatment (Sang et al., 2010). As mentioned in chapter 6, we will also conduct a global parameter sensitivity analysis of our model using data clustering techniques. We may also consider cell-cell communication in future work to see if this acts to stabilise and synchronise oscillatory behaviour as was found experimentally in Masamizu et al. (2006) and in a mathematical model of Notch signalling in Terry et al. (2011).

10.2.3 Spatial stochastic p53-Mdm2 gene regulatory network model

We are currently formulating and exploring a spatial stochastic model of the p53-Mdm2 GRN. Preliminary results are encouraging and we present 4 trajectories in Figure 10.1 which display the total copy number of p53 (red) and Mdm2 (blue). This Figure bears a striking resemblance to the corresponding experimental data, see Figure 2 in Geva-Zatorsky et al. (2010). Using a spatial stochastic approach makes it possible to replicate the noisy oscillatory dynamic displayed in the experimental data. In addition, we also present a plot (Figure 10.2) showing how the spatio-temporal evolution of a sample trajectory evolves. This plot also agrees well with the equivalent experimental Figure (see Figure 1 of Geva-Zatorsky et al. (2010)).

Once we have thoroughly examined a spatial stochastic model of the p53-Mdm2 GRN, we plan to extend it in various ways. Some examples include accounting for dimerisation and tetramerisation of p53, active transport of p53 along microtubules and modelling transport across the nuclear membrane in greater detail. The spatial-stochastic p53-Mdm2 model can be adapted to study possible mutations or potential drug treatments by simply changing parameter sets. Using this approach, comparisons of mutant and wild-type cells under a range of drug treatment combinations is also possible.

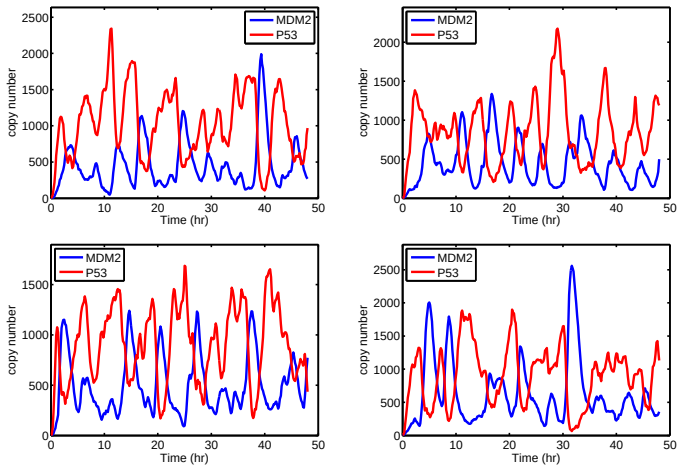

Figure 10.1: *Four trajectories from preliminary simulations of our spatial stochastic p53 GRN model. Plots show how the copy number of p53 (red) and Mdm2 (blue) evolve over a 50 hour time period.*

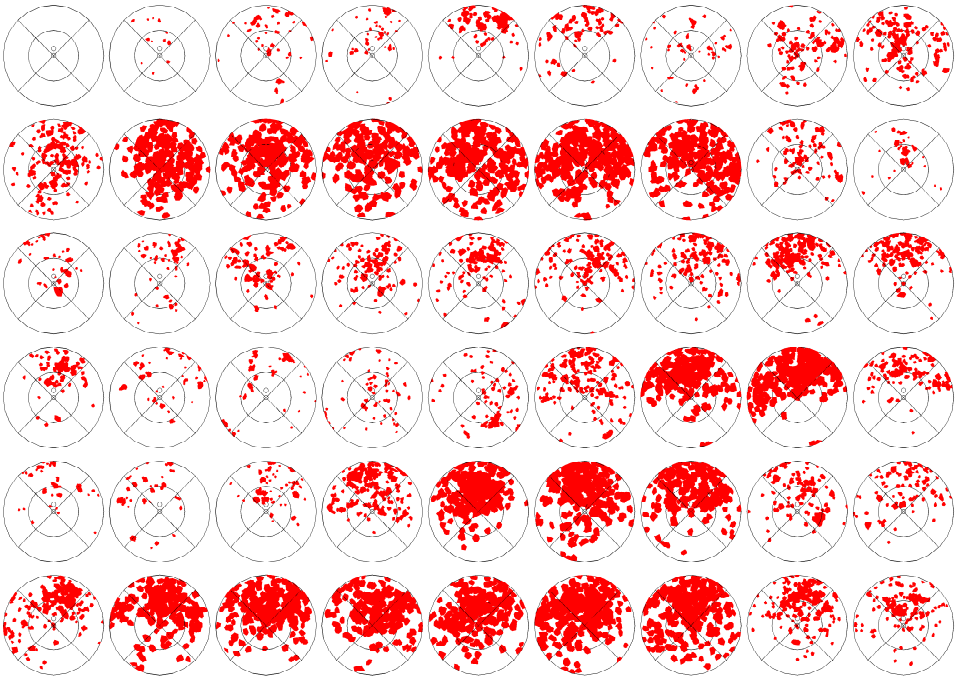

Figure 10.2: *Spatial snapshots of p53 protein distributions from preliminary simulations of our spatial stochastic model. Time between sequential frames is 20 minutes.*

Chapter 11

Appendix

11.1 Protein translation and synthesis in the cytoplasm: consideration of the location of the endoplasmic reticulum

The endoplasmic reticulum (ER) is a network of flattened sacs and branching tubules that extends throughout the cytoplasm in eukaryotic cells. These sacs and tubules are all interconnected by a single continuous membrane so that the organelle has only one large and intricately arranged lumen. The ER is divided into two distinct zones, the rough ER and the smooth ER. The surface of the rough ER is embedded with many ribosomes giving it a 'rough' appearance (hence its name). The rough ER is involved in the synthesis of proteins and is also a membrane factory for the cell, while the smooth ER is involved in the metabolising of carbohydrates, regulation of calcium concentration and the synthesis of lipids. The proteins made in the ER are either exported to the exterior of the cell or are transported to other membrane structures such as the Golgi apparatus, lysosomes and endosomes (Alberts et al., 2008). Thus proteins made in the

endoplasmic reticulum are unlikely to translocate to the nucleus.

In our PDE models of the Hes1 and p53 GRNs, we have made allowance for the endoplasmic reticulum by assuming that proteins made in the cytoplasm are translated a certain radial distance outside the nucleus. Beyond this radial distance, we have assumed that free-floating ribosomes are found in sufficient abundance and distributed homogeneously so that a step-function is suitable to account for their presence (see equation 4.5). This is not unreasonable to assume as depending on the protein production level of a particular cell, ribosomes may number in the millions (Alberts et al., 2008). The Heaviside function $H(x,y)$ states that in a region close to the nucleus (representing the location of the ER), the function is zero, meaning there is no protein synthesis in this region. In a region further away from the nucleus (outside the ER) the function takes the value of one, representing the region of the cytoplasm where we allow the translation of protein to occur. The Heaviside function is illustrated graphically in Figure 11.1.

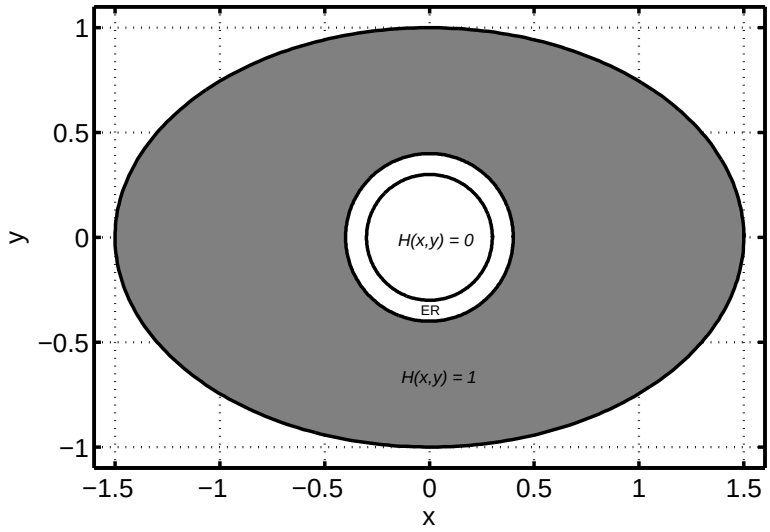

Figure 11.1: *A schematic representation of equation 4.5. The grey region of the cytoplasm depicts where we allow constant protein synthesis to occur, representing the region where the Heaviside function $H(x,y) = 1$. The white regions represent the nucleus and ER, where the Heaviside function $H(x,y) = 0$ (no protein synthesis takes place). The ER has a major axis of length $\sqrt{2}$ units and minor axis of length 1 unit.*

11.2 The Hes1 gene regulatory network

11.2.1 Dulac's criterion

We state here Dulac's criterion for proving the non-existence of periodic orbits in some regions of the phase space. We begin by recalling that if ∂A is a simple closed curve with outward normal n enclosing a region A and $\mathbf{f} : \mathbb{R}^2 \to \mathbb{R}^2$ is a continuously differentiable vector field and $\mathbf{g} : \mathbb{R}^2 \to \mathbb{R}$ is a continuously differentiable function then the divergence theorem of the plane states that

$$\oint_{\partial A} \mathbf{g}(\mathbf{f} \cdot \mathbf{n})\, dr = \iint_A \nabla \cdot (\mathbf{gf})\, dxdy,$$

where **gf** is a vector, $\mathbf{g}(x,y)\mathbf{f}(x,y)$, and is not to be confused with the composition of **g** and **f** (i.e., $\mathbf{g} \circ \mathbf{f}$).

Theorem 1. *If there exists a continuously differentiable function* $\mathbf{g} : \mathbb{R}^2 \to \mathbb{R}$ *such that* $\nabla \cdot (\mathbf{gf})$ *is continuous and non-zero on some simply connected domain D, then no periodic orbit can lie entirely in D.*

Proof. Suppose a periodic orbit ∂A does lie entirely in *D*. Then

$$\iint_A \nabla \cdot (\mathbf{gf})\, dxdy \neq 0,$$

where A is the area bounded by ∂A, since $\nabla \cdot (\mathbf{gf})$ is either strictly greater than zero or strictly less than zero throughout A. However, a periodic orbit is a trajectory, and hence tangential to the vector field, **f**. So, $\mathbf{f} \cdot \mathbf{n} = 0$, where **n** is the outward normal to the periodic orbit. Hence,

$$\oint_{\partial A} \mathbf{g}(\mathbf{f} \cdot \mathbf{n})\, dr = 0,$$

producing a contradiction by the divergence theorem. □

If $\mathbf{g} = 1$ then this result is sometimes referred to as Bendixson's criterion. Hence, in section 3.3.2 it could be said that we applied Bendixson's criterion to rule out periodic solutions in the Hes1 ODE model.

11.2.2 Non-dimensionalisation of reaction-diffusion models

We summarise our non-dimensionalisation of the Hes1 reaction-diffusion models (described in sections 4.2 and 5.2). To non-dimensionalise the extended Hes1 model given by equations (4.1) – (4.4) and (5.5), subject to the conditions in equations (4.8) – (5.4),

we first define re-scaled variables by dividing each variable by a reference value. Re-scaled variables are given overlines to distinguish them from variables that are not re-scaled. Thus we can write:

$$[\overline{m}_n] = \frac{[m_n]}{[m_0]}, [\overline{m}_c] = \frac{[m_c]}{[m_0]}, [\overline{p}_n] = \frac{[p_n]}{[p_0]}, [\overline{p}_c] = \frac{[p_c]}{[p_0]}, \overline{t} = \frac{t}{\tau}, \overline{x} = \frac{x}{L}, \overline{y} = \frac{y}{L}, \qquad (11.1)$$

where the right hand side of each equation is a dimensional variable divided by its reference value. From equation (11.1), we can write variables in terms of re-scaled variables and then substitute these expressions into equations (4.1) – (4.4) and (5.5), and into the conditions in equations (4.8) – (5.4). This gives a model defined in terms of re-scaled variables which has the same form as the dimensional model but now the parameters are all non-dimensional. Denoting the non-dimensional parameters with an asterisk, they are related to dimensional parameters as follows:

$$D^*_{i_j} = \frac{\tau D_{i_j}}{L^2}, \alpha^*_m = \frac{\tau \alpha_m}{[m_0]}, p^* = \frac{[p_0]}{\hat{p}}, \mu^*_m = \tau \mu_m, \alpha^*_p = \frac{\tau [m_0] \alpha_p}{[p_0]},$$
$$\mu^*_p = \tau \mu_p, D^*_m = \frac{\tau D_m}{L^2}, D^*_p = \frac{\tau D_p}{L^2}, d^* = \frac{d}{L}, a^* = \frac{\tau a}{L}, l^* = \frac{l}{L}. \qquad (11.2)$$

We solve the non-dimensional model using the method described in section 4.3. We simulate the model in COMSOL 3.5a, finding non-dimensional parameter values that yield oscillatory dynamics. We chose the same values as in equation (25) in Sturrock et al. (2011) except for those parameters which were new because of our extension to the model. These latter values were chosen as follows: $D^*_m = D^*_{i_j}/5$, $D^*_p = D^*_{i_j}/15$, $d^* = 0.01$, $a^* = 0.03$, $l^* = 0.63$.

Finally, we calculated the dimensional parameter values. To do this, we needed to estimate the reference values. Since Her1 in zebrafish and Hes1 in mice are both pathways connected with somitogenesis, we used the reference concentrations for Her1 protein and her1 mRNA in Terry et al. (2011) as our reference concentrations for Hes1 protein

and hes1 mRNA. Thus, we chose $[m_0] = 1.5 \times 10^{-9}$M and $[p_0] = 10^{-9}$M. We assumed a cell to be of width 30μm. But from Figures 4.1 and 5.2, the cell width is equal to 3 non-dimensional spatial units or $3L$ dimensional units (using equation (11.1)). Hence we set $3L = 30\mu$m, so that $L = 10\mu$m. The experimentally observed period of oscillations of Hes1 is approximately 2 hours (Hirata et al., 2002). Our simulations of the non-dimensionalised model gave oscillations with a period of approximately 300 non-dimensional time units or 300τ dimensional units (using equation (11.1)). Hence we set $300\tau = 2$ hours $= 7200$ seconds, so that $\tau = 24$ seconds. Using our references values and non-dimensional parameter values, we found dimensional parameter values from equation (11.2).

Note that we chose our reference time $\tau = 24$ seconds based on simulations of the extended Hes1 model since this was our most realistic Hes1 model. For the original Hes1 model and for all special cases of the Hes1 model (for example, setting active transport rates to zero), we retained the reference time $\tau = 24$ seconds.

11.2.3 Parameter sweeps of spatial stochastic model

In this section we present parameters sweeps for the remaining parameters in the spatial stochastic model which we did not discuss in section 6.4. The parameters α_m (the rate of transcription) and α_p (the rate of translation) do not influence the mean period distribution when varied (see Figures 11.2 and 11.4). Figure 11.3 reveals that provided the scale of transcription repression (γ) is greater than or equal to 12, a broad range of mean periods are found. The degradation parameters (μ_m and μ_p) permit broad mean period distributions for a range of parameter values (shown in Figures 11.5 and 11.6). If the degradation rates are too high or too low, the broad mean period distribution is lost.

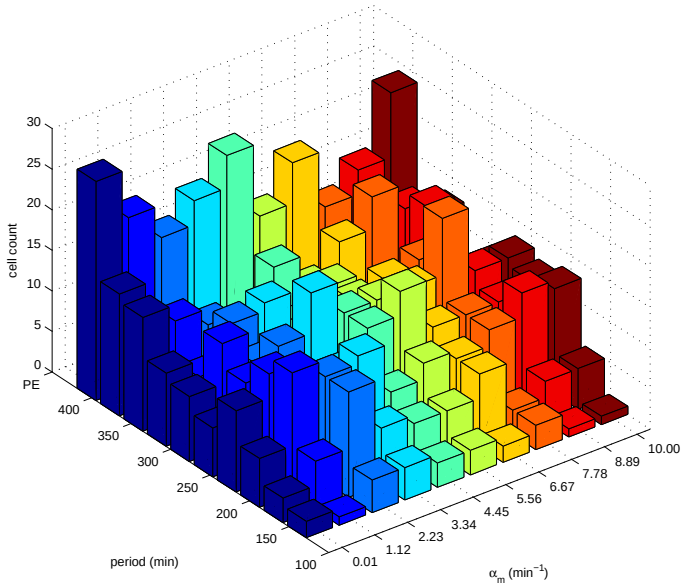

Figure 11.2: *Histogram plot showing the effect on the period of oscillations of changing the parameter α_m, the basal transcription rate of hes1 mRNA.* 10 *values of α_m were chosen from the range* $(0.01 - 10)\,\text{min}^{-1}$ *were chosen, and* 100 *trajectories for each different value were recorded. All other parameters in the model (see column 4, Table 6.1) were held constant. The mean periods were computed and divided into 'bins' varying from* 150 *mins to persistent expression (PE) i.e. greater than* 400 *mins. It is clear that α_m is robust to change, with no significant changes in the mean periods observed when the parameter is varied.*

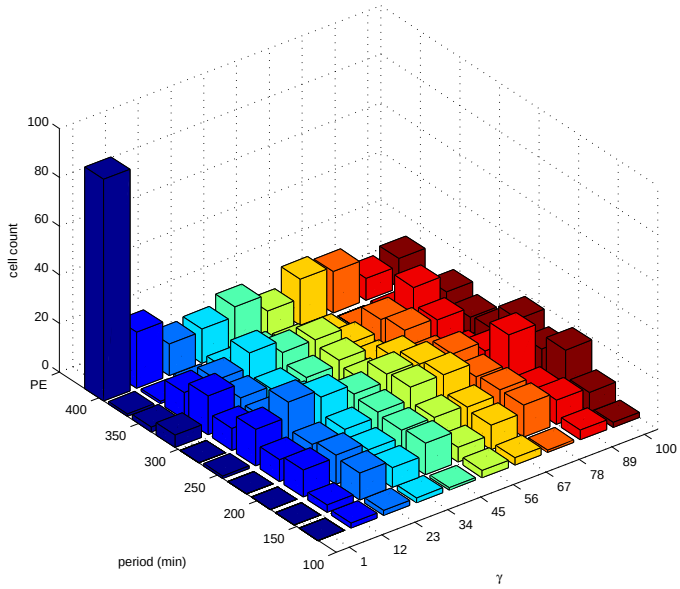

Figure 11.3: *Histogram plot showing the effect on the period of oscillations of changing the parameter γ, the scale of transcriptional repression.* 10 *values of γ were chosen from the range* $(1-100)$ *were chosen, and* 100 *trajectories for each different value were recorded. All other parameters in the model (see column 4, Table 6.1) were held constant. The mean periods were computed and divided into 'bins' varying from* 150 *mins to persistent expression (PE) i.e. greater than* 400 *mins. As may be expected, if γ is too small (corresponding to no or little negative feedback) no oscillations are observed and almost all trajectories exhibit persistent expression. Provided γ is greater than or equal to* 12 *we find that this parameter is robust to change, with a broad range of periods found for each different value of γ.*

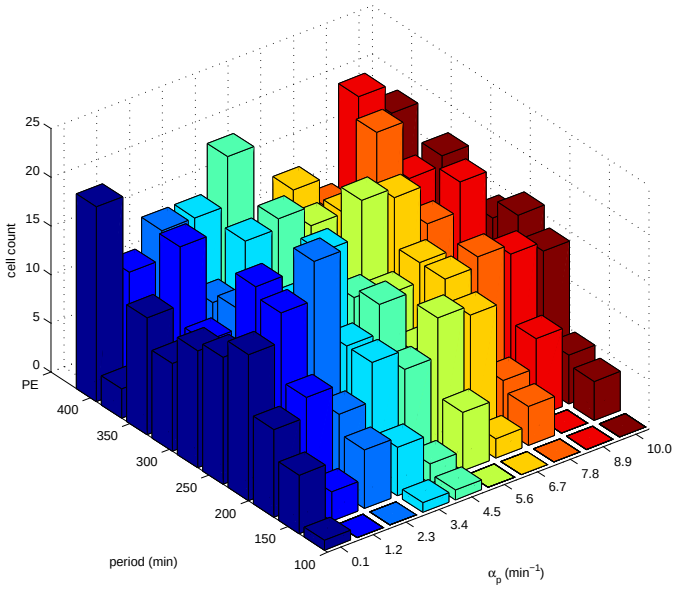

Figure 11.4: *Histogram plot showing the effect on the period of oscillations of changing the parameter α_p, the basal translation rate of hes1 mRNA.* 10 *values of α_p from the range* $(0.1 - 10)\,\mathrm{min}^{-1}$ *were chosen, and* 100 *trajectories for each different value were recorded. All other parameters in the model (see column 4, Table 6.1) were held constant. The mean periods were computed and divided into 'bins' varying from* 100 *mins to persistent expression (PE) i.e. greater than* 400 *mins. It is clear that α_p is robust to change, with no significant changes in the mean periods observed when the parameter is varied.*

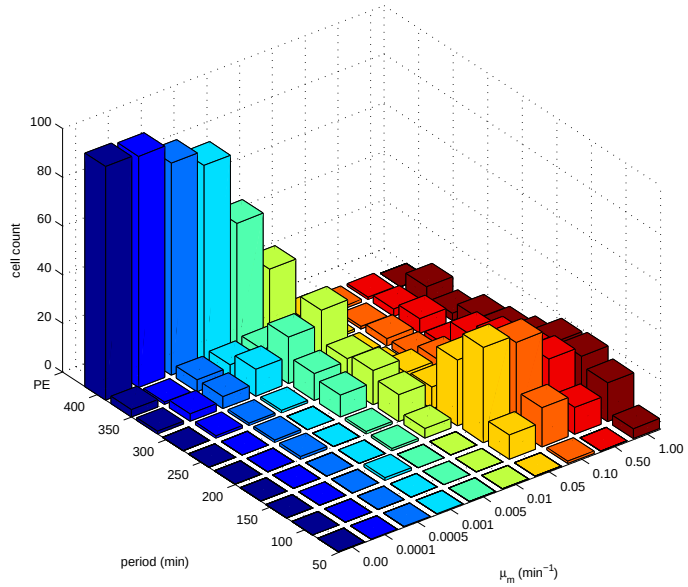

Figure 11.5: *Histogram plot showing the effect on the period of oscillations of changing the parameter μ_m, the degradation rate of hes1 mRNA.* 10 *values of μ_m from the range* $(0-1.0)\,\mathrm{min}^{-1}$ *were chosen, and* 100 *trajectories for each different value were recorded. All other parameters in the model (see column 4, Table 6.1)) were held constant. The mean periods were computed and divided into 'bins' varying from 100 mins to persistent expression (PE) i.e. greater than* 400 *mins. Low values of μ_m result in huge quantities of hes1 mRNA and subsequently Hes1 protein in the cell. Hence, it is not surprising that low values of μ_m result in persistent expression of Hes1. As μ_m is increased, we can see how the distribution of periods changes. We find that for larger values of μ_m many mean periods are found in the short period bins (*100 *to* 200 *mins). Only for $\mu_m = 0.01$ do we find a broad range of mean periods.*

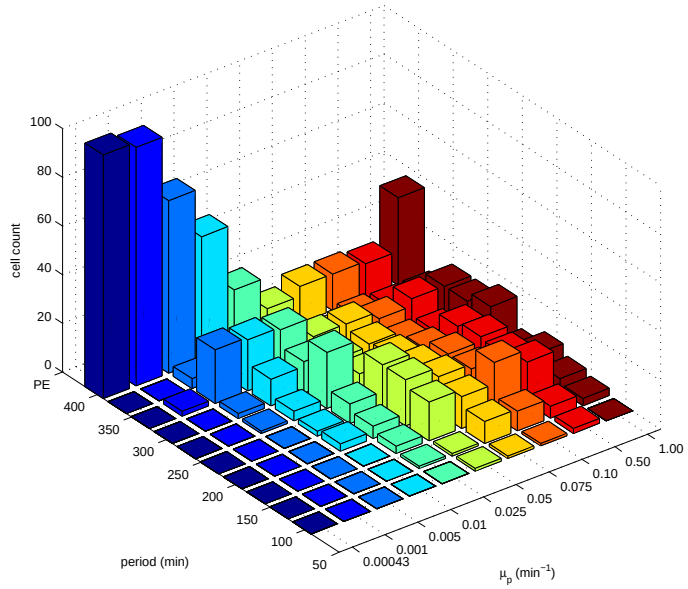

Figure 11.6: *Histogram plot showing the effect on the period of oscillations of changing the parameter μ_p, the degradation rate of Hes1 protein.* 10 *values of μ_p from the range* $(0.00043 - 1.0)\,\mathrm{min}^{-1}$ *were chosen, and* 100 *trajectories for each different value were recorded. All other parameters in the model (see column 4, Table 6.1) were held constant. The mean periods were computed and divided into 'bins' varying from* 100 *mins to persistent expression (PE) i.e. greater than* 400 *mins. Low values of μ_p result in huge quantities of Hes1 protein present in the cell. Hence, it is not surprising that low values results in most mean periods being placed in the PE bin. As μ_p is increased, fewer mean periods are found to exhibit persistent expression. We find that μ_p is relatively robust to change, with broad ranges of mean periods recorded, provided it takes a value greater than or equal to* $0.025\mathrm{min}^{-1}$.

11.3 The p53-Mdm2 gene regulatory network

11.3.1 Busenberg's criterion

We present here an extension of Dulac's criterion to systems in $\mathbb{R}^3$ as appears in Busenberg and Driessche (1990). This criterion is used for ruling out periodic solutions to ordinary differential equation systems. We applied it to system of equations (7.1) – (7.3), which models the p53-Mdm2 GRN.

Theorem 2. *Let* $\mathbf{f}: \mathbb{R}^3 \to \mathbb{R}^3$ *be a Lipschitz continuous vector field and let* $\gamma(t)$ *be a closed, piecewise smooth, curve which is the boundary of an orientable smooth surface* $S \subset \mathbb{R}^3$. *Suppose that* $\mathbf{g}: \mathbb{R}^3 \to \mathbb{R}^3$ *is defined and piecewise smooth in a neighbourhood of S, and that it satisfies*

$$\mathbf{g}(\gamma(t)) \cdot \mathbf{f}(\gamma(t)) \leq 0 \ (or \geq 0) \text{ for all } t, \tag{11.3}$$

$$(\nabla \times \mathbf{g}) \cdot \mathbf{n} \geq 0 \ (\leq 0) \text{ on } S, \text{ and } (\nabla \times \mathbf{g}) \cdot \mathbf{n} > 0 \ (< 0) \text{ for some point on } S, \tag{11.4}$$

where $\mathbf{n}$ *is the unit normal to S. Then* $\gamma(t)$ *is not the finite union of solution trajectories of*

$$\mathbf{x}'(t) = \mathbf{f}(\mathbf{x}(t)) \tag{11.5}$$

which are traversed in the positive sense relative to the direction of $\mathbf{n}$.

Proof. We first note that γ(t) is an orbit of solutions of (11.5) if, and only if, it is an orbit of the system $\mathbf{x}'(t) = -\mathbf{f}(\mathbf{x}(t))$, which is traversed in the opposite direction. Thus, the two sets of inequalities in (11.3) and (11.4) are equivalent, and we give the proof only for the first set. By (11.4) and using Stokes' theorem we have:

$$0 < \iint_S (\nabla \times \mathbf{g}) \cdot \mathbf{n} \, dA = \int_\gamma \mathbf{g}(\gamma(t)) \cdot \gamma'(t) \, dt. \tag{11.6}$$

Now, if $\gamma(t)$ is piecewise smooth with $\gamma'(t) = \mathbf{f}(\gamma(t))$, except for a finite number of points, then from (11.3)

$$\int_\gamma \mathbf{g}(\gamma(t)) \cdot \gamma'(t)\, dt = \int_\gamma \mathbf{g}(\gamma(t)) \cdot \mathbf{f}(\gamma(t))\, dt \leq 0.$$

This contradicts (11.6) and the theorem is proved. □

An immediate corollary of this theorem yields the criterion that we used in the proof that the p53-Mdm2 system (given by equations (7.1) – (7.3)) can not produce periodic solutions.

Corollary 1. *Let $S \subset \mathbb{R}^3$ be a smooth, orientable surface such that any piecewise smooth closed curve $\gamma(t) \in S$ is the boundary of a surface $S' \subset S$. If $\gamma : \mathbb{R}^3 \to \mathbb{R}^3$ is smooth, $\mathbf{f} : \gamma(t) \to \mathbb{R}^3$ is Lipschitz, and* **f** *and* **g** *satisfy*

$$\mathbf{g}(\gamma(t)) \cdot \mathbf{f}(\gamma(t)) = 0, \tag{11.7}$$

and

$$(\nabla \times \mathbf{g}) \cdot \mathbf{n} > 0 \text{ on } S \ (< 0 \text{ on } S), \tag{11.8}$$

where **n** *is the unit normal to S, then $\gamma(t)$ is not a phase polygon of the differential equation $\mathbf{x}'(t) = \mathbf{f}(\mathbf{x}(t))$.*

Proof. If γ(t) was a phase polygon of $\mathbf{x}'(t) = \mathbf{f}(\mathbf{x}(t))$, then $\{\gamma(\text{t}), \text{t} \geq 0\} = \partial S'$ for some oriented smooth surface $S' \subset$ S when γ is a given positive orientation relative to the normal **n** to S. Now, apply Theorem 2 to γ(t) and S' to see that this is not possible. □

It is easy to see that this corollary generalises Dulac's criterion (presented in section 11.2.1). In fact, if

$$x' = f_1(x,y),$$
$$y' = f_2(x,y),$$

is a planar system, we extend it trivially to $\mathbb{R}^3$ by

$$\begin{aligned} x' &= f_1(x,y), \\ y' &= f_2(x,y), \\ z' &= 0, \end{aligned}$$

and we choose $\mathbf{g}(x,y)$ = (-$f_2(x,y)$, $f_1(x,y)$,0). Then $\mathbf{g}(x,y) \cdot (f_1(x,y), f_2(x,y), 0) = 0$, and letting S be the x, y plane, we have **n** = (0,0,1). Assuming $f_1(x,y)$ and $f_2(x,y)$ are smooth, we have $(\nabla \times \mathbf{g}) \cdot \mathbf{n} = \nabla \cdot (f_1(x,y), f_2(x,y)) > 0$ ($<$0), in this special case of Corollary 1.

We note that both Theorem 1 and Corollary 1 do not require that the field **f** be smooth or even differentiable. In fact, even the Lipschitz condition on **f**, which implies that **f** is differentiable almost everywhere, can be replaced by requiring that **f** be continuous and that the problem $\mathbf{x}'(t) = \mathbf{f}(\mathbf{x}(t))$, $\mathbf{x}(0) = x_0$, has a unique solution.

11.3.2 Non-dimensionalisation of reaction-diffusion models

We non-dimensionalised the p53-Mdm2 model defined in section 8.2, and the extended p53-Mdm2 model defined in section 9.2, using the technique described above for non-dimensionalising the extended Hes1 model. We present here brief details of our non-dimensionalisation of the extended p53-Mdm2 model.

To non-dimensionalise the extended p53-Mdm2 model given by equations (8.1) – (8.8) and (9.9) – (9.10) subject to conditions (8.9), (8.14) – (8.17) and (9.1) – (9.8), we define re-scaled variables (denoted by overlines) by dividing each variable by a reference value:

$$
\begin{aligned}
&[\overline{p53m_n}] = \frac{[p53m_n]}{[p53m_0]}, [\overline{p53m_c}] = \frac{[p53m_c]}{[p53m_0]}, [\overline{p53_n}] = \frac{[p53_n]}{[p53_0]}, [\overline{p53_c}] = \frac{[p53_c]}{[p53_0]}, \\
&[\overline{Mdm2m_n}] = \frac{[Mdm2m_n]}{[Mdm2m_0]}, [\overline{Mdm2m_c}] = \frac{[Mdm2m_c]}{[Mdm2m_0]}, \\
&[\overline{Mdm2_n}] = \frac{[Mdm2_n]}{[Mdm2_0]}, [\overline{Mdm2_c}] = \frac{[Mdm2_c]}{[Mdm2_0]}, \overline{t} = \frac{t}{\tau}, \overline{x} = \frac{x}{L}, \overline{y} = \frac{y}{L}.
\end{aligned}
\tag{11.9}
$$

Substituting the scaling in equation (11.9) into the extended p53-Mdm2 model gives a non-dimensionalised model with non-dimensional parameters (which we denote with asterisks) that are related to dimensional parameters as follows:

$$
\begin{aligned}
&D_{i_j}^* = \frac{\tau D_{i_j}}{L^2}, \zeta^* = \frac{\tau\zeta}{[p53m_0]}, \phi^* = \tau\phi, \beta^* = \frac{\tau\beta[p53m_0]}{[p53_0]}, \mu^* = \tau\mu, \nu^* = \tau\nu, \\
&Mdm2^* = \frac{\widehat{Mdm2}}{[Mdm2_0]}, \alpha^* = \frac{\tau\alpha}{[Mdm2m_0]}, \eta^* = \frac{\tau\eta}{[Mdm2m_0]}, p53^* = \frac{\widehat{p53}}{[p53_0]}, \\
&\theta^* = \frac{[p53_0]\theta}{[Mdm2_0]}, \gamma^* = \frac{\tau\gamma[Mdm2m_0]}{[Mdm2_0]}, \rho^* = \tau\rho, D_m^* = \frac{\tau D_m}{L^2}, D_p^* = \frac{\tau D_p}{L^2}, \\
&d^* = \frac{d}{L}, a^* = \frac{\tau a}{L}, l^* = \frac{l}{L}.
\end{aligned}
$$

We solve the non-dimensional model using COMSOL 3.5a, finding non-dimensional parameter values that yield oscillatory dynamics. We chose the same values as in equation (60) in Sturrock et al. (2011) except for those parameters which were new because of our extension to the model. These latter values were chosen as follows: $\theta^* = 1$, $\zeta^* = 0.35$, $D_m^* = D_{i_j}^*/5$, $D_p^* = D_{i_j}^*/15$, $d^* = 0.01$, $a^* = 0.03$, $l^* = 0.63$.

Finally, we calculated the dimensional parameter values. To do this, we had to estimate

the reference values. We found a reference concentration for $[p53_0]$ of 0.5μM and estimated reference concentrations for rest of the model species as follows: $[p53_0] = 0.5\mu$M, $[Mdm2m_0] = 0.05\mu$M, $[Mdm2_0] = 2\mu$M, and $[p53m_0] = 0.025\mu$M. As with the Hes1 model, we assumed a cell to be of width 30μm, which again leads to the reference length $L = 10\mu$m. Our simulations of the non-dimensionalised model gave oscillations with a period of approximately 360 non-dimensional time units or 360τ dimensional units (using equation (11.10)) and the experimentally observed period is approximately 3 hours (Monk, 2003). Hence we set $360\tau = 3$ hours $= 10800$ seconds, so that $\tau = 30$s. The reference time $\tau = 30$ seconds was based on simulations of the extended p53-Mdm2 model since this was our most realistic p53-Mdm2 model. For all variants of this model (for example, setting active transport rates to zero), we retained the reference time $\tau = 30$ seconds for ease of comparison of the numerical results. Using our references values and non-dimensional parameter values, we found dimensional parameter values from equation (11.10).

Bibliography

Agrawal, S., Archer, C., and Schaffer, D. V. (2009). Computational models of the notch network elucidate mechanisms of context-dependent signaling. *PLoS Comput. Biol.*, 5:e1000390.

Alberts, B., Johnson, A., Lewis, J., Raff, M., Roberts, K., and Walter, P. (2008). *Molecular Biology of the Cell*. Garland Science, Taylor and Francis Group Ltd, Oxford, fifth edition.

Bancaud, A., Huet, S., Daigle, N., Mozziconacci, J., Beaudouin, J., and Ellenberg, J. (2009). Molecular crowding affects diffusion and binding of nuclear proteins in heterochromatin and reveals the fractal organization of chromatin. *EMBO J.*, 28:3785–3798.

Bar-Or, R. L., Maya, R., Segel, L. A., Alon, U., Levine, A. J., and Oren, M. (2000). Generation of oscillations by the p53-Mdm2 feedback loop: A theoretical and experimental study. *Proc. Natl. Acad. Sci. USA*, 97:11250–11255.

Barik, D., Baumann, W. T., Paul, M. R., Novak, B., and Tyson, J. J. (2010). A model of yeast cell-cycle regulation based on multisite phosphorylation. *Mol. Sys. Biol.*, 6: 405.

Barik, D., Paul, M. R., Baumann, W. T., Cao, Y., and Tyson, J. J. (2008). Stochastic

simulation of enzyme-catalyzed reactions with disparate timescales. *Biophys. J.*, 95:3563–3574.

Barrio, M., Burrage, K., Leier, A., and Tian, T. (2006). Oscillatory regulation of Hes1: Discrete stochastic delay modelling and simulation. *PLoS ONE*, 2:e117.

Baserga, R. (2007). Is cell size important? *Cell Cycle*, 6(7):814–816.

Batchelor, E., Loewer, A., and Lahav, G. (2009). The ups and downs of p53: understanding protein dynamics in single cells. *Nat. Rev. Cancer*, 9:371–377.

Batchelor, E., Mock, C. S., Bhan, I., Loewer, A., and Lahav, G. (2008). Recurrent initiation: A mechanism for triggering p53 pulses in response to DNA damage. *Mol. Cell*, 30:277–289.

Beck, M., Forster, F., Ecke, M., Plitzko, J. M., Melchoir, F., Gerisch, G., Baumeister, W., and Medalia, O. (2004). Nuclear pore complex structure and dynamics revealed by cryoelectron tomography. *Science*, 306:1387–1390.

Bennet, W. P., Hussain, S. P., Vahakangas, K. H., Khan, M. A., Shields, P. G., and Harris, C. C. (1999). Molecular epidemiology of human cancer risk: gene environment interactions and p53 mutation spectrum in human lung cancer. *J. Pathol.*, 187:8–18.

Bernard, S., Čajavec, B., Pujo-Menjouet, L., Mackey, M. C., and Herzel, H. (2006). Modelling transcriptional feedback loops: the role of Gro/TLE1 in Hes1 oscillations. *Phil. Trans. Roy. Soc. A*, 364:1155–1170.

Bolouri, H. (2008). *Computational modeling of gene regulatory networks – a primer*. Imperial College Press, London.

Brown, G. and Kholodenko, B. (1999). Spatial gradients of cellular phospho-proteins. *FEBS Letters*, 457:452–454.

Burrage, K., Burrage, P. M., Leier, A., Marquez-Lago, T., and Jr, D. V. N. (2011). *Design and Analysis of Biomolecular Circuits: Engineering Approaches to Systems and Synthetic Biology*. Springer Science + Business Media, New York.

Busenberg, S. and Driessche, P. (1990). Analysis of a disease transmission model in a population with varying size. *J. Math. Biol.*, 28:257–270.

Busenberg, S. and Driessche, P. (1993). A method for proving the non-existence of limit cycles. *J. Math. Anal. Appl.*, 172:463–479.

Busenberg, S. and Mahaffy, J. M. (1985). Interaction of spatial diffusion and delays in models of genetic control by repression. *J. Math. Biol.*, 22:313–333.

Cangiani, A. and Natalini, R. (2010). A spatial model of cellular molecular trafficking including active transport along microtubules. *J. Theor. Biol.*, 267:614–625.

Carbonaro, M., O'Brate, A., and Giannakakou, P. (2011). Microtubule disruption targets HIF-1α mRNA to cytoplasmic P-bodies for translation repression. *J. Cell. Biol.*, 192:83–99.

Carter, S. and Vousden, K. H. (2009). Modifications of p53: competing for the lysines. *Curr. Opin. Genet. Dev.*, 19:18–24.

Caspi, A., Granek, R., and Elbaum, M. (2000). Enhanced diffusion in active intracellular transport. *Phys. Rev. Lett.*, 85:5655–5658.

Chahine, M. N. and Pierce, G. N. (2009). Therapeutic targeting of nuclear protein import in pathological cell conditions. *Pharmacol. Rev.*, 61:358–372.

Ciliberto, A., Novak, B., and Tyson, J. J. (2005). Steady states and oscillations in the p53/Mdm2 network. *Cell Cycle*, 4:488–493.

Cole, C. N. and Scarcelli, J. J. (2006). Transport of messenger RNA from the nucleus to the cytoplasm. *Curr. Opin. Cell Biol.*, 18:299–306.

Cole, N. B. and Lippincott-Schwartz, J. (1995). Organization of organelles and membrane traffic by microtubules. *Curr. Opin. Cell Biol.*, 7:55–64.

Collins, M. K., Perkins, G. R., Rodriguez-Tarduchy, G., Nieto, M. A., and López-Rivas, A. (1994). Growth factors as survival factors: regulation of apoptosis. *Bioessays.*, 16:133–138.

Coutts, A. S., Adams, C. J., and Thangue, N. B. L. (2009). p53 ubiquitination by Mdm2: a never ending tail? *DNA Repair*, 8:483–490.

Davidson, M. W. (26th April 2011). Micromagnet website. *http://micro.magnet.fsu.edu/primer/techniques/fluorescence/gallery/cells/u2/u2cellslarge8.html*.

de Oca Luna, R. M., Wagner, D. S., and Lozano, G. (1995). Rescue of early embryonic lethality in mdm2-deficient mice by deletion of p53. *Nature*, 378:203–206.

Diller, L., Kassel, J., Nelson, C. E., Gryka, M. A., Litwak, G., Gebhardt, M., Bressac, B., Ozturk, M., Baker, S. J., Vogelstein, B., and Friend, S. H. (1990). p53 functions as a cell cycle control protein in osteosarcomas. *Mol. Cell. Biol.*, 10:5772–5781.

Dimitrio, L., Clairambault, J., and Natalini, R. (2013). A spatial physiological model for p53 intracellular dynamics. *J. Theor. Biol.*, 316:9–24.

Dinh, A. T., Theofanous, T., and Mitragotri, S. (2005). A model of intracellular trafficking of adenoviral vectors. *Biophys. J.*, 89:1574–1588.

Drawert, B., Engblom, S., and Hellander, A. (2012). Urdme: a modular framework for stochastic simulation of reaction-transport processes in complex geometries. *BMC Syst. Biol.*, 6:76.

Elf, J. and Ehrenberg, M. (2004). Spontaneous separation of bi-stable biochemical systems into spatial domains of opposite phases. *Syst. Biol.*, 1 (2):230–236.

Engblom, S., Ferm, L., Hellander, A., and Lötstedt, P. (2009). Simulation of stochastic reaction–diffusion processes on unstructured meshes. *SIAM J. Sci. Comput.*, 31 (3):1774–1797.

Fall, C. P., Marland, E. S., Wagner, J. M., and Tyson, J. J. (2002). *Computational Cell Biology*. Springer, New York, fifth edition.

Fange, D. and Elf, J. (2006). Noise-induced min phenotypes in E. coli. *PLoS Comput. Biol.*, 2:e80.

Feldherr, C. M. and Akin, D. (1991). Signal-mediated nuclear transport in proliferating and growth-arrested BALB/c 3T3 cells. *J. Cell. Biol.*, 115:933–939.

Ferrari, S. and Palmerini, E. (2007). Adjuvant and neoadjuvant combination chemotherapy for osteogenic sarcoma. *Curr. Opin. Oncol.*, 19:341–346.

Finlay, C. A. (1993). The mdm-2 oncogene can overcome wild-type p53 suppression of transformed cell growth. *Mol. Cell. Biol.*, 12:301–306.

Fusco, D., Accornero, N., Lavoie, B., Shenoy, S. M., Blanchard, J., Singer, R. H., and Bertrand, E. (2003). Single mRNA molecules demonstrate probabilistic movement in living mammalian cells. *Curr. Biol.*, 13:161–167.

Garvie, M. R. (2007). Finite-difference schemes for reaction-diffusion equations modeling predator-prey interactions in matlab. *Bull. Math. Biol.*, 69:931–956.

Gasiorowski, J. Z. and Dean, D. A. (2003). Mechanisms of nuclear transport and interventions. *Adv. Drug Deliv. Rev.*, 55:703–716.

Gerstein, M., Bruce, C., Rozowsky, J., Zheng, D., Du, J., Korbel, J., Emanuelsson, O., Zhang, Z., Weissman, S., and Snyder, M. (2007). What is a gene, post-ENCODE? history and updated definition. *Genome Res.*, 17:669–681.

Geva-Zatorsky, N., Dekel, E., Batchelor, E., Lahav, G., and Alon, U. (2010). Fourier analysis and systems identification of the p53 feedback loop. *Proc. Natl. Acad. Sci. USA*, 107:13550–13555.

Geva-Zatorsky, N., Rosenfeld, N., Itzkovitz, S., Milo, R., Sigal, A., Dekel, E., Yarnitzky, T., Liron, Y., Polak, P., Lahav, G., and Alon, U. (2006). Oscillations and variability in the p53 system. *Mol. Syst. Biol.*, 2:E1–E13.

Giannakakou, P., Sackett, D. L., Ward, Y., Webster, K. R., Blagosklonny, M. V., and Fojo, T. (2000). p53 is associated with cellular microtubules and is transported to the nucleus by dynein. *Nat. Cell Biol.*, 2:709–717.

Gibson, M. A. and Bruck, J. (2000). Efficient exact stochastic simulation of chemical systems with many species and many channels. *J. Phys. Chem.*, 104:1876–1889.

Gillespie, D. T. (1976). A general method for simulating the stochastic time evolution of coupled chemical reactions. *J. Comput. Phys.*, 22:403–434.

Glass, L. and Kauffman, S. A. (1970). Co-operative components, spatial localization and oscillatory cellular dynamics. *J. Theor. Biol.*, 34:219–237.

Gordon, K. E., Leeuwen, I. M. M. V., Laín, S., and Chaplain, M. A. J. (2009). Spatio-temporal modelling of the p53-mdm2 oscillatory system. *Math. Model. Nat. Phenom.*, 4:97–116.

Hamstra, D. A., Bhojani, M. S., Griffin, L. B., Laxman, B., Ross, B. D., and Rehemtulla, A. (2006). Real-time evaluation of p53 oscillatory behaviour *in vivo* using bioluminescent imaging. *Cancer Res.*, 66:7482–7489.

Hanisch, A., Holder, M. V., Choorapoikayil, S., Gajewski, M., and Özbudak, E. M. (2013). The elongation rate of RNA polymerase II in zebrafish and its significance in the somite segmentation clock. *Development*, 140:444–453.

Harang, R., Bonnet, G., and Petzold, L. R. (2012). Wavos: a matlab toolkit for wavelet analysis and visualization of oscillatory systems. *BMC Res. Notes*, 26:5:163.

Hasty, J., Pradines, J., Dolnik, M., and Collins, J. J. (2000). Noise-based switches and amplifiers for gene expression. *Proc. Natl. Acad. Sci. USA*, 97:2075–2080.

Hellander, A. and Lötstedt, P. (2010). Incoporating active transport of cellular cargo in stochastic mesoscopic models of living cells. *Multiscale Model. Sim.*, 8:1691–1714.

Hirata, H., Yoshiura, S., Ohtsuka, T., Bessho, Y., Harada, T., K.Yoshikawa, and Kageyama, R. (2002). Oscillatory expression of the bHLH factor Hes1 regulated by a negative feedback loop. *Science*, 298:840–843.

Howard, M. and Rutenberg, A. D. (2003). Pattern formation inside bacteria: Fluctuations due to the low copy number of proteins. *Phys. Rev. Lett.*, 90:128102.

Jensen, M. H., Sneppen, J., and Tiana, G. (2003). Sustained oscillations and time delays in gene expression of protein hes1. *FEBS Lett.*, 541:176–177.

Johansson, T., Lejonklou, M. H., Ekeblad, S., Stålberg, P., and Skogseid, B. (2008). Lack of nuclear expression of hairy and enhancer of split-1 (HES1) in pancreatic endocrine tumors. *Horm. Metab. Res.*, 40:354–359.

Jones, S. N., Roe, A. E., Donehower, L. A., and Bradley, A. (1995). Rescue of embryonic lethality in Mdm2-deficient mice by absence of p53. *Nature*, 378:206–208.

Jong, H. D. (2002). Modeling and simulation of genetic regulatory systems: a literature review. *J. Comp. Biol.*, 9:67–103.

Jordan, M. A. and Wilson, L. (2004). Microtubules as a target for anticancer drugs. *Nature Rev. Cancer*, 4:253–265.

Kar, S., Baumann, W. T., Paul, M. R., and Tyson, J. J. (2009). Exploring the roles of noise in the eukaryotic cell cycle. *Proc. Natl. Acad. Sci. USA*, 106:6471–6476.

Kavallaris, M. (2010). Microtubules and resistance to tubulin-binding agents. *Nature Rev. Cancer*, 10:194–204.

Keller, E. F. and Harel, D. (2007). Beyond the gene. *PLoS ONE*, 11:e1231.

Kherlopian, A., Song, T., Duan, Q., Neimark, M., Po, M., Gohagan, J., and Laine, A. (2008). A review of imaging techniques for systems biology. *BMC Sys. Biol.*, 2:74–92.

Kholodenko, B. (2006). Cell-signalling dynamics in time and space. *Nature Rev. Mol. Cell Biol.*, 7:165–174.

Kim, I. S., Kim, D. H., Han, S. M., Chin, M. U., Nam, H. J., Cho, H. P., Choi, S. Y., Song, B. J., Kim, E. R., Bae, Y. S., and Moon, Y. H. (2000). Truncated form of importin alpha identified in breast cancer cells inhibits nuclear import of p53. *J. Biol. Chem*, 275:23139–23145.

Klonis, N., Rug, M., Harper, I., Wickham, M., Cowman, A., and Tilley, L. (2002). Fluorescence photobleaching analysis for the study of cellular dynamics. *Eur. Biophys. J.*, 31:36–51.

Kobayashi, T. and Kageyama, R. (2010). Hes1 regulates embryonic stem cell differentiation by suppressing notch signaling. *Genes to Cells*, 15:689–698.

Kobayashi, T. and Kageyama, R. (2011). Hes1 oscillations contribute to heterogeneous differentiation responses in embryonic stem cells. *Genes*, 2:219–228.

Kobayashi, T., Mizuno, H., Imayoshi, I., Furusawa, C., Shirahige, K., and Kageyama, R. (2009). The cyclic gene hes1 contributes to diverse differentiation responses of embryonic stem cells. *Genes & Development*, 23:1870–1875.

Lahav, G., Rosenfeld, N., Sigal, A., Geva-Zatorsky, N., Levine, A. J., Elowitz, M. B.,

and Alon, U. (2004). Dynamics of the p53-Mdm2 feedback loop in individual cells. *Nature Genet.*, 36:147–150.

Lane, D. P. (1992). p53, guardian of the genome. *Nature*, 358:15–16.

Levine, A. J. (1997). p53, the cellular gatekeeper for growth and division. *Cell*, 88:323–331.

Lewis, J. (2003). Autoinhibition with transcriptional delay: a simple mechanism for the zebrafish somitogenesis oscillator. *Curr. Biol.*, 13:1398–1408.

Liang, J. and Han, J. (2012). Stochastic boolean networks: An efficient approach to modeling gene regulatory networks. *BMC Syst. Biol.*, 6:113.

Lightcap, E. S., McCormack, T. A., Pien, C. S., Chau, V., Adams, J., and Elliott, P. J. (2000). Proteasome inhibition measurements: clinical application. *Clin. Chem.*, 46:673–683.

Locke, J. C. W., Southern, M. M., Kozma-Bognár, L., Hibberd, V., Brown, P. E., Turner, M. S., and Millar, A. J. (2005). Extension of a genetic network model by iterative experimentation and mathematical analysis. *Mol. Syst. Biol.*, 1:1–9.

Loewer, A., Batchelor, E., Gaglia, G., and Lahav, G. (2010). Basal dynamics of p53 reveal transcriptionally attenuated pulses in cycling cells. *Cell*, 142:89–100.

Lomakin, A. and Nadezhdina, E. (2010). Dynamics of nonmembranous cell components: Role of active transport along microtubules. *Biochemistry (Moscow)*, 75:7–18.

Ma, L., Wagner, J., Rice, J. J., Hu, W., Levine, A. J., and Stolovitzky, G. A. (2005). A plausible model for the digital response of p53 to DNA damage. *Proc. Natl. Acad. Sci. USA*, 102:14266–14271.

Mahaffy, J. M. (1988). Genetic control models with diffusion and delays. *Math. Biosci.*, 90:519–533.

Mahaffy, J. M. and Pao, C. V. (1984). Models of genetic control by repression with time delays and spatial effects. *J. Math. Biol.*, 20:39–57.

Maki, C. G., Huibregtse, J. M., and Howley, P. M. (1996). In vivo ubiquitination and proteasome-mediated degradation of p53. *Cancer Res.*, 56:2649–2654.

Mallat, S. A. (1999). *A wavelet tour of signal processing*. Academic Press.

Marfori, M., Mynott, A., Ellis, J. J., Mehdi, A. M., Saunders, N. F. W., Curmi, P. M., Forwood, J. K., Bodén, M., and Kobe, B. (2010). Molecular basis for specificity of nuclear import and prediction of nuclear localization. *Biochim. Biophys. Acta Mol. Cell Res.*, 1813:1562–1577.

Marine, J. C. and Jochemsen, A. G. (2003). Mdmx and Mdm2: brothers in arms? *Cell Cycle*, 3:900–904.

Marquez-Lago, T. T., Leier, A., and Burrage, K. (2012). Anomalous diffusion and multifractional brownian motion: simulating molecular crowding and physical obstacles in systems biology. *IET Sys. Biol.*, 6:134–142.

Masamizu, Y., Ohtsuka, T., Takashima, Y., Nagahara, H., Takenaka, Y., Yoshikawa, K., Okamura, H., and Kageyama, R. (2006). Real-time imaging of the somite segmentation clock: revelation of unstable oscillators in the individual presomitic mesoderm cells. *Proc. Natl. Acad. Sci. USA*, 103:1313–1318.

Matsuda, T., Miyawaki, A., and Nagai, T. (2008). Direct measurement of protein dynamics inside cells using a rationally designed photoconvertible protein. *Nature Meth.*, 5:339–345.

Mayo, L. D. and Donner, D. B. (2001). A phosphatidylinositol 3-kinase/akt pathway promotes translocation of mdm2 from the cytoplasm to the nucleus. *Proc. Natl. Acad. Sci. USA*, 98:11598–11603.

Mendez, V., Fedotov, S., and Horsthemke, W. (2010). *Reaction-Transport Systems*. Springer, New York.

Meyers, J., Craig, J., and Odde, D. J. (2006). Potential for control of signaling pathways via cell size and shape. *Curr. Biol.*, 16:1685–1693.

Michalet, X., Pinaudand, F. F., Bentolila, L. A., Tsay, J. M., Doose, S., Li, J. J., Sundaresan, G., Wu, A. M., Gambhir, S. S., and Weiss, S. (2005). Quantum dots for live cells, in vivo imaging, and diagnostics. *Science*, 307:538–544.

Mihalas, G. I., Neamtu, M., Opris, D., and Horhat, R. F. (2006). A dynamic p53-Mdm2 model with time delay. *Chaos Sol. Fract.*, 30:936–945.

Momiji, H. and Monk, N. A. M. (2008). Dissecting the dynamics of the Hes1 genetic oscillator. *J. Theor. Biol.*, 254:784–798.

Monk, N. A. M. (2003). Oscillatory expression of Hes1, p53, and NF-κB driven by transcriptional time delays. *Curr. Biol.*, 13:1409–1413.

Muller, M. J. I., Klumpp, S., and Lipowsky, R. (2008). Tug-of-war as a cooperative mechanism for bidirectional cargo transport of molecular motors. *Proc. Natl. Acad. Sci. USA*, 105:4609–4614.

Nelson, D. E., Ihekwaba, A. E. C., Elliott, M., Johnson, J. R., Gibney, C. A., Foreman, B. E., Nelson, G., See, V., Horton, C. A., Spiller, D. G., Edwards, S. W., McDowell, H. P., Unitt, J. F., Sullivan, E., Grimley, R., Benson, N., Broomhead, D., Kell, D. B., and White, M. R. H. (2004). Oscillations in NF-κB signaling control the dynamics of gene expression. *Science*, 306:704–708.

Neves, S. R., Tsokas, P., Sarkar, A., Grace, E. A., Rangamani, P., Taubenfeld, S. M., Alberini, C. M., Schaff, J. C., Blitzer, R. D., Moraru, I. I., and Iyengar, R. (2008). Cell shape and negative links in regulatory motifs together control spatial information flow in signaling networks. *Cell*, 133:666–680.

Norvell, A., Debec, A., Finch, D., Gibson, L., and Thoma, B. (2005). Squid is required for efficient posterior localization of oskar mRNA during drosophila oogenesis. *Dev. Genes Evol.*, 215:340–349.

O'Brate, A. and Giannakakou, P. (2003). The importance of p53 location: nuclear or cytoplasmic zip code? *Drug Res. Updates*, 6(6):313–322.

Orlowski, R. Z. and Kuhn, D. J. (2008). Proteasome inhibitors in cancer therapy: Lessons from the first decade. *Clin. Cancer Res.*, 14:1649–1657.

Ouattara, D. A., Abou-Jaoudé, W., and Kaufman, M. (2010). From structure to dynamics: Frequency tuning in the p53-Mdm2 network. ii Differential and stochastic approaches. *J. Theor. Biol.*, 264:1177–1189.

Perkins, N. D. (2007). Integrating cell-signalling pathways with NF-κB and IKK function. *Nature Rev. Mol. Cell Biol.*, 8:49–62.

Pincus, Z. and Theriot, J. A. (2007). Comparison of quantitative methods for cell-shape analysis. *J. Microscopy*, 227:140–156.

Pommier, Y., Sordet, O., Antony, S., Hayward, R. L., and Kohn, K. W. (2004). Apoptosis defects and chemotherapy resistance: molecular interaction maps and networks. *Oncogene*, 23:2934–2949.

Prinz, H. (2010). Hill coefficients, dose-response curves, and allosteric mechanisms. *J. Chem. Biol.*, 3:37–44.

Proctor, C. J. and Gray, D. A. (2008). Explaining oscillations and variability in the p53-Mdm2 system. *BMC Syst. Biol.*, 2:1–20.

Puszyński, K., Bertolusso, R., and Lipniacki, T. (2009). Crosstalk between p53 and NF-κB systems: pro- and anti-apoptotic functions of NF-κB. *IET Sys. Biol.*, 3:356–367.

Puszyński, K., Hat, B., and Lipniacki, T. (2008). Oscillations and bistability in the stochastic model of p53 regulation. *J. Theor. Biol.*, 254:452–465.

Rangamani, P. and Iyengar, R. (2007). Modelling spatio-temporal interactions within the cell. *J. Biosci.*, 32:157–167.

Robati, M., Holtz, D., and Dunton, C. J. (2008). A review of topotecan in combination chemotherapy for advanced cervical cancer. *Ther. Clin. Risk. Manag.*, 4:213–218.

Rodriguez, M., Dargemont, C., and Stutz, F. (2004). Nuclear export of RNA. *Biol. Cell*, 96:639–655.

Roth, D. M., Moseley, G. W., Glover, D., Pouton, C. W., and Jans, D. A. (2007). A microtubule-facilitated nuclear import pathway for cancer regulatory proteins. *Traffic*, 8:673–686.

Ryan, K. M., Phillips, A. C., and Vousden, K. H. (2001). Regulation and function of the p53 tumor suppressor protein. *Curr. Opin. Cell Biol.*, 13:332–337.

Sang, L., Coller, H. A., and Roberts, J. M. (2008). Control of the reversibility of cellular quiescence by the transcriptional repressor HES1. *Science*, 321:1095–1100.

Sang, L., Roberts, J. M., and Coller, H. A. (2010). Hijacking HES1: Tumors co-opt the anti-differentiation stategies of queiscent cells. *Trends Mol. Med.*, 16:17–26.

Schnee, M. J., Arn, E. A., Bullock, S. L., and Macdonald, P. M. (2005). Recognition of the bcd mRNA localization signal in drosophila embryos and ovaries. *Mol. Cell. Biol.*, 24:1501–1510.

Seksek, O., Biwersi, J., and Verkman, A. S. (1997). Translational diffusion of macromolecule-sized solutes in cytoplasm and nucleus. *J. Cell. Biol.*, 138:131–142.

Shahrezaei, V. and Swain, P. S. (2008). The stochastic nature of biochemical networks. *Curr. Opin. Biotechnol.*, 19:369–374.

Shankaran, H., Ippolito, D. L., Chrisler, W. B., Resat, H., Bollinger, N., Opresko, L. K., and Wiley, H. S. (2009). Rapid and sustained nuclear-cytoplasmic ERK oscillations induced by epidermal growth factor. *Mol. Syst. Biol.*, 5: 332.

Shimojo, H., Ohtsuka, T., and Kageyama, R. (2008). Oscillations in notch signaling regulate maintenance of neural progenitors. *Neuron*, 58:52–64.

Shymko, R. M. and Glass, L. (1974). Spatial switching in chemical reactions with heterogeneous catalysis. *J. Chem. Phys.*, 60:835–841.

Slaymaker, M., Osborne, J., Simpson, A., and Gavaghan, D. (2012). On an infrastructure to support sharing and aggregating pre- and post-publication systems biology research data. *Syst. Synth. Biol.*, 6:35–49.

Smith, D. A. and Simmons, R. M. (2001). Model of motor-assisted transport of intracelullar particules. *Biophys. J.*, 80:45–68.

Stommel, J. M. and Wahl, G. M. (2004). Accelerated MDM2 auto-degradation induced by DNA-damage kinases is required for p53 activation. *Embo. J.*, 23:1574–1556.

Sturrock, M., Hellander, A., Matzavinos, A., and Chaplain, M. A. J. (2013). Spatial stochastic modelling of the hes1 gene regulatory network: intrinsic noise can

explain heterogeneity in embryonic stem cell differentiation. *J. R. Soc. Interface*, 10:20120988.

Sturrock, M., Terry, A. J., Xirodimas, D. P., Thompson, A. M., and Chaplain, M. A. J. (2011). Spatio-temporal modelling of the Hes1 and p53-Mdm2 intracellular signalling pathways. *J. Theor. Biol.*, 273:15–31.

Sturrock, M., Terry, A. J., Xirodimas, D. P., Thompson, A. M., and Chaplain, M. A. J. (2012). Influence of the nuclear membrane, active transport and cell shape on the Hes1 and p53–Mdm2 pathways: Insights from spatio-temporal modelling. *Bull. Math. Biol.*, 74:1531–1579.

Tafvizi, A., Mirny, L. A., and Oijen, A. M. V. (2011). Dancing on DNA: kinetic aspects of search processes on DNA. *Chem. Phys. Chem.*, 12:1481–1489.

Takahashi, K., Tănase-Nicola, S., and ten Wolde, P. R. (2010). Spatio-temporal correlations can drastically change the response of a MAPK pathway. *Proc. Natl. Acad. Sci. USA*, 107:2473–2478.

Takebayashi, K., Sasai, Y., Sakai, Y., Watanabe, T., Nakanishi, S., and Kageyama, R. (1994). Structure, chromosomal locus, and promoter analysis of the gene encoding the mouse helix-loop-helix factor HES-1. *J. Biol. Chem.*, 269:5150–5156.

Tekotte, H. and Davis, I. (2002). Intracellular mRNA localization: motors move messages. *TIG*, 18:636–642.

Terry, A. J. and Chaplain, M. A. J. (2011). Spatio-temporal modelling of the NF-κB intracellular signalling pathway: The roles of diffusion, active transport, and cell geometry. *J. Theor. Biol.*, 290:7–26.

Terry, A. J., Sturrock, M., Dale, J. K., Maroto, M., and Chaplain, M. A. J. (2011). A spatio-temporal model of Notch signalling in the zebrafish segmentation clock: Conditions for synchronised oscillatory dynamics. *PLoS ONE*, 6:e16980.

Thut, C. J., Goodrich, J. A., and Tjian, R. (1997). Repression of p53-mediated transcription by MDM2: a dual mechanism. *Genes Dev.*, 11:1974–1986.

Tiana, G., Jensen, M. H., and Sneppen, K. (2002). Time delay as a key to apoptosis induction in the p53 network. *Eur. Phys. J. B*, 29:135–140.

Toledo, F. and Wahl, G. M. (2006). Regulating the p53 pathway: *in vitro* hypotheses, *in vivo* veritas. *Nature Rev. Cancer*, 6:909–923.

Torrence, C. and Compo, G. P. (1998). A practical guide to wavelet analysis. *Bull. Am. Meteorol. Soc.*, 79:61–78.

van Zon, J. S., Morelli, M. J., Tănase-Nicola, S., and ten Wolde, P. R. (2006). Diffusion of transcription factors can drastically enhance the noise in gene expression. *Biophys. J.*, 91:4350–4367.

Vogelstein, B., Lane, D., and Levine, A. J. (2000). Surfing the p53 network. *Nature*, 408:307–310.

Vousden, K. H. and Prives, C. (2009). Blinded by the light: the growing complexity of p53. *Cell*, 137:413–431.

Wachsmuth, M., Waldeck, W., and Langowski, J. (2000). Anomalous diffusion of fluorescent probes inside living cell nuclei investigated by spatially-resolved fluorescence correlation spectroscopy. *J. Mol. Biol.*, 298:677–689.

Wang, S. and Hazelrigg, T. (1994). Implications for bcd mRNA localization from spatial distribution of exu protein in drosophila oogenesis. *Nature*, 369:400–403.

Weis, K. (2003). Regulating access to the genome: nucleocytoplasmic transport throughout the cell cycle. *Cell*, 112:441–451.

Weiss, J. N. (2009). The hill equation revisited: uses and misuses. *FASEB J.*, 11:835–841.

Weiss, M., Hashimoto, H., and Nilsson, T. (2004). Anomalous protein diffusion is a measure for cytoplasmic crowding in living cells. *Biophys. J.*, 87:3518–3524.

Wilkinson, D. (2009). Stochastic modelling for quantitative description of heterogeneous biological systems. *Nat. Rev. Genet.*, 10:122–133.

Xirodimas, D. P., Stephen, C. W., and Lane, D. P. (2001). Cocompartmentalization of p53 and Mdm2 is a major determinant for Mdm2-mediated degradation of p53. *Exp. Cell. Res.*, 270:66–77.

Yadav, A., Milu, S. M., and Horsthemke, W. (2008). Turing instability in reaction-subdiffusion systems. *Phys. Rev. E*, 78:026116.

Yu, X., Alder, J. K., Chun, J. H., Friedman, A. D., Heimfeld, S., Cheng, L., and Civin, C. I. (2006). HES1 inhibits cycling of hematopoietic progenitor cells via DNA binding. *Stem Cells*, 24:876–888.

Zeiser, S., Muller, J., and Liebscher, V. (2007). Modeling the Hes1 oscillator. *J. Comp. Biol.*, 14:984–1000.

Zhang, P., Yang, Y., Zweidler-McKay, P. A., and Hughes, D. P. M. (2008). Critical role of notch signaling in osteosarcoma invasion and metastasis. *Clin. Cancer Res.*, 14:2962–2969.

Zhang, T., Brazhnik, P., and Tyson, J. J. (2007). Exploring mechanisms of the DNA-damage response: p53 pulses and their possible relevance to apoptosis. *Cell Cycle*, 6:85–94.

Zhou, Q., Jouneau, A., Brochard, V., Adenot, P., and Renard, J. P. (2001). Developmental potential of mouse embryos reconstructed from metaphase embryonic stem cell nuclei. *Biol. Reprod.*, 65:412–419.

Zilfou, J. T. and Lowe, S. W. (2009). Tumor suppressive functions of p53. *Cold Spring Harbor Perspect. Biol.*, 1:a001883.